Worcester Polytechnic Institute
Digital WPI

Major Qualifying Projects (All Years) Major Qualifying Projects

April 2014

Study of whirling instability

Weifan Liu
Worcester Polytechnic Institute

Repository Citation

Liu, W. (2014). *Study of whirling instability*. Retrieved from https://digitalcommons.wpi.edu/mqp-all/4101

Project Number: MQP-SDO-203

Study of whirling instability

A Major Qualifying Project Report
Submitted to The Faculty
of
Worcester Polytechnic Institute
In partial fulfillment of the requirements for the
Degree of Bachelor of Science
by

Weifan Liu

April, 2014

Approved:

Professor Sarah Olson

Abstract

We study the behavior of a Kirchhoff rod with intrinsic bend and twist immersed in a viscous, incompressible fluid at zero Reynolds number. Using a regularized Stokes formulation, we investigate the effect of different material moduli and prescribed configurations on the helical equilibria of a free and tethered rod. A model developed by Sookkyung Lim was first analyzed and then extended to study the instability of a tethered rod with a straight and helical configuration in various conditions. Then we explore the behavior of the rod in a loaded and unloaded condition prescribed with a time and spatially dependent curvature and twist along the rod. To study the instability of the rod in each case, we analyze its energy profile, configuration change and movement along each axis. Numerical simulations are presented to show some interesting results and insights gained into the instability of a Kirchhoff rod in Stokes flow. Results are discussed in connection with motion of filamentous structures such as flagella and cilia in biological contexts.

Executive Summary

Filamentous structures that twist and bend are seen in various biological structures such as proteins, flagella and cilia. Many micro-organisms swim via flagella. A eukaryotic flagellum is a cylindrical shaped appendage that protrudes from the cell body of a microorganism and is driven by a rotary engine. The rotation of these motors determines the form of micro-organism motion such as bundling, twirling and tumbling. For example, *E.coli* is a rod-shaped bacterium whose strains possess flagella to propel the bacterium when rotated by the motor through the hook. Immersed in high viscosity fluids, elastic filaments and flagella exhibit instabilities when undergoing deformation and movement. Previous modeling studies have represented the filament as a Kirchhoff rod, coupling its movement to the fluid using an immersed boundary approach. A rotating straight rod, immersed in a viscous fluid, was shown to exhibit buckling or large bending when the rotation was above a given frequency. Additionally, a rod initialized as straight and given increasing value of twist caused the rod to become unstable and buckle above a critical twist.

The goal of this project is to further explore various instabilities of a Kirchhoff rod in high viscosity flow under different conditions. To solve the coupled fluid-structure interaction, we use a regularized Stokes formulation by introducing a regularized force and torque from the unconstrained Kirchhoff rod model. First, we explore the instability of helical equilibria of a tethered rod initialized as straight with nonzero curvature and twist in Stokes flow. This corresponds to a rod that has a preferred shape corresponding to a helix. To quantify the degree of instability and analyze the effect of different material moduli on the instability, we analyze the energy profile of the rod in each case. We found that bending and twist energy of the rod is monotonically decreasing as the rod achieves its prescribed helical configuration. As the preferred twist is increased (corresponding to more turns along the helix), the rod is unable to achieve its prescribed configuration, exhibiting buckling and loops. In such cases, the rod has a higher energy, corresponding to a higher instability in the system. A tethered rod initialized as a helix also exhibits similar instabilities as the preferred twist is increased. Compared to the case where the rod is initialized as a straight rod, the rod initialized as a helix has a lower bending energy initially. As the rod bends further to achieve its prescribed configuration, the bending energy plays a more dominant role relative to the rod initialized as straight.

We also extend our study to the instability of a Kichhoff rod propagating a helical bending wave. We explore the instability of both free and tethered Kirchhoff rods. We investigate the effect of the surrounding fluid viscosity and the form of helical wave including amplitude, frequency and direction of propagation on instability of the rod. In the case of a free rod, we calculate the swimming speed of the rod associated with each helical bending wave and analyze the energy profile of the rod along with its oscillation about different axes. We found that when the rod is unable to achieve its prescribed waveform, excessively high beat frequency only results in excessive energy consumption, decreased achieved amplitude and slower swimming speed. Increasing fluid viscosity reduces the ability of the rod to achieve its prescribed amplitude and swim faster. Through our simulations, we found that in a fluid of given viscosity, the rod may increase its swimming speed and decrease its energy by choosing to propagate a wave of appropriate form (helical parameters) and frequency. We also observed an asymmetric behavior of the rod with respect to the direction in which the wave propagates. This asymmetry leads to different instabilities of a tethered rod propagating a helical bending wave. At the end of the project, we discuss the biological implications of our study in the context of aquatic micro-organisms.

Acknowledgements

I would like to thank my advisor Professor Sarah Olson for her continued support, guidance and encouragement throughout this project. Her passion and vision are invaluable assets to my future career in mathematics.

Contents

List of Figures

List of Tables

Chapter 1

Introduction and Motivation

1.1 Micro-organisms in Marine Environment

Micro-organisms are among the most important life forms on Earth, due to their diversity, ubiquity and critical role in nutrient recycling of ecosystems. The ocean is known to provide one of the largest reservoirs of micro-organisms. Fluid mechanics govern a wide range of functions for aquatic micro-organisms such as bacteria, sperm and alga, regulating their biological behavior ranging from motility to nutrient uptake to reproduction [11]. Understanding the interaction of acquatic micro-organisms with their ambient fluid environment plays a key role in understanding the biological functions of these microorganisms and their importance to marine ecology.

Micro-organisms move for different purposes. Some swim to forage for food or escape from predators; others move for external fertilization or other biological functions, often guided by the gradient of temperature, salinity or light. Moving micro-organisms can be classified as motile and non-motile. Sea urchin spermatozoon, for example, is a motile sperm cell capable of propelling themselves spontaneously and actively via flagella. Some algae and marine eggs are non-motile organisms which can only move passively as a result of ocean waves. In both cases, fluid environment is critical to the locomotion strategies of these microorganisms [13].

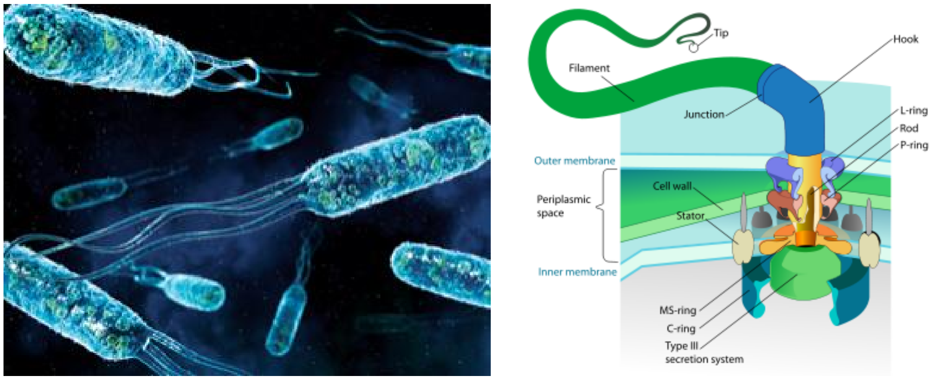

(a) (b)

Figure 1.1: (a) *E.coli* with cell body and several flagella move via flagella (taken from [16]) (b) The base of the flagellum drives the rotation of the hook and filament (taken from [17]).

Many micro-organisms swim via flagella. A eukaryotic flagellum is a cylindrical shaped appendage that protrudes from the cell body of a microorganism and is driven by a rotary engine [15]. The rotation of these motors determines the form of micro-organism motion such as bundling, twirling and tumbling. For example, *E.coli* is a rod-shaped bacterium whose strains possess flagella to propel the bacterium when rotated by the motor through the hook. Figure 1.1 (a) shows a group of motile *E.coli* with flagella. Figure 1.1 (b) shows how the bacterial flagellum is driven by a rotary engine located between cell body and flagellum. Twirling and whirling instabilities of micro-organism are critical to their movement and relocation strategy [10, 21].

1.2 Navier Stokes Equation and Low Reynolds Number

The Navier-Stokes equations describe the velocity field of fluid substances. These equations arise from applying Newtons second law to fluid motion in combination with a fluid stress due to viscosity and pressure. We consider an infinitesimal fluid element. Applying Newton's second law to this material element gives Eq. (1.1) where $\boldsymbol{F}$ is a sum of forces (kg m s^{-2}) acting on the fluid element, including body forces and surface forces. m is the mass (kg) and $\boldsymbol{u}$ is the velocity (m s^{-1}) of the element. $\frac{D\boldsymbol{u}}{Dt}$ is the material derivative of velocity, representing acceleration.

$$m\frac{D\boldsymbol{u}}{Dt} = \boldsymbol{F} \tag{1.1}$$

The forces acting on the surface of the element are described by a stress tensor $\boldsymbol{\tau}$ (kg m^{-1} s^{-2}). The stress tensor $\boldsymbol{\tau}$ consists of pressure p and deviatoric stress tensors $\boldsymbol{T}$, i.e. $\boldsymbol{\tau} = -p\boldsymbol{I} + \boldsymbol{T}$ where $\boldsymbol{I}$ is the Identity tensor. Rewriting the equation by breaking up the force component, we obtain the Cauchy momentum equation. Note that $m = \rho d\boldsymbol{x}$ where ρ (kg m^{-3}) is the density of the element. If we let $\boldsymbol{f}$ represent the body force per unit volume, i.e. $\boldsymbol{f}d\boldsymbol{x} = \boldsymbol{F}$, Eq. (1.1) can be rewritten as Eq. (1.2) given below [1].

$$\rho\frac{D\boldsymbol{u}}{Dt} = -\nabla p + \nabla\boldsymbol{T} + \boldsymbol{f} \tag{1.2}$$

Applying Newton's law of viscosity which relates the stress tensor to the first dynamic viscosity μ (kg m^{-1} s^{-1}) and second coefficient of viscosity λ (kg m^{-1} s^{-1}) which becomes essential when the fluid is compressible, we obtain Eq. (1.3) where $\boldsymbol{d}$ is the rate of strain (s^{-1}) [1].

$$\tau = 2\mu\boldsymbol{d} + \left(\lambda - \frac{2}{3}\mu\right)(\nabla u)\boldsymbol{I} \tag{1.3}$$

If we impose an incompressibility condition to the fluid, i.e. $\nabla \cdot \boldsymbol{u} = 0$, we have $\tau = 2\mu\boldsymbol{d} = \mu\left[\nabla\boldsymbol{u} + (\nabla\boldsymbol{u})^T\right]$. Hence, $\nabla\tau = \mu\Delta\boldsymbol{u}$. Substituting this expression into the Navier Stokes Equation, we obtain Eq. (1.4).

$$\rho\frac{D\boldsymbol{u}}{Dt} = -\nabla p + \mu\Delta\boldsymbol{u} + \boldsymbol{f} \tag{1.4}$$

To simplify the Navier Stokes equation in physical applications and gain a better understanding of the relative size of various parameters, we non-dimensionalize the Navier Stokes Equation Eq. (1.4). If we let L and U be the characteristic length and velocity scale respectively and choose $p = \dfrac{\mu U}{L}p*$ to be the characteristic scale for p, then the time t has scale $t = \dfrac{L}{U}t^*$ and the force density $\boldsymbol{f}$ has scale $\boldsymbol{f} = \dfrac{\mu U}{L^2}\boldsymbol{f}^*$. The non-dimensionalized equation using the above scale is given by Eq. (1.5) where $Re = \dfrac{\rho U L}{\mu}$ is called the Reynolds number.

$$Re\left(\frac{\partial \boldsymbol{u}^*}{\partial t} + \boldsymbol{u}^* \cdot \nabla \boldsymbol{u}^*\right) = -\nabla p^* + \Delta \boldsymbol{u}^* + \boldsymbol{f}^* \tag{1.5}$$

The Reynolds number is a dimensionless quantity that measures the ratio of inertial forces to viscous forces. When the Reynolds number is small, the viscous forces dominate, in which case, fluid velocities are typically slow and acceleration can be neglected. Most micro-organisms live in a world dominated by viscous forces, i.e. very low Reynolds number. We refer to this special dynamical regime where Re$\ll$0 as Stokes flow. In this regime, if an organism stops actively moving its flagellum, it stops moving instantaneously. In contrast, at high Reynolds number when a swimming person stops moving, the person will continue to glide due to non-vanishing acceleration.

Chapter 2

Methods

2.1 Stokes Flow

Stokes flow is a type of fluid flow where the relative length scale of the flow is small or the fluid is extremely viscous. In Stokes flow, $Re \to 0$ and as a result of this vanishing Reynolds number, the inertial terms can be neglected. In such a case, if we envision a micro-organism swimming in a fluid, it would immediately stop moving or wiggling once it stops generating forces. Neglecting the inertial terms, i.e. the acceleration by setting $\dfrac{D\boldsymbol{u}}{Dt} = 0$ in Eq. (1.2), we obtain the Stokes equation for an incompressible fluid. Eq. (2.1) is the Stokes equation and Eq. (2.2) is the incompressibility condition, also known as mass conservation.

$$0 = -\nabla p + \mu \Delta \boldsymbol{u} + \boldsymbol{f} \tag{2.1}$$

$$0 = \nabla \cdot \boldsymbol{u} \tag{2.2}$$

Stokes flow is independent of time. Given any boundary conditions and external force at a given time, the flow can be solved at that time instant without any knowledge of the flow at any other time. However, if the force changes, fluid flow and pressure will change instaneously. A fundamental solution of these equations is called a Stokeslet, which represents the velocity due to an external force acting at a single point in Stokes flow. Assuming an infinite domain, the Green's function is given by Eq. (2.3) where $\|\cdot\|$ denotes Euclidean norm.

$$G(\boldsymbol{x}) = -\frac{1}{4\pi\|\boldsymbol{x} - \boldsymbol{x_0}\|} \tag{2.3}$$

The Green's function is introduced to study the Dirichlet problem. The Green's function $G(\boldsymbol{x})$ for the domain D at the point $\boldsymbol{x}_0 \in D$ is a function defined for $\boldsymbol{x} \in D$ such that it satisfies the following three conditions [23].

1. $G(\boldsymbol{x})$ possesses continuous second derivaties and $\Delta G = 0$ in D, except at the point $\boldsymbol{x} = \boldsymbol{x}_0$.
2. $G(\boldsymbol{x}) = 0$ for x $\in \partial D$.
3. The function $G(\boldsymbol{x}) + \dfrac{1}{4\pi\|\boldsymbol{x} - \boldsymbol{x}_0\|}$ is finite at $\boldsymbol{x}_0$ and has continuous second derivatives everywhere and is harmonic at $\boldsymbol{x}_0$.

The singularity of the solution in Eq. (2.3) introduces difficulty in solving for the point force at $\boldsymbol{x}_0$. To ease the challenge of numerical computation and be able to solve for the velocity at each point in a fluid domain, we employ regularized Stokeslets [5]. To desingularize the solution at $\boldsymbol{x_0}$, we smooth the force function by considering the forces to be spread over a small sphere centered at $\boldsymbol{x_0}$ where the force achieves a maximum value at the center and decays to zero on the surface of the sphere. The radius of the sphere is a small numerical parameter that can be controlled independently.

To desingularize the force function, we introduce a radially symmetric smooth function ϕ_ε satisfying $\displaystyle\int_{-\infty}^{\infty} \phi_\varepsilon(\boldsymbol{x}-\boldsymbol{x_0})d\boldsymbol{x} = 1$ in $\mathbb{R}^3$ [5]. If we consider a smooth function $f(x)$ in 1-D and the convolution function given by Eq. (2.4), we know that when the regularization parameter ε is small, the blob approaches $h(x)$ near $y = x$ [4].

$$(h * \phi_\varepsilon) = \int_{-\infty}^{\infty} h(y)\phi_\varepsilon(x-y)dy \tag{2.4}$$

If we let $\displaystyle M_k(\phi) = \int_{-\infty}^{\infty} z^k \phi(z)dz$ be the k-th moment of the function ϕ, using a Taylor expansion, we can write the convolution function in $\mathbb{R}$ as Eq. (2.5).

$$(h * \phi_\varepsilon)(x) = \sum_{k=0}^{\infty} \varepsilon^k \frac{h^{(k)}}{k!} M_k(\phi_\varepsilon) \tag{2.5}$$

To ensure that we have an accuracy of fluid velocity evaluated in the region near point force up to order $O(\varepsilon^p)$, we require a blob in 1-D satisfy $M_0(\phi) = 1$, and $M_k(\phi) = 0$ for $k = 1, 2, ..., p-1$. A blob function in $\mathbb{R}^3$ is scaled by volume where $\phi_\varepsilon(\boldsymbol{x}) = \dfrac{1}{\varepsilon^3}\phi_\varepsilon\left(\dfrac{\boldsymbol{x}}{\varepsilon}\right)$. To ensure an accuracy of order $O(\varepsilon^p)$, the same requirement applies to blob functions in 3-D. For a radially symmetric blob function in $\mathbb{R}^3$, the k-th moment of a function ϕ is given by $\displaystyle M_k(\phi) = C(k)\int_0^{\infty} r^{k+2}\phi(r)dr$ where $r = \|\boldsymbol{x}-\boldsymbol{x_0}\|$ for some scaling function $C(k)$. Following the introduction of ϕ_ε, the regularized Green's function, G_ε is defined by Eq. (2.6) and the regularized biharmonic function B_ε is defined by Eq. (2.7) in infinite space [5, 4].

$$\Delta G_\varepsilon = \phi_\varepsilon(\boldsymbol{x}) \tag{2.6}$$

$$\Delta B_\varepsilon = G_\varepsilon(\boldsymbol{x}) \tag{2.7}$$

In this project, we use a blob function with infinite support given by Eq. (2.8) where $r = \|\boldsymbol{x}-\boldsymbol{x_0}\|$.

$$\phi_\varepsilon = \frac{15\varepsilon^4}{8\pi(\varepsilon^2+r^2)^{\frac{7}{2}}} \tag{2.8}$$

Figure 2.1 is a plot of this blob function with different regularization parameter ε. As ε increases, the width of the blob increases and the peak value decreases. Figure 2.2 demonstrates a comparison between forces on a helix in 3-D without and with blobs. Peskin *et al.* employed a blob function with compact support [20] given by Eq. (2.9).

$$\phi_\varepsilon = \begin{cases} \frac{3-2|r|+\sqrt{1+4|r|-4|r^2|}}{8} & |r| \leq 1 \\ \frac{5-2|r|-\sqrt{-7+12|r|-4r^2}}{8} & 1 \geq |r| \leq 2 \\ 0 & |r| \geq 2 \end{cases} \tag{2.9}$$

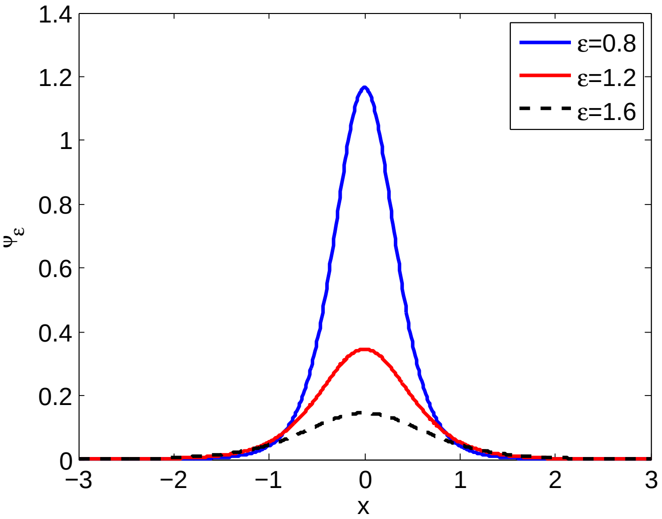

Figure 2.1: Blob in Eq. (2.8) with different regularization parameter ε.

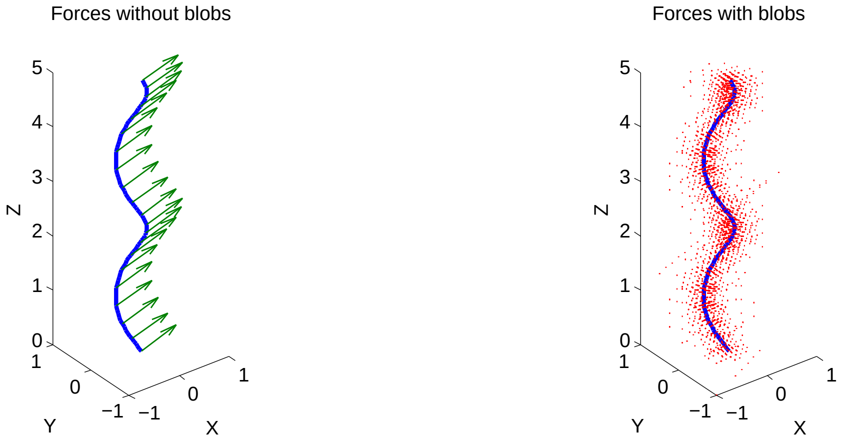

Figure 2.2: Singular forces on structure (left) and regularized forces to spherical support via Eq. (2.8) (right).

Compared to compact support, an infinite support blob makes it easier to compute the singular value numerically. With an infinite support, we are able to choose a blob function such that 95% of the force is concentrated within a critical radius r_c, defined in [6], which generally suffices in engineering applications. Furthermore, in the context of an elastic rod model, the radially symmetric nature of the blob makes it more physically accurate as it spreads the force radially around the centerline of the rod, corresponding to the circular cross-section of the rod.

To derive the Stokeslet, we first take the divergence of both sides of Eq. (2.1) where $\boldsymbol{f} = \boldsymbol{f}_0\phi_\varepsilon$ is regarded as the regularized point force. Then we obtain Eq. (2.10).

$$\nabla \cdot (\nabla p) = \mu \nabla \cdot (\Delta \boldsymbol{u}) + \nabla \cdot \boldsymbol{f_0}\phi_\varepsilon \tag{2.10}$$

Since $\nabla \cdot \boldsymbol{u} = 0$ due to incompressibility, we have $\Delta \boldsymbol{u} = 0$. This gives Eq. (2.11).

$$\Delta p = \nabla \cdot \boldsymbol{f}\phi_\varepsilon \tag{2.11}$$

Applying the vector identity $\nabla \cdot (\phi \boldsymbol{F}) = (\nabla \phi) \cdot \boldsymbol{F} + \phi(\nabla \cdot \boldsymbol{F})$, we obtain Eq. (2.12).

$$\nabla \cdot (\phi_\varepsilon \boldsymbol{f_0}) = \nabla \phi_\varepsilon \cdot \boldsymbol{f_0} + \phi_\varepsilon(\nabla \cdot \boldsymbol{f_0}) \tag{2.12}$$

At every time instant when we are solving for the velocity with a given force $\boldsymbol{f_0}$, $\boldsymbol{f_0}$ can be viewed as constant at each time step, yielding $\nabla \boldsymbol{f_0} = 0$. The equation then simplifies to Eq. (2.13).

$$\Delta p = \nabla \phi_\varepsilon \cdot \boldsymbol{f_0} \tag{2.13}$$

Substituting Eq. (2.6) into Eq. (2.13), we obtain Eq. (2.14), which implies Eq. (2.15), a new pressure expression.

$$\Delta p = \nabla \phi_\varepsilon \cdot \boldsymbol{f_0} = \nabla \cdot (\Delta G_\varepsilon) \cdot \boldsymbol{f_0} = (\boldsymbol{f_0} \cdot \nabla) \cdot \Delta G_\varepsilon = \Delta \cdot (\boldsymbol{f_0} \cdot \nabla G_\varepsilon) \tag{2.14}$$

$$p = \boldsymbol{f_0} \cdot \nabla G_\varepsilon \tag{2.15}$$

Substituting the new pressure expression into Eq. (2.1), we have $\mu \Delta \boldsymbol{u} = (\boldsymbol{f}_0 \cdot \nabla)\nabla G_\varepsilon - \boldsymbol{f_0} \cdot \phi_\varepsilon$, which yields a particular solution for the Stokes equation, given by Eq. (2.16).

$$\mu \boldsymbol{u} = (\boldsymbol{f}_0 \cdot \nabla)\nabla B_\varepsilon(\boldsymbol{x} - \boldsymbol{x_0}) - \boldsymbol{f_0} G_\varepsilon(\boldsymbol{x} - \boldsymbol{x_0}) \tag{2.16}$$

In $\mathbb{R}^3$, Eq. (2.6) expressed in spherical coordinates is given by Eq. (2.17).

$$G''_\varepsilon(r) + \frac{2}{r}G'_\varepsilon(r) = \frac{1}{r^2}[r^2 G'_\varepsilon(r)]' = \phi_\varepsilon \tag{2.17}$$

A solution for $G_\varepsilon(r)$ follows from Eq. (2.17) where $G_\varepsilon(r)$ can be obtained by taking the integral given in Eq. (2.18). Note that $A(r) = \int r^2 \phi_\varepsilon dr$.

$$G_\varepsilon(r) = \int \frac{A(r)}{r^2} dr \tag{2.18}$$

A similar approach can be applied to find $B_\varepsilon(r)$. Using the chosen blob function Eq. (2.8), we find that $G_\varepsilon(r)$ and $B_\varepsilon(r)$ can be expressed in the forms given by Eq. (2.19) and Eq. (2.20). Figure 2.3 shows the graph of regularized Green's function and regularized Biharmonic function with different regularization parameters. $G_\varepsilon(r)$ agrees well with $G(r)$ from $r > 1$.

$$G_\varepsilon(r) = \frac{-3\varepsilon^2 - 2r^2}{8\pi(\varepsilon^2 + r^2)^{\frac{3}{2}}} \tag{2.19}$$

$$B_\varepsilon(r) = \frac{\varepsilon - \sqrt{\varepsilon^2 + r^2}}{8\pi} \tag{2.20}$$

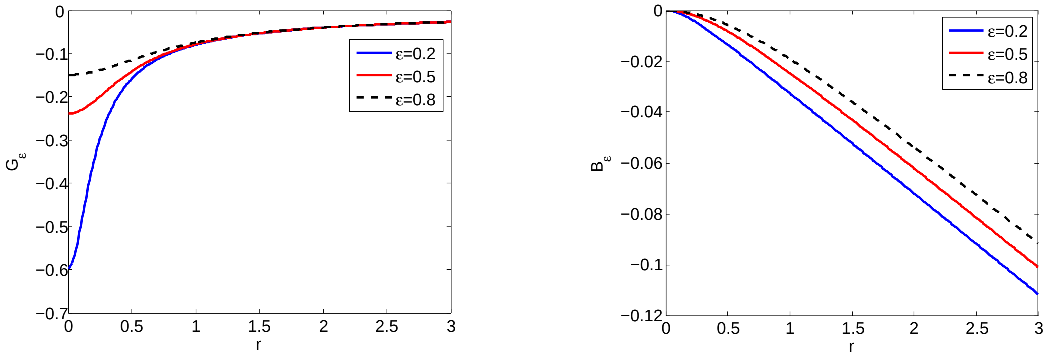

(a) Green's function in Eq. (2.19)

(b) Biharmonic function in Eq. (2.20)

Figure 2.3: Regularized Green's function in Eq. (2.19) and Biharmonic function in Eq. (2.20).

2.2 Material Frame

To describe the movement of an elastic rod immersed in an incompressible Stokes flow, we wish to develop a representation of the rod using its centerline. The centerline of the space curve $\boldsymbol{X}(s,t)$ is parametrized by arc length s and time t. The Frenet frame $(\boldsymbol{n}, \boldsymbol{b}, \boldsymbol{t})$ is intrinsic to the curve itself and captures the curve irrespective of any motion, where $\boldsymbol{t}$ is the unit tangent vector of the curve, $\boldsymbol{n}$ is the normal unit vector, i.e. the derivative of t with respect to the arc length s, and $\boldsymbol{b}$ is the binormal unit vector, chosen to be $\boldsymbol{b} = \boldsymbol{t} \times \boldsymbol{n}$. In a Frenet frame, these three unit vectors are related by Eq. (2.21) where κ represents curvature, τ represents torsion and $'$ denotes derivative with respect to arclength, s.

$$\begin{bmatrix} \boldsymbol{b} \\ \boldsymbol{n} \\ \boldsymbol{t} \end{bmatrix}' = \begin{bmatrix} 0 & -\tau & 0 \\ \tau & 0 & -\kappa \\ 0 & \kappa & 0 \end{bmatrix} \begin{bmatrix} \boldsymbol{b} \\ \boldsymbol{n} \\ \boldsymbol{t} \end{bmatrix} \tag{2.21}$$

While the Frenet frame arises as a natural frame choice for an orthonormal triad, for a physical filament, we wish to develop an orthonormal basis that corresponds to or captures certain material properties of the rod. Here we consider a rotation of the Frenet frame. Specifically, we choose a frame with an orthonormal triad $(\boldsymbol{D}^1, \boldsymbol{D}^2, \boldsymbol{D}^3)$ in such a way that $\boldsymbol{D}^3$ is aligned with tangent vector $\boldsymbol{t}$, $\boldsymbol{D}^1$ is aligned with binormal vector $\boldsymbol{b}$ and $\boldsymbol{D}^2$ has the opposite direction of the normal vector, i.e. $\boldsymbol{D}^2 = -\boldsymbol{n}$. As a result of this new definition, we have $\boldsymbol{D}^1 = \boldsymbol{D}^2 \times \boldsymbol{D}^3$. This new frame is effectively a rotation of the normal and binormal vector in the Frenet frame by $\frac{\pi}{2}$. The rotation can be described by a Darboux vector. Adopting the Darboux frame $(\boldsymbol{D}^1, \boldsymbol{D}^2, \boldsymbol{D}^3)$ as described above, the Darboux vector is given by $\boldsymbol{\Omega} = \kappa_1 \boldsymbol{D}^1 + \kappa_2 \boldsymbol{D}^2 + \kappa_3 \boldsymbol{D}^3$. In this newly established frame, the relation between each pair of orthonormal vectors is given by Eq. (2.22).

$$\begin{bmatrix} \boldsymbol{D}^1 \\ \boldsymbol{D}^2 \\ \boldsymbol{D}^3 \end{bmatrix}' = \begin{bmatrix} 0 & \kappa_3 & -\kappa_2 \\ -\kappa_3 & 0 & \kappa_1 \\ \kappa_2 & -\kappa_1 & 0 \end{bmatrix} \begin{bmatrix} \boldsymbol{D}^1 \\ \boldsymbol{D}^2 \\ \boldsymbol{D}^3 \end{bmatrix} \tag{2.22}$$

In this new material frame, κ_1 is the geodesic curvature, κ_2 is the normal curvature, and τ is the relative torsion. The intrinsic curvature of the rod can be calculated by $\kappa = \sqrt{\kappa_1^2 + \kappa_2^2}$ and the torsion is simply measured by κ_3. Note that the Frenet frame can be viewed as a special case of the new reference frame where $\kappa_1 = \kappa$, $\kappa_2 = 0$ and $\tau = \kappa_3$. The Darboux vector has the following symmetric properties, given by Eq. (2.23a) - Eq. (2.23c). Note that we will employ the Darboux frame as the frame for the Kirchhoff frame.

$$\boldsymbol{D}^{1\prime} = \boldsymbol{\Omega} \times \boldsymbol{D}^1 \tag{2.23a}$$

$$\boldsymbol{D}^{2\prime} = \boldsymbol{\Omega} \times \boldsymbol{D}^2 \tag{2.23b}$$

$$\boldsymbol{D}^{3\prime} = \boldsymbol{\Omega} \times \boldsymbol{D}^3 \tag{2.23c}$$

As stated earlier, this new reference frame is essentially a rotation of the Frenet frame by a certain angle. If we let this angle be ζ, then the two reference frames can be related by Eq. (2.24). It has been verified by the implementation of the above reference frames that when applying a rotation to the rod, it is more preferable to use the Darboux frame with $\zeta \neq 0$. In absence of any rotation, κ_2 can be chosen to be 0, adopting a Frenet frame for simplicity. With this rotation angle ζ, we are also able to relate the curvature and twist in two frame representations together by Eq. (2.25).

$$\begin{bmatrix} \boldsymbol{D}^1 \\ \boldsymbol{D}^2 \\ \boldsymbol{D}^3 \end{bmatrix} = \begin{bmatrix} \cos(\zeta) & \sin(\zeta) & 0 \\ -\sin(\zeta) & \cos(\zeta) & 0 \\ 0 & 0 & 1 \end{bmatrix} \begin{bmatrix} \boldsymbol{n} \\ \boldsymbol{b} \\ \boldsymbol{t} \end{bmatrix} \tag{2.24}$$

$$(\kappa_1, \kappa_2, \kappa_3) = \left(\kappa \sin\zeta, \kappa \cos\zeta, \tau + \frac{d\zeta}{ds} \right) \tag{2.25}$$

We would like to emphasize that there is a subtle difference between twist and torsion, although the two terms have been used interchangably in many contexts. Twist is torsion, but not all torsion is twist. Using the notation above, κ_3 is torsion and τ is twist. When curvature and twist are specified as a vector, namely $\boldsymbol{\Omega}$, if $\tau = 0$, then torsion $\kappa_3 = \frac{d\zeta}{ds}$. In this case, torsion is the rate of rotation of $\boldsymbol{\Omega}$ in the x-y plane with respect to arc length s. If $\tau \neq 0$, an additional rotation of $\boldsymbol{\Omega}$ needs to be accounted for. This additional rotation results from $\tau \neq 0$, which measures the rate of change of twist angle along the length of the rod. Generally, in the case where bending of a rod is significant, it is more preferable to use twist versus torsion. For example, in a helical bending wave, torsion does not equal twist. In a solid rotation, torsion does equal twist. The distinction between these two cases will be discussed in Chapter 4.

A particularly simple example of a curve defined by κ and τ is the circular helix where κ and τ are constants. The standard parameters of such a helix, the radius r and the axial distance of one turn of a helix h are given by Eq. (2.26) and Eq. (2.27) respectively. The arc length of one turn of the helix, S is given by Eq. (2.28) [3].

$$r = \frac{\kappa}{\kappa^2 + \tau^2} \tag{2.26}$$

$$h = \frac{2\pi\tau}{\kappa^2 + \tau^2} \tag{2.27}$$

$$S = \sqrt{(2\pi r)^2 + h^2} \tag{2.28}$$

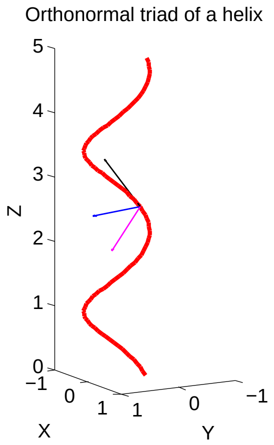

Figure 2.4: Illustration of orthonormal triad on a helix.

A right handed helix starting at the origin with its axis and Darboux vector aligned with z-axis can be produced by $(x(s), y(s), z(s))$ where

$$x(s) = -r\sin\left(\frac{2\pi s}{S}\right) \tag{2.29}$$

$$y(s) = r - r\cos\left(\frac{2\pi s}{S}\right) \tag{2.30}$$

$$z(s) = \frac{hs}{S}. \tag{2.31}$$

Figure 2.4 shows the orthonormal triad defined at a given point on a helix using a Frenet frame. In this example, $\boldsymbol{D}^3$, the unit tangent vector can be given by $\boldsymbol{D}^3 = \dfrac{\boldsymbol{r}'(s)}{\|\boldsymbol{r}'(s)\|}$. Note that employing a Frenet frame, we set $\kappa_2 = 0$. Accordingly, $\boldsymbol{D}^2$ is given by the derivative of $\boldsymbol{D}^3$ with respect to arc length s and $\boldsymbol{D}^1$ is given by the cross product of $\boldsymbol{D}^3$ and $\boldsymbol{D}^2$. The expression of $\boldsymbol{D}^i$ for $i = 1, 2, 3$ is given by Eq. (2.32a), Eq. (2.32b), and Eq. (2.32c).

$$\boldsymbol{D}^3 = \frac{S}{\sqrt{4\pi^2 r^2 + h^2}}\left(-\frac{2\pi r}{S}\cos\left(\frac{2\pi s}{S}\right), \frac{2\pi r}{S}\sin\left(\frac{2\pi s}{S}\right), \frac{h}{S}\right) \tag{2.32a}$$

$$\boldsymbol{D}^2 = \frac{\partial \boldsymbol{D}^3}{\partial s} = \left(\sin\left(\frac{2\pi s}{S}\right), \cos\left(\frac{2\pi s}{S}\right), 0\right) \tag{2.32b}$$

$$\boldsymbol{D}^1 = \boldsymbol{D}^3 \times \boldsymbol{D}^2 \tag{2.32c}$$

An orthonormal triad in the Darboux frame, defined based on the material properties of the rod, can be obtained by simply applying a rotation of this orthonormal triad in Frenet frame.

2.3 Kirchhoff Rod

Rod theories have been applied to understand satellite tethers and biological filaments. Classic Kirchhoff rod theory employs a linear elastic constitutive law for bending and torsion. Constrained

Kirchhoff rod theory imposes two constraints to the rod. First, the Kirchhoff rod is unshearable and inextensible, requiring that

$$\left\|\frac{\partial \boldsymbol{X}}{\partial s}\right\| = 1,$$

where $\boldsymbol{X}$ is the position of the centerline of the rod. The second constraint is that one of the orthonormal triad vectors at each point should be kept aligned with the tangent vector of the rod. The rod is required to satisfy the following equation.

$$\boldsymbol{D}^3 \cdot \frac{\partial \boldsymbol{X}}{\partial s} = 1$$

In this paper, we do not impose these constraints exactly. Instead, we provide forces to keep the value of $\left\|\frac{\partial \boldsymbol{X}}{\partial s}\right\|$ close to 1 and align $\boldsymbol{D}^3$ with the tangent vector at each point. In addition, a Kirchhoff rod satisfies the linear momentum and angular momentum balance equations in the fluid. The force and torque balance are captured by Eq. (2.33) and Eq. (2.34). Note that $\boldsymbol{F}$ and $\boldsymbol{N}$ are the total force and torque on the rod; $\boldsymbol{f}$ and $\boldsymbol{n}$ refer to the force and torque density of the rod. $\boldsymbol{F}$ has a unit of $\frac{m^* L^*}{t^{*2}}$ where m^*, L^* and t^* are the characteristic mass, length and time respectively. $\boldsymbol{N}$ has a unit of $\frac{m^* L^{*2}}{t^{*2}}$. Correspondingly, $\boldsymbol{f}$ has a unit of $\frac{m^*}{t^{*2}}$ and $\boldsymbol{n}$ has a unit of $\frac{m^* L^*}{t^{*2}}$.

$$0 = \boldsymbol{f} + \frac{\partial \boldsymbol{F}}{\partial s} \tag{2.33}$$

$$0 = \boldsymbol{n} + \frac{\partial \boldsymbol{N}}{\partial s} + \left(\frac{\partial \boldsymbol{X}}{\partial s} \times \boldsymbol{F}\right) \tag{2.34}$$

Chapter 3

Mathematical Formulation

3.1 Dynamical Rod Model

Normally, the force would be expressed in the basis of $\{\boldsymbol{i}, \boldsymbol{j}, \boldsymbol{k}\}$ where $\boldsymbol{i}, \boldsymbol{j}$ and $\boldsymbol{k}$ are the unit vectors in the direction of x-, y- and z-axis. Since we wish to capture certain material properties of the rod as mentioned earlier in Section 2.2, we express the internal force $\boldsymbol{F}$ and the moment $\boldsymbol{N}$ of the rod in the basis of the orthonormal triad associated with each point along the length of the rod, i.e. $\{\boldsymbol{D}^1, \boldsymbol{D}^2, \boldsymbol{D}^3\}$, given by Eq. (3.1) and Eq. (3.2) respectively.

$$\boldsymbol{F} = F^1\boldsymbol{D}^1 + F^2\boldsymbol{D}^2 + F^3\boldsymbol{D}^3 \tag{3.1}$$

$$\boldsymbol{N} = N^1\boldsymbol{D}^1 + N^2\boldsymbol{D}^2 + N^3\boldsymbol{D}^3 \tag{3.2}$$

The constitutive relations of the Kirchhoff rod are given by Eq. (3.3a) - Eq. (3.3c) and Eq. (3.4a) - Eq. (3.4c) where a_1 and a_2 are bending moduli about $\boldsymbol{D}^1$ and $\boldsymbol{D}^2$ and where a_3 is the twisting modulus.

$$N^1 = a_1 \frac{\partial \boldsymbol{D}^2}{\partial s} \cdot \boldsymbol{D}^3 \tag{3.3a}$$

$$N^2 = a_2 \frac{\partial \boldsymbol{D}^3}{\partial s} \cdot \boldsymbol{D}^1 \tag{3.3b}$$

$$N^3 = a_3 \frac{\partial \boldsymbol{D}^1}{\partial s} \cdot \boldsymbol{D}^2 \tag{3.3c}$$

$$F^1 = b_1 \boldsymbol{D}^1 \cdot \frac{\partial \boldsymbol{X}}{\partial s} \tag{3.4a}$$

$$F^2 = b_2 \boldsymbol{D}^2 \cdot \frac{\partial \boldsymbol{X}}{\partial s} \tag{3.4b}$$

$$F^3 = b_3 \left(\boldsymbol{D}^3 \cdot \frac{\partial \boldsymbol{X}}{\partial s} - 1 \right) \tag{3.4c}$$

In the case where the rod has a circular cross-section and homogeneous material properites, we let $a_1 = a_2$. The constitutive equations are means by which we enforce the constraints that the rod is inextensible and that $\boldsymbol{D}^3$ is aligned with the tangent vector. Note that orthonormal triads are unitless; curvature and torsion have units of $\frac{1}{L^*}$ where L^* is the characteristic length, as introduced in the previous section. The bending and twist moduli a_1, a_2 and a_3 all have units of $\frac{m^* L^{*3}}{t^{*2}}$ where m^* and

t^* are the characteristic mass and time; the shear and stretch moduli b_1, b_2 and b_3 all have units of $\dfrac{m^*L^*}{t^{*2}}$.

This unconstrained version of Kirchhoff rod model can be derived from an elastic energy of the form given by Eq. (3.5) where $\boldsymbol{\Omega}$ is the intrinsic twist vector of the rod, defined by $\boldsymbol{\Omega} = (\kappa_1, \kappa_2, \kappa_3)$. κ_1 and κ_2 are intrinsic curvature and κ_3 is intrinsic twist.

$$\begin{aligned} E =& \frac{1}{2}\int_0^L \Bigg[a_1 \left(\frac{\partial \boldsymbol{D}^2}{\partial s} \cdot \boldsymbol{D}^3 - \kappa_1 \right)^2 + a_2 \left(\frac{\partial \boldsymbol{D}^3}{\partial s} \cdot \boldsymbol{D}^1 - \kappa_2 \right)^2 + a_3 \left(\frac{\partial \boldsymbol{D}^1}{\partial s} \cdot \boldsymbol{D}^2 - \kappa_3 \right)^2 \\ &+ b_1 \left(\boldsymbol{D}^1 \cdot \frac{\partial \boldsymbol{X}}{\partial s} \right)^2 + b_2 \left(\boldsymbol{D}^2 \cdot \frac{\partial \boldsymbol{X}}{\partial s} \right)^2 + b_3 \left(\boldsymbol{D}^3 \cdot \frac{\partial \boldsymbol{X}}{\partial s} - 1 \right)^2 \Bigg] ds \end{aligned} \tag{3.5}$$

Note that Eq. (3.5) is formulated based on Eq. (3.6a) - Eq. (3.6c). Since Eq. (3.6a) and Eq. (3.6b) yield parameters of curvature and Eq. (3.6c) gives parameter of twist, the energy will be minimized when the rod achieves its intrinsic twist configuration defined by $\boldsymbol{\Omega}$. Eq. (3.6a) - Eq. (3.6c) are specific to the Darboux frame and are simplified using the property $\boldsymbol{D}^i \cdot \boldsymbol{D}^j = \delta_{ij}$.

$$\frac{\partial \boldsymbol{D}^2}{\partial s} \cdot \boldsymbol{D}^3 = (-\kappa_3 \boldsymbol{D}^1 + \kappa_1 \boldsymbol{D}^3) \cdot \boldsymbol{D}^3 = \kappa_1 \tag{3.6a}$$

$$\frac{\partial \boldsymbol{D}^3}{\partial s} \cdot \boldsymbol{D}^1 = (\kappa_2 \boldsymbol{D}^1 - \kappa_1 \boldsymbol{D}^2) \cdot \boldsymbol{D}^1 = \kappa_2 \tag{3.6b}$$

$$\frac{\partial \boldsymbol{D}^1}{\partial s} \cdot \boldsymbol{D}^2 = (\kappa_3 \boldsymbol{D}^2 - \kappa_2 \boldsymbol{D}^3) \cdot \boldsymbol{D}^2 = \kappa_3 \tag{3.6c}$$

3.2 Stokeslet and Rotlet

In this model, we wish to couple the motion of the rod to its fluid environment. This is done by assuming a no-slip condition where the rod is moving at a velocity equal to the fluid velocity at that point. Each point in the fluid is acted upon by both a point force and a point torque. As a result of this torque, a given point in the fluid possesses not only a linear velocity, but also an angular velocity. The angular velocity at a given point contributes to the rotation of the orthonormal triad at that point. Therefore, the no-slip condition in our model applies for both linear velocity $\boldsymbol{u}$ and angular velocity $\boldsymbol{\omega}$ given by Eq. (3.7) and Eq. (3.8) respectively [19].

$$\frac{\partial \boldsymbol{X}(s,t)}{\partial t} = \boldsymbol{u}(\boldsymbol{X}(s,t),t) \tag{3.7}$$

$$\frac{\partial \boldsymbol{D}^i(s,t)}{\partial t} = \boldsymbol{\omega}(\boldsymbol{X}(s,t),t) \times \boldsymbol{D}^i(s,t), \quad i = 1,2,3 \tag{3.8}$$

The linear velocity and angular velocity at any point in the fluid domain are solved using the constitutive relation for a given force at each time step. In this model, considering the presence of torque, we let the force function at each point be defined by Eq. (3.9) [19].

$$\boldsymbol{f} = \boldsymbol{g_0}\phi_\varepsilon(\boldsymbol{x} - \boldsymbol{X}_0) + \frac{1}{2}\nabla \times \boldsymbol{m_0}\phi_\varepsilon(\boldsymbol{x} - \boldsymbol{X_0}) \tag{3.9}$$

We let G_ε represent the regularized Green's function and B_ε represent the regularized biharmonic function, as defined by Eq. (2.6) and Eq. (2.7) in Section 2.1. Let both G_ε and B_ε be functions of

r where $r = \|\boldsymbol{x} - \boldsymbol{X}_0\|$ and $\boldsymbol{X}_0$ is a given point on the rod. Substituting Eq. (3.9) into Eq. (2.1) and taking the divergence of both sides of the Stokes equation with the substitution of the force gives Eq. (3.10). Similar to the derivation from Eq. (2.11) to Eq. (2.13), we obtain the same pressure representation given by Eq. (2.15) derived in Section 2.1 for the case in which only force is applied at a point.

$$\nabla \cdot (\nabla p) = \mu\Delta \cdot (\Delta \boldsymbol{u}) + \nabla \cdot (\boldsymbol{f_0}\phi_\varepsilon + \frac{1}{2} \times \boldsymbol{n_0}\phi_\varepsilon) \tag{3.10}$$

Now substitute the pressure representation Eq. (2.15) into Eq. (2.1). We obtain a particular solution to the Stokes equation with both applied force and torque.

$$\mu\Delta\boldsymbol{u} = \nabla p - \boldsymbol{f_0}\phi_\varepsilon - \frac{1}{2}\nabla \times \boldsymbol{n_0}\phi_\varepsilon$$

$$\mu\Delta\boldsymbol{u} = \nabla(\boldsymbol{f_0} \cdot \nabla G_\varepsilon) - \boldsymbol{f_0}\phi_\varepsilon - \frac{1}{2}\nabla \times (\boldsymbol{n_0}\phi_\varepsilon).$$

Using the vector identity $\nabla \times (\phi\boldsymbol{A}) = \phi\nabla \times \boldsymbol{A} - \boldsymbol{A} \times \nabla\phi$, we now have $\nabla \times (\boldsymbol{n_0}\phi) = \phi_\varepsilon\nabla \times \boldsymbol{n_0} - \boldsymbol{n_0} \times \nabla\phi_\varepsilon$. We treat $\boldsymbol{n_0}$ as a constant at each time step, similar to $\boldsymbol{f_0}$, and substitute Eq. (2.6) and Eq. (2.7) in the particular solution above. We obtain

$$\mu\Delta\boldsymbol{u} = \nabla(\boldsymbol{f_0} \cdot \nabla(\Delta B_\varepsilon)) - \boldsymbol{f_0}\Delta G_\varepsilon - \frac{1}{2}\nabla(\Delta G_\varepsilon) \times \boldsymbol{n_0}.$$

By definition,

$$-\frac{1}{2}\nabla(\Delta G_\varepsilon) \times \boldsymbol{n_0} = -\frac{1}{2}\nabla \cdot (\nabla \cdot \nabla G_\varepsilon) \times \boldsymbol{n_0} = -\frac{1}{2}(\nabla \cdot \nabla) \cdot \nabla G_\varepsilon \times \boldsymbol{n_0} = -\frac{1}{2}\Delta(\nabla G_\varepsilon) \times \boldsymbol{n_0}.$$

This gives

$$\mu\Delta\boldsymbol{u} = \nabla(\boldsymbol{f_0} \cdot \nabla(\Delta B_\varepsilon)) - \boldsymbol{f_0}\Delta G_\varepsilon - \frac{1}{2}\Delta(\nabla G_\varepsilon) \times \boldsymbol{n_0}.$$

A simplified particular solution for linear velocity and pressure is thus obtained, given by Eq. (3.11a) and Eq. (3.11d) respectively. The linear velocity $\boldsymbol{u}$ provides knowledge about the motion of the centerline of the rod as well as any other points in the fluid domain. We call $\boldsymbol{u}_S[\boldsymbol{f}]$ in Eq. (3.11b) the regularized Stokeslet from point force and $\boldsymbol{u}_R[\boldsymbol{n}]$ in Eq. (3.11b) the regularized Rotlet from point torque. Adding them together gives the linear velocity [19].

$$\boldsymbol{u} = \boldsymbol{u}_S[\boldsymbol{f}] + \boldsymbol{u}_R[\boldsymbol{n}] \tag{3.11a}$$

$$\boldsymbol{u}_S[\boldsymbol{f}] = \frac{1}{\mu}(\boldsymbol{f_0} \cdot \nabla) \cdot \nabla B_\varepsilon(\boldsymbol{x} - \boldsymbol{X_0}) - \boldsymbol{f_0}G_\varepsilon(\boldsymbol{x} - \boldsymbol{X_0}) \tag{3.11b}$$

$$\boldsymbol{u}_R[\boldsymbol{n}] = \frac{1}{2\mu}\boldsymbol{n}_0 \times \nabla G_\varepsilon \tag{3.11c}$$

$$p = \boldsymbol{f_0} \cdot \nabla G_\varepsilon(\boldsymbol{x} - \boldsymbol{X_0}) \tag{3.11d}$$

We now derive the solution for angular velocity at each point. The angular velocity and linear velocity at each point are related by Eq. (3.12).

$$\mu\boldsymbol{\omega} = \frac{1}{2}\nabla \times (\mu\boldsymbol{u}) \tag{3.12}$$

Since we have already obtained a particular solution for $\boldsymbol{u}$, we substitute this particular solution, i.e. Eq. (3.11a) into Eq. (3.12), obtaining

$$\mu\boldsymbol{\omega} = \frac{1}{2}\nabla \times \left[(\boldsymbol{f_0} \cdot \nabla) \cdot \nabla B_\varepsilon(\boldsymbol{x} - \boldsymbol{X_0}) - \boldsymbol{f_0} G_\varepsilon(\boldsymbol{x} - \boldsymbol{X_0}) + \frac{1}{2}\boldsymbol{n_0} \times \nabla G_\varepsilon) \right].$$

Since curl of any gradient is zero, we have

$$\frac{1}{2}\nabla \times [(\boldsymbol{f_0} \cdot \nabla) \cdot \nabla B_\varepsilon(\boldsymbol{x} - \boldsymbol{X_0})] = 0.$$

By definition,

$$-\frac{1}{2}\nabla \times [\boldsymbol{f_0} \cdot G_\varepsilon(\boldsymbol{x} - \boldsymbol{X_0})] = -\frac{1}{2}\left[G_\varepsilon(\boldsymbol{x} - \boldsymbol{X_0}) \cdot (\nabla \times \boldsymbol{f_0}) - \boldsymbol{f_0} \times \nabla G_\varepsilon(\boldsymbol{x} - \boldsymbol{X_0}) \right].$$

Substitution of these two new expressions into the angular velocity representation gives

$$\mu\boldsymbol{\omega} = -\frac{1}{2}\left[G_\varepsilon(\boldsymbol{x} - \boldsymbol{X_0}) \cdot (\nabla \times \boldsymbol{f_0}) - \boldsymbol{f_0} \times \nabla G_\varepsilon(\boldsymbol{x} - \boldsymbol{X_0}) \right] - \frac{1}{4}\nabla \times (\nabla G_\varepsilon \times \boldsymbol{n_0}).$$

Since $\boldsymbol{f_0}$ is regarded as a constant, $\nabla \times \boldsymbol{f_0} = 0$. Using the vector identity $\boldsymbol{A} \times (\boldsymbol{B} \times \boldsymbol{C}) = (\boldsymbol{A} \cdot \boldsymbol{C}) \cdot \boldsymbol{B} - (\boldsymbol{A} \times \boldsymbol{B}) \times \boldsymbol{C}$, we rewrite the last term of the above equation with further simplification, obtaining

$$\mu\boldsymbol{\omega} = \frac{1}{2}\boldsymbol{f_0} \times \nabla G_\varepsilon(\boldsymbol{x} - \boldsymbol{X_0}) + \frac{1}{4}\boldsymbol{n_0} \cdot \Delta G_\varepsilon - \frac{1}{4}(\boldsymbol{n_0} \cdot \nabla)\nabla G_\varepsilon.$$

Finally, we substitute the definition of regularized Green's function given by Eq. (2.6) into the above equation. The angular velocity at a given point is given by Eq. (3.13a). We call $\boldsymbol{u}_R[\boldsymbol{f}]$ in Eq. (3.13b) the regularized Rotlet from point force and $\boldsymbol{u}_S[\boldsymbol{n}]$ in Eq. (3.13c) the regularized Dipole from point torque [19].

$$\boldsymbol{\omega} = \boldsymbol{u}_R[\boldsymbol{f}] + \boldsymbol{u}_S[\boldsymbol{n}] \tag{3.13a}$$

$$\boldsymbol{u}_R[\boldsymbol{f}] = \frac{1}{2\mu}\boldsymbol{f_0} \times \nabla G_\varepsilon(\boldsymbol{x} - \boldsymbol{X_0}) \tag{3.13b}$$

$$\boldsymbol{u}_S[\boldsymbol{n}] = \frac{1}{4}\boldsymbol{n_0} \cdot \phi_\varepsilon - \frac{1}{4}(\boldsymbol{n_0} \cdot \nabla)\nabla G_\varepsilon \tag{3.13c}$$

As stated in Section 2.1, we choose a blob function with infinite support, given by Eq. (2.8). This equation satisfies $4\pi \int_0^\infty r^2 \phi_\varepsilon(r) dr = 1$ and $M_2(k) = 4\pi \int_0^\infty r^4 \phi_\varepsilon(r) dr = \frac{3}{2}\varepsilon^2$ which represents the second moment of ϕ_ε, ensuring that as $\varepsilon \to 0$, the blob function approaches an accuracy of $\delta(\varepsilon^2)$ [18]. The explicit form of regularized p, $\boldsymbol{u}$ and $\boldsymbol{\omega}$ using the chosen blob function can be obtained by substituting the blob into the particular solution of velocity. Note that substituting $\phi_\varepsilon(r)$ into Eq. (3.11a) requires a change of variable from r to $\boldsymbol{x} - \boldsymbol{X_0}$ with $r = \|\boldsymbol{x} - \boldsymbol{X_0}\|$ through differentiation given in Eq. (3.14)

$$dr = \frac{\boldsymbol{x} - \boldsymbol{X_0}}{r} d\boldsymbol{x} \tag{3.14}$$

Using Eq. (3.14), we apply chain rule to Eq. (3.11a), obtaining

$$\begin{aligned}(\boldsymbol{f_0}\cdot\nabla)\cdot\nabla B_\varepsilon(\boldsymbol{x}-\boldsymbol{X_0}) &= (\boldsymbol{f_0}\cdot\nabla)\cdot\left[\frac{(\boldsymbol{x}-\boldsymbol{X_0})}{r}B'_\varepsilon(r)\right]\\ &= \boldsymbol{f_0}\cdot\nabla\left[\frac{(\boldsymbol{x}-\boldsymbol{X_0})}{r}B'_\varepsilon(r)\right]\\ &= \boldsymbol{f_0}\cdot\left[(\boldsymbol{x}-\boldsymbol{X_0})\cdot(\boldsymbol{x}-\boldsymbol{X_0})\frac{rB''_\varepsilon - B'_\varepsilon}{r^3}+\frac{B'_\varepsilon}{r}\right].\end{aligned}$$

Also, we have

$$\frac{d}{d\boldsymbol{x}}\left(\frac{B'_\varepsilon}{r}\right)=\frac{(\boldsymbol{x}-\boldsymbol{X_0})}{r}\frac{(rB''_\varepsilon - B'_\varepsilon)}{r^2}=(\boldsymbol{x}-\boldsymbol{X_0})\frac{rB''_\varepsilon - B'_\varepsilon}{r^3}.$$

Combining and further simplifying the expressions above yield a regularized linear velocity, given by Eq. (3.15).

$$\begin{aligned}\mu\boldsymbol{u} &= \boldsymbol{f_0}\cdot\left[(\boldsymbol{x}-\boldsymbol{X_0})\cdot(\boldsymbol{x}-\boldsymbol{X_0})\frac{rB''_\varepsilon - B'_\varepsilon}{r^3}+\frac{B'_\varepsilon}{r}\right]-\boldsymbol{f_0}G_\varepsilon+\frac{1}{2}\boldsymbol{n_0}\times(\boldsymbol{x}-\boldsymbol{X_0})\frac{G'_\varepsilon}{r} \\ &= \boldsymbol{f_0}\left(\frac{B'_\varepsilon}{r}-G_\varepsilon\right)+\boldsymbol{f_0}\cdot\left[(\boldsymbol{x}-\boldsymbol{X_0})\cdot(\boldsymbol{x}-\boldsymbol{X_0})\frac{rB''_\varepsilon - B'_\varepsilon}{r^3}\right]+\frac{1}{2}\boldsymbol{n_0}\times(\boldsymbol{x}-\boldsymbol{X_0})\frac{G'_\varepsilon}{r}\end{aligned} \tag{3.15}$$

Through a similar approach, we can obtain the explicit form of angular velocity given by Eq. (3.16).

$$\mu\boldsymbol{\omega}=\frac{1}{2}\left[\boldsymbol{f_0}\times(\boldsymbol{x}-\boldsymbol{X_0})\right]\frac{G'_\varepsilon}{r}+\frac{1}{4}\boldsymbol{n_0}\left(-\frac{G'_\varepsilon}{r}+\phi_\varepsilon\right)+\frac{1}{4}\left[\boldsymbol{n_0}\cdot(\boldsymbol{x}-\boldsymbol{X_0})\right]\cdot(\boldsymbol{x}-\boldsymbol{X_0})\left(\frac{rG''_\varepsilon - G'_\varepsilon}{r^3}\right) \tag{3.16}$$

3.3 Numerical Scheme

To solve the motion of a Kirchhoff rod in Stokes flow, we need to choose a numerical scheme. First, we discretize the centerline of the rod into M points, with a constant length of interval between each pair of points, represented by Δs. If the rod has a length of L, then $\Delta s = \dfrac{L}{M-1}$. Let s_k denote the k-th point on the rod for $k = 1, 2, ..., M$, with $s_k = k\Delta s$. As a result of this discretization, the integral in the energy formulation is calculated by Eq. (3.17).

$$\begin{aligned}E =&\frac{1}{2}\sum_{i=1}^{M-1}\Bigg[a_1\left(\frac{\partial\boldsymbol{D}^2}{\partial s}\cdot\boldsymbol{D}^3-\kappa_1\right)^2+a_2\left(\frac{\partial\boldsymbol{D}^3}{\partial s}\cdot\boldsymbol{D}^1-\kappa_2\right)^2+a_3\left(\frac{\partial\boldsymbol{D}^1}{\partial s}\cdot\boldsymbol{D}^2-\kappa_3\right)^2\\ &+b_1\left(\boldsymbol{D}^1\cdot\frac{\partial\boldsymbol{X}}{\partial s}\right)^2+b_2\left(\boldsymbol{D}^2\cdot\frac{\partial\boldsymbol{X}}{\partial s}\right)^2+b_3\left(\boldsymbol{D}^3\cdot\frac{\partial\boldsymbol{X}}{\partial s}-1\right)^2\Bigg]\Delta s\end{aligned} \tag{3.17}$$

The variables $\boldsymbol{X}$, $\boldsymbol{D}^1$, $\boldsymbol{D}^2$, $\boldsymbol{D}^3$, $\boldsymbol{F}$, $\boldsymbol{N}$, $\boldsymbol{f}$ and $\boldsymbol{n}$ will be defined at points s_k for integer values of k. Besides the integer-value boundary points, the variables $\boldsymbol{X}$, $\boldsymbol{D}^1$, $\boldsymbol{D}^2$, $\boldsymbol{D}^3$, $\boldsymbol{F}$ and $\boldsymbol{N}$ will also be defined at $s_{k+\frac{1}{2}}$ for half-integer values, i.e. the mid-point between s_k and s_{k+1}. The force $\boldsymbol{F}$ is computed using Eq. (3.18) where F^i for $i = 1, 2, 3$ is computed via Eq. (3.19). Moment $\boldsymbol{N}$ is computed using Eq. (3.20) where N^1, N^2 and N^3 are computed via Eq. (3.21a) - Eq. (3.21c).

$$\boldsymbol{F}_{k+\frac{1}{2}}=\sum_{i=1}^{3}F^j_{k+\frac{1}{2}}\boldsymbol{D}^j_{k+\frac{1}{2}} \tag{3.18}$$

$$F^{j}_{k+\frac{1}{2}} = b_i \left(\boldsymbol{D}^{\boldsymbol{j}}_{\boldsymbol{k+\frac{1}{2}}} \cdot \frac{\boldsymbol{X_{k+1}} - \boldsymbol{X_k}}{\Delta s} - \delta_{3i} \right) \tag{3.19}$$

$$\boldsymbol{N}_{k+\frac{1}{2}} = \sum_{i=1}^{3} N_{k+\frac{1}{2}}{}^{j} \boldsymbol{D}^{j}_{k+\frac{1}{2}} \tag{3.20}$$

$$N^{1}_{k+\frac{1}{2}} = a_1 \left(\frac{\boldsymbol{D}^2_{k+1} - \boldsymbol{D}^2_k}{\Delta s} \cdot \boldsymbol{D}_{k+\frac{1}{2}} - \kappa_1 \right) \tag{3.21a}$$

$$N^{2}_{k+\frac{1}{2}} = a_2 \left(\frac{\boldsymbol{D}^3_{k+1} - \boldsymbol{D}^3_k}{\Delta s} \cdot \boldsymbol{D}_{k+\frac{1}{2}} - \kappa_2 \right) \tag{3.21b}$$

$$N^{3}_{k+\frac{1}{2}} = a_3 \left(\frac{\boldsymbol{D}^1_{k+1} - \boldsymbol{D}^1_k}{\Delta s} \cdot \boldsymbol{D}_{k+\frac{1}{2}} - \kappa_3 \right) \tag{3.21c}$$

Since $\boldsymbol{F}$ and $\boldsymbol{N}$ need to be evaluated at half-integer boundary points in our discretization scheme, a rotation matrix is needed to produce the orthonormal triad at half-integer boundary points from the orthonormal triad at integer boundary points. We wish to find a rotation matrix A such that $\boldsymbol{D}^i_{k+1} = A\boldsymbol{D}^i_k$ where $\boldsymbol{D}^i_k$ is the orthonormal triad for $i = 1, 2, 3$ at a given point s_k along the rod. The matrix A functions to rotate $\boldsymbol{D}^i_k$ to yield $\boldsymbol{D}^i_{k+1}$. To find A, we first have the relation between a consecutive pair of boundary points.

$$\begin{aligned} \boldsymbol{D}^i_{k+1} &= \boldsymbol{D}^i_{k+1} I \\ &= \boldsymbol{D}^i_{k+1} \left((\boldsymbol{D}^i_k)^T \boldsymbol{D}^i_k \right) \\ &= (\boldsymbol{D}^i_{k+1} (\boldsymbol{D}^i_k)^T) \boldsymbol{D}^i_k \end{aligned}$$

This implies that A could be given by Eq. (3.22). If we wish to obtain the orthonormal triad at half-integer boundary points, we only need to require that the rotation angle be half of those of integer-value boundary points. Let this half-angle rotation matrix be represented by A'. Then A and A' satisfy $A'A' = A$ where $A' = \sqrt{A}$ is the principal square root of A. Hence, the orthonormal triad at a half-integer boundary point between s_k and s_{k+1} can be given by Eq. (3.23).

$$A = \boldsymbol{D}^i_{k+1} (\boldsymbol{D}^{\boldsymbol{i}}_{\boldsymbol{k}})^T \tag{3.22}$$

$$\boldsymbol{D}^i_{k+\frac{1}{2}} = \sqrt{A} \boldsymbol{D}^i_k \tag{3.23}$$

As we discretize the rod into M points, the body force of the rod is computed using a summation given by Eq. (3.24) where $\boldsymbol{f}_k$ and $\boldsymbol{n}_k$ are discretized via Eq. (3.25a) and Eq. (3.25b).

$$\boldsymbol{f}(x) = \sum_{k=1}^{M} -\boldsymbol{f}_k \phi_\varepsilon(\boldsymbol{x} - \boldsymbol{X}_k) \Delta s + \frac{1}{2} \nabla \times \sum_{k=1}^{M} -\boldsymbol{n}_k \phi_\varepsilon(\boldsymbol{x} - \boldsymbol{X}_k) \Delta s \tag{3.24}$$

$$-\boldsymbol{f}_k = \frac{\boldsymbol{F}_{k+\frac{1}{2}} - \boldsymbol{F}_{k-\frac{1}{2}}}{\Delta s} \tag{3.25a}$$

$$-\boldsymbol{n}_k = \frac{\boldsymbol{N}_{k+\frac{1}{2}} - \boldsymbol{N}_{k-\frac{1}{2}}}{\Delta s} + \frac{1}{2} \left(\frac{\boldsymbol{X}_{k+1} - \boldsymbol{X}_k}{\Delta s} \times \boldsymbol{F}_{k+\frac{1}{2}} + \frac{\boldsymbol{X}_k - \boldsymbol{X}_{k-1}}{\Delta s} \times \boldsymbol{F}_{k-\frac{1}{2}} \right) \tag{3.25b}$$

Given the discretized force, we compute the linear and angular velocity solution of the Stokes equation using Eq. (3.26) and Eq. (3.27) respectively. Note that $\boldsymbol{u}_S[-\boldsymbol{f}_k\Delta s]$ and $\boldsymbol{u}_R[-\boldsymbol{n}_k\Delta s]$ are the regularized Stokeslet and Rotlet from the point force and torque; $\boldsymbol{u}_R[-\boldsymbol{f}_k\Delta s]$ and $\boldsymbol{u}_D[-\boldsymbol{n}_k\Delta s]$ are the regularized Rotlet and Dipole from the point force and torque.

$$\boldsymbol{u}(\boldsymbol{x}) = \frac{1}{\mu}\sum_{k=1}^{M}\boldsymbol{u}_S[-\boldsymbol{f}_k\Delta s] + \frac{1}{\mu}\sum_{k=1}^{M}\boldsymbol{u}_R[-\boldsymbol{n}_k\Delta s] \tag{3.26}$$

$$\boldsymbol{\omega}(\boldsymbol{x}) = \frac{1}{\mu}\sum_{k=1}^{M}\boldsymbol{u}_R[-\boldsymbol{f}_k\Delta s] + \frac{1}{\mu}\sum_{k=1}^{M}\boldsymbol{u}_D[-\boldsymbol{n}_k\Delta s] \tag{3.27}$$

$$\boldsymbol{X}_k^{n+1} = \boldsymbol{X}_k^n + \boldsymbol{u}(\boldsymbol{X}_k^n)\Delta t \tag{3.28}$$

$$\begin{aligned}\boldsymbol{v}_{rot} &= R(\boldsymbol{k},\theta)\boldsymbol{v} \qquad (3.29)\\ &= \boldsymbol{v}\mathrm{cos}\theta + (\boldsymbol{v}\times\boldsymbol{v})\mathrm{sin}\theta + \boldsymbol{k}(\boldsymbol{k}\cdot\boldsymbol{v})(1-\mathrm{cos}\theta)\\ &= (\boldsymbol{I}\mathrm{cos}\theta)\boldsymbol{v} + (\mathrm{sin}\theta\boldsymbol{k}\times)\boldsymbol{v} + (1-\mathrm{cos}\theta)\boldsymbol{k}\boldsymbol{k}^T\boldsymbol{v}\end{aligned}$$

$$(\boldsymbol{D}_k^i) = R\left(\frac{\boldsymbol{\omega}\boldsymbol{X}_{\boldsymbol{k}}^{\boldsymbol{n}}}{\|\boldsymbol{\omega}\boldsymbol{X}_{\boldsymbol{k}}^{\boldsymbol{n}}\|}, \|\boldsymbol{\omega}\boldsymbol{X}_{\boldsymbol{k}}^{\boldsymbol{n}}\|\Delta t\right)(\boldsymbol{D}_k^i)^n \tag{3.30}$$

The linear velocity at each point in the fluid domain is updated using Euler's method, given by Eq. (3.28). The angular velocity is updated based on the updated linear velocity via its definition, given by Eq. (3.12) in Section 3.2. Changes in angular velocity at an immersed boundary point contribute to changes in its corresponding orthonormal triads. To update the orthonormal triad at a given boundary point, we apply Rodrigues' rotation formula, represented by $R(\boldsymbol{k},\theta)$ where $\boldsymbol{k}$ points in the direction of the rotation axis and θ is the rotation angle. Rodrigues' rotation formula is an efficient algorithm for rotating a vector in space given an axis of rotation and a rotation angle. If we let $\boldsymbol{v_{rot}}$ represent the vector obtained after rotation and $\boldsymbol{I}$ be the 3×3 Identity matrix, then the updated vector is calculated by Eq. (3.29). The update of the orthonormal triad at the immersed boundary points is given by Eq. (3.30) using Rodrigues' formula.

Chapter 4

Analysis

4.1 Material Properties and Energy

The ability of the rod to bend, twist and stretch affects the movement of the rod in a given fluid flow. To analyze the effect of material properties, i.e. a_i and b_i in Eq. (3.3) and Eq. (3.4) on the movement of the rod, parameters including bending, twisting, shearing and stretching modulus were varied to determine their influence on the energy profile and equilibrium state of the rod. We initialize the rod as straight with two free ends and enforce a preferred curvature κ and twist τ. Eq. (4.1a) - Eq. (4.1d) show the initial condition of the rod and the orthonormal triad at each point in our simulation where Δs is the distance between each consecutive pair of immersed boundary points and $k = \{0, 1, 2, ..., M-1\}$ for M immersed boundary points. Table 4.1 shows the set of basic parameters used in our simulations.

$$\boldsymbol{X}(s) = (0, 0, k\Delta s) \tag{4.1a}$$
$$\boldsymbol{D}^1 = (1, 0, 0) \tag{4.1b}$$
$$\boldsymbol{D}^2 = (0, 1, 0) \tag{4.1c}$$
$$\boldsymbol{D}^3 = (0, 0, 1) \tag{4.1d}$$

Note that in all the simulations in this section, we prescribe the rod with an intrinsic twist vector that defines a helix. From Eq. (4.2) and Eq. (4.3), we can compute the radius r and the axial distance h of the helix using the prescribed curvature κ and twist τ. Initialized as straight, the rod will attempt to achieve its assigned configuration driven by the minimizing energy. Note that in the energy formulation given in Eq. (3.5), the magnitude of force and moment that drive the configuration change of the rod is set up to minimize the difference between the preferred and actual curvature and twist.

Table 4.1: Basic parameters

Parameter	Value	Unit
Time step Δt	1×10^{-7}	s
IB spacing Δs	0.1	μm
Number of IB points M	100	—
Regularization parameter ε	0.5	μm
Fluid viscosity μ	8.9×10^{-7}	$dag \mu m^{-1} s^{-1}$

$$r = \frac{\kappa}{\kappa^2 + \tau^2} \tag{4.2}$$

$$h = \frac{2\pi\tau}{\kappa^2 + \tau^2} \tag{4.3}$$

In the following simulations, we vary each modulus one at a time and examine the effect of changing each modulus on time for the rod to reach an equilibrium state and its energy profile. Table 4.2 is a set of standard parameters [19], which will be used as a reference to compare with in the following simulations. First, we explore the impact of changing different moduli on the time process for a free rod to reach an equilibrium configuration, given a preferred intrinsic twist vector corresponding to a helix as described above. Figure 4.1 (a) shows the configuration of the rod at $t = 4 \times 10^{-5}$ s, which is initialized as a straight and free. Using the standard parameter set in Table 4.2, a rod is initialized as straight rod and κ_1, κ_2 and τ are set corresponding to a helix. Figure 4.1 (b) shows the configuration of the rod when the energy of the rod falls below 10^{-4} fJ. Figure 4.1 (c) shows the prescribed configuration of the rod. Comparing Figure 4.1 (b) with Figure 4.1 (c), we see that the achieved configuration agrees with the prescribed configuration, showing that the equilibrium is stable. Note that Figure 4.1 (b) is the configuration achieved by the rod at $t = 0.0062$s. The energy will continue to be minimized if the simulations are run for a longer time period in which case, the rod will assume a configuration that agrees better with Figure 4.1 (c). The black arrows on the rod are the velocity vectors at each immersed boundary point.

Table 4.3 shows a series of times it takes a free rod to reach a new equilibrium with an increasing bending modulus. The rod is given a preferred strain twist vector and other modulus values from Table 4.2 (the standard parameter set). We set the stop criterion of our simulations to be $E \leq 10^{-2}$ fJ (femtojoule where 1 fJ $= 1 \times 10^{-15}$ J). Note that for mass, we use decagram where $1dag = 10g$. Despite the fact that the rod might not achieve 100% equilibrium, assuming an exactly identical shape with the prescribed configuration, the energy is monotonically decreasing throughout the process. We use the time to reach $E = 10^{-2}$ fJ in each case as a metric of time it takes for a rod to reach equilibrium. In other simulations where the energy of the rod is comparably higher, we consider equilibrium to be achieved when the rod becomes relatively static. As we can see from Table 4.3, as bending modulus increases, the time to reach equilibrium increases. This can be explained by the fact that as the material of the rod becomes increasingly resistant to bending, it is more difficult for the rod to bend and therefore takes longer for the rod to reach its equilibrium configuration.

Table 4.4 shows the the time it takes for a free rod to reach an equilibrium with an increasing twist modulus, given the same preferred strain twist vector from the standard parameter set. Shown in the table, as the twist modulus of the rod increases, the time to reach equilibrium decreases. This is due to the fact that the twist value implemented falls within the regime where increasing the twist modulus increases the rod's ability to achieve its prescribed configuration. Note that when the twist modulus is below a certain value, the rod could be too flexible to bend to its prescribed configuration. To illustrate the existence of different regimes, we run this simulation with an additional set of twist moduli. Note that when the twist modulus is increased from 25.5 to 27.5, the time to reach equilibrium increases, implying that the rod is within a regime where increasing twist modulus restrains the rod from reaching equilibrium. When the twist modulus is increased from 35.5 to 37.5, the time to reach equilibrium again decreases within this modulus interval. However, we note that time to reach equilibrium increases compared to the $a_3 \in$(35.5,37.5) regime. Hence, we conclude that there exist different regimes in which twist modulus has different effects on the rod's ability to reach equilibiurm. We note that compared to twist modulus, the effect of bending modulus on time to reach equilibrium varies less in the regime of our test as bending modulus changes. Over the range of bending modulus we implement in our

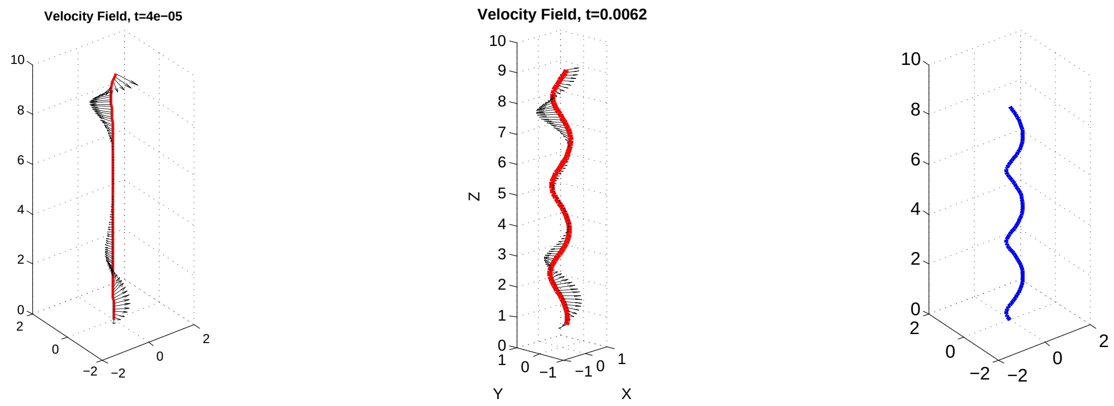

(a) Initial configuration of the rod (b) Achieved configuration (c) Prescribed configuration

Figure 4.1: A rod achieves a helical equilibrium given a preferred curvature and twist. The black arrows are velocity vectors at each immersed boundary point.

simulation, we observe a positive correlation between bending modulus and time to reach equilibrium, suggesting that with our current parameter set, we are in a regime where bending modulus is more critical to the ability of the rod to achieve its prescribed configuration. In fact, this agrees with the finding in [14] where it is found that when the rod is compact and bent the equilibrium configuration is dominated by the bending energy over the twisting energy. In contrast, Table 4.5 and 4.6 demonstrate less of a change in time to reach equilibrium within a relatively large range of shear and stretch modulus values. We see from the tables that neither of the two parameter values plays a critical role in affecting time to reach a new equilibrium. Comparing Table 4.5 and Table 4.6 with Table 4.3 and Table 4.4, we conclude that bending and twist play a major role in affecting time it takes for a rod to reach a new equilibrium configuration. The effect of shear and stretch is negligible in this respect.

Table 4.2: Standard parameter set for rod initialized as a straight rod and given preferred strain twist vector corresponding to a helix

Parameter	Value	Unit
Bending modulus $a_1 = a_2$	3.5×10^{-3}	$dag\mu\text{m}^3\text{s}^{-2}$
Twist modulus a_3	3.5×10^{-3}	$dag\mu\text{m}^3\text{s}^{-2}$
Shear modulus $b_1 = b_2$	8.0×10^{-1}	$dag\mu\text{ms}^{-2}$
Stretch modulus b_3	8.0×10^{-1}	$dag\mu\text{ms}^{-2}$
Strain twist vector $(\kappa_1, \kappa_2, \tau)$	$(1, 0, \frac{\pi}{2})$	μm^{-1}

Table 4.3: Effect of bending modulus on time to reach equilibrium for free rod initialized as straight with preferred helical shape

Bending modulus $a_1 = a_2$ $(10^{-3} dag\mu\text{m}^3\text{s}^{-2})$	1.5	3.5	5.5	9.5	11.5
Time (10^{-7}s)	4597	5406	5684	5912	6246

We then explore the effect of changing different modulus of the rod on its energy profile. We break up the energy into four parts, namely bending energy, twisting energy, shearing energy and stretching

Table 4.4: Effect of twist modulus on time to reach stability for free rod initialized as straight with preferred helical shape

Twist modulus a_3 ($10^{-3} dag\mu \mathrm{m}^3\mathrm{s}^{-2}$)	1.5	3.5	5.5	25.5	27.5	35.5	37.5
Time (10^{-7}s)	8217	5406	4214	1836	1878	2214	2071

Table 4.5: Effect of shear modulus on time to reach stability for free rod initialized as straight with preferred helical shape

Shear modulus $b_1 = b_2$ ($10^{-1} dag\mu \mathrm{m}^3\mathrm{s}^{-2}$)	4	8	12
Time (10^{-7}s)	5398	5406	5410

Table 4.6: Effect of stretch modulus on time to reach stability for free rod initialized as straight with preferred helical shape

Stretch modulus b_3 ($10^{-1} dag\mu \mathrm{m}^3\mathrm{s}^{-2}$)	4	8	12
Time (10^{-7}s)	5414	5406	5403

energy. Total energy of the rod is calculated using Eq. (3.17) by taking the sum of the energy at each immersed boundary point. Each type of energy corresponds to its respective material modulus. Each energy component can be calculated by decomposing the total energy formulation through Eq. (4.4a) - Eq. (4.4d) respectively. Similar to the analysis on time above, we compare the energy profile of the rod with a changed material modulus each time to the energy profile of the rod generated by the standard parameter set. Figure 4.2 (a) shows the energy change of the rod from its initialized state where it is free and straight to its new equilibrium configuration given the strain twist vector and material parameters from the standard parameters from Table 4.2. From Figure 4.2 (a), we see that the total energy, bending energy and twisting energy are all decreasing as time increases. The shearing energy and stretching energy are approximating zero, indicating a negligible effect, similar to its effect on time in our previous analysis. Note that the curve of total enegy, bending energy, and twisting energy all decrease more steeply at the beginning and slow down as time elapses, eventually reaching an equilibrium state as each of them approaches zero.

$$E_{\text{bending}} = \frac{1}{2}\sum_{i=1}^{M-1}\left[a_1\left(\frac{\partial \boldsymbol{D}^2}{\partial s}\cdot \boldsymbol{D}^3 - \kappa_1\right)^2 + a_2\left(\frac{\partial \boldsymbol{D}^3}{\partial s}\cdot \boldsymbol{D}^1 - \kappa_2\right)^2\right]\Delta s \tag{4.4a}$$

$$E_{\text{twist}} = \frac{1}{2}\sum_{i=1}^{M-1} a_3\left(\frac{\partial \boldsymbol{D}^1}{\partial s}\cdot \boldsymbol{D}^2 - \kappa_3\right)^2 \Delta s \tag{4.4b}$$

$$E_{\text{shear}} = \frac{1}{2}\sum_{i=1}^{M-1}\left[b_1\left(\boldsymbol{D}^1\cdot\frac{\partial \boldsymbol{X}}{\partial s}\right)^2 + b_2\left(\boldsymbol{D}^2\cdot\frac{\partial \boldsymbol{X}}{\partial s}\right)^2\right]\Delta s \tag{4.4c}$$

$$E_{\text{stretch}} = \frac{1}{2}\sum_{i=1}^{M-1}\left[b_3\left(\boldsymbol{D}^3\cdot\frac{\partial \boldsymbol{X}}{\partial s} - 1\right)^2\right]\Delta s \tag{4.4d}$$

Figure 4.2 (b) shows the total energy of the rod in different regions of the rod. We partition the rod into three different regions with an equal length of interval. Region 1 corresponds to the first one-third of the rod length close to the bottom; Region 2 corresponds to the second one-third of the rod length, i.e. the region in the middle of the rod; Region 3 corresponds to the last one-third of the rod length, i.e. the region close to the top of the rod. In our simulations, we set the number of immersed boundary points $M = 99$ so that each region contains 33 immersed boundary points. From Figure 4.2 (b), we see that Region 1 and Region 3 have identical energy profile and that the energy of these two regions is lower than the energy of Region 2. The symmetry agrees with the fact that the rod is free with no force applied at either end of the rod. We also notice that the energy of Region 2 is not only higher in value but also has a slightly different decrease pattern from that of Region 1 and Region 3. While the energy curve of Region 1 and Region 3 seems to be concave up, the curve of Region 2 appears to be concave down. Figure 4.2 (c) and Figure 4.2 (d) are the bending energy and twisting energy plots of the three partitioned regions respectively. In Figure 4.2 (c), we see that the symmetry of Region 1 and Region 3 is preserved. However, in contrast to the total energy, the bending energy of the rod in Region 2 first goes through a slight increase and then decreases towards zero. In Figure 4.2 (d), we see an energy profile similar to total energy where Region 1 and Region 3 have a lower energy compared to Region 2.

To explore the contribution of energy from different positions on the rod, we also plot the ratio of the energy at the two free ends of the rod to its total energy. Figure 4.3 (a) and Figure 4.3 (b) show the time-dependent proportion of bending energy and twisting energy at the two endpoints respectively. From Figure 4.3 (a), we see that the proportion of bending energy at the two ends decreases steeply at the beginning and increases slowly after $t = 3 \times 10^{-4}$ s. The maximum proportion reached is 12% for each end, which occurs at time $t = 0$. From Figure 4.3 (b), we can observe that the proportion of twisting energy at the two endpoints is decreasing monotonically and more slowly as it approaches zero. Similar to bending energy, the proportion of twisting energy at each end does not exceed 16%, which indicates that the energy at the two ends does not play a dominant role in the total energy of the rod. As the rod moves away from its initialized state, the proportion of both bending energy and twisting energy at the two ends decreases, implying that the middle region of the rod has a greater and increasing role in the total energy of the rod in the time process to reach an equilibrium state.

To explore the effect of material properties on the energy profile of the rod, we wish to examine the effect of changing different moduli on different energies of the rod. Similar to our previous analysis on time, we change one of the material parameters at a time in each simulation and compare the energy profile obtained with that produced by the standard parameter set in Table 4.2. Figure 4.4 (a) and Figure 4.4 (b) show the different energy profiles generated by implementing different bending modulus. As can be observed from the two figures, as bending modulus increases, bending energy and total energy of the rod both increase. We see in Figure 4.4 (a) that as the value of bending modulus increases, the decrease in bending energy also becomes more drastic and steeper within a given time period. Figure 4.4 (c) and Figure 4.4 (d) are the energy profiles produced by changing twist modulus. The twisting energy and total energy are both increased as twist modulus is increased. It is particularly worth mentioning that in Figure 4.4 (d), a greater twist modulus results in a higher total energy initially and that the energy curve of the rod with a greater twist modulus also has a more rapid decrease and thus less time to reach an equilibrium configuration. This agrees with our results in time to reach equilibrium in 4.4. Figure 4.4 (e) and Figure 4.4 (f) are the shearing energy and stretching energy of the rod corresponding to a changing shear modulus and stretch modulus. The numerical value of the energy curves in these two graphs indicate that shear modulus and stretch modulus play a relatively minor role in both time to reach an equilibrium and total energy of the rod. This implies that shear energy and stretch energy are a lower order of magnitude relative to other moduli for this test case.

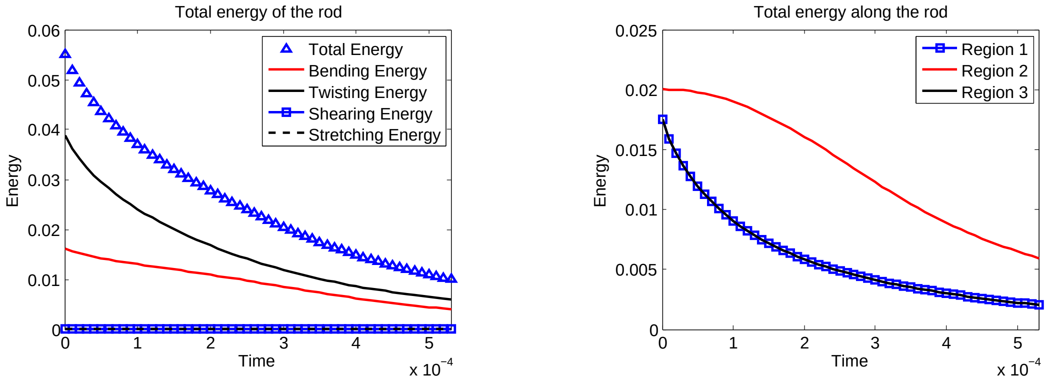

(a) Total energy of the rod (b) Total energy of the rod

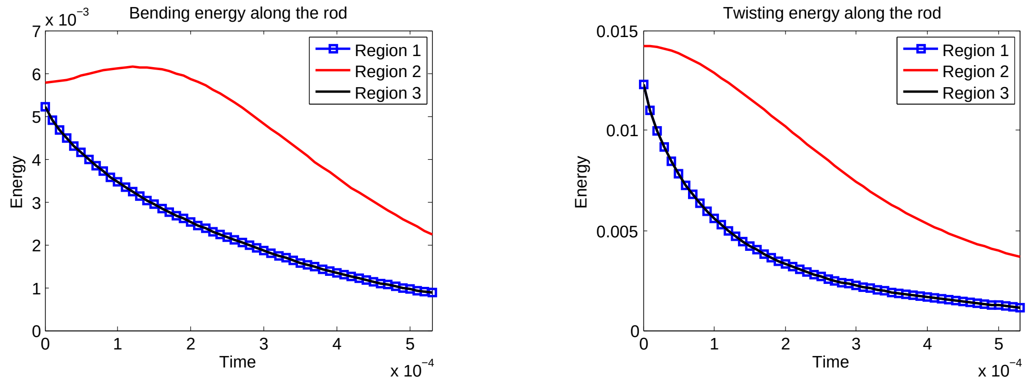

(c) Bending energy along the rod (d) Twist energy along the rod

Figure 4.2: Region 1-3 are partitions of the rod from bottom to top. In this case, the rod is initialized as a free straight rod and prescribed with a helical configuration. Note that in (b)-(d), the energy curve of Region 1 and Region 3 overlap.

4.2 Helical Equilibria

4.2.1 Rod Initialized as Straight and Tethered

Section 4.1 showcases an example of helical equilibrium where given a set of preferred curvature and twist, a free rod achieves a preferred helical configuration when energy is minimized. One of the interesting questions in helices is whether a helix is a stable configuration. Lim studied the stability of this configuration by keeping the rod straight and inputting a varying intrinsic twist [14]. The numerical results computed using a sequence of increasing intrinsic twist shows that there exists a critical twist τ_c above which a twisted straight rod becomes unstable and demonstrates buckling. Lim shows that buckling behavior can occur at many different locations on the rod, depending on the given twist and length of the rod. In Lim's study in [14], buckling is observed in the middle of the rod because there is no force or moment at either end of the rod. Inspired by this result, we wish to look at the behavior of a straight and tethered rod, i.e. a rod with applied force at one end. Under the loaded condition, we still prescribe the rod with both non-zero curvature and non-zero twist, as opposed to the free and straight rod with zero curvature studied in [14]. We are interested in the effect of adding a force to one

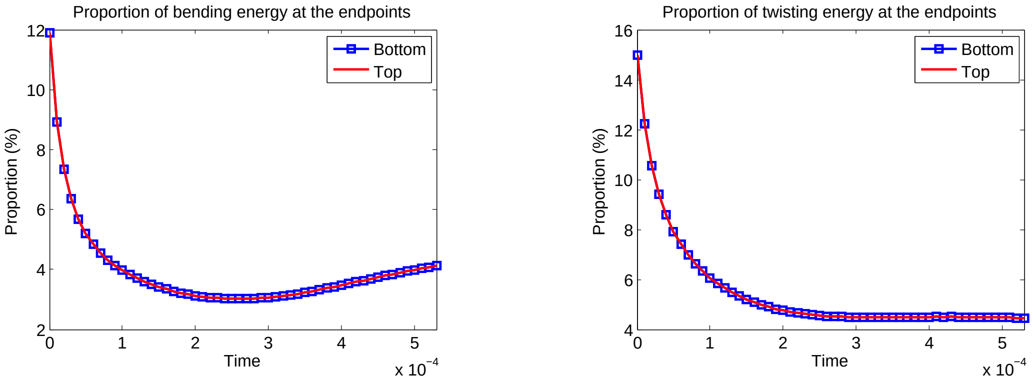

(a)

(b)

Figure 4.3: In this case, the rod is initialized as a free straight rod prescribed with a helical configuration. (a) Proportion of the bending energy at the two ends with respect to the total bending energy of the rod (b) Proportion of the twisting energy at the two ends with respect to the total twisting energy of the rod.

end of the rod on the buckling position and stability of the rod.

We tether the rod by applying an additional force to the bottom of the rod. We envision the bottom of the rod is tethered by a linear elastic spring. This Hookean type force keeps the first immersed boundary point of the rod, i.e. the bottom of the rod at its initialized position. If the bottom of the rod tends to move away from its initialized position, this tether force pulls the rod in an opposite direction so that it stays at its original location. For simplicity, we let the first point on the rod be initialized at the origin. We add a spring force to the first immersed boundary point of the rod. This force is additional to the internal force $\boldsymbol{F}$ at the first point described by Eq. (3.4) in Section 3.1 and functions to prevent the first point from moving away from the origin. Fauci et al. used a spring force between a pair of immersed boundary points given by Eq. (4.5) in [8] where S is the stiffness coefficient, $\boldsymbol{X}_i$ and $\boldsymbol{X}_j$ are the two immersed boundary points and d_i is resting length between them. We employ the same force function. In our case, $\boldsymbol{X}_j$ is the origin and the bottom point $\boldsymbol{X}_1$ is $\boldsymbol{X}_j$. $\boldsymbol{X}_1$ is located at the origin when the rod is in a resting state, yielding d_i=0. Hence, the total force at the first point of the rod is now given by Eq. (4.6) where $\boldsymbol{F}_1^*$ is the new force, S is the stiffness coefficient (spring constant with a unit of $\frac{m^*}{L^*}$ where m^* and L^* are the characteristic mass and length), $\boldsymbol{X}_1$ is the position of the first point and $\boldsymbol{F}_1$ is the internal force at $\boldsymbol{X}_1$.

$$\boldsymbol{f}(\boldsymbol{X}_i) = S\left(1 - \frac{d_i}{\|\boldsymbol{X}_i - \boldsymbol{X}_j\|}\right)(\boldsymbol{X}_i - \boldsymbol{X}_j) \tag{4.5}$$

$$\boldsymbol{F}_1^* = S(-\boldsymbol{X}_1) + \boldsymbol{F}_1 \tag{4.6}$$

To explore the stability of obtained helical equilibria, we run simulations for three cases, each with a different preferred intrinsic twist vector. The three cases and parameters can be found in Table **??**. To obtain better knowledge about the configuration of our prescribed helix, we set the preferred intrinsic twist and curvature by setting r, the radius of the helix and h, the axial distance of one turn of the helix. The corresponding twist and curvature of the helix can be calculated via Eq. (4.7) and Eq.

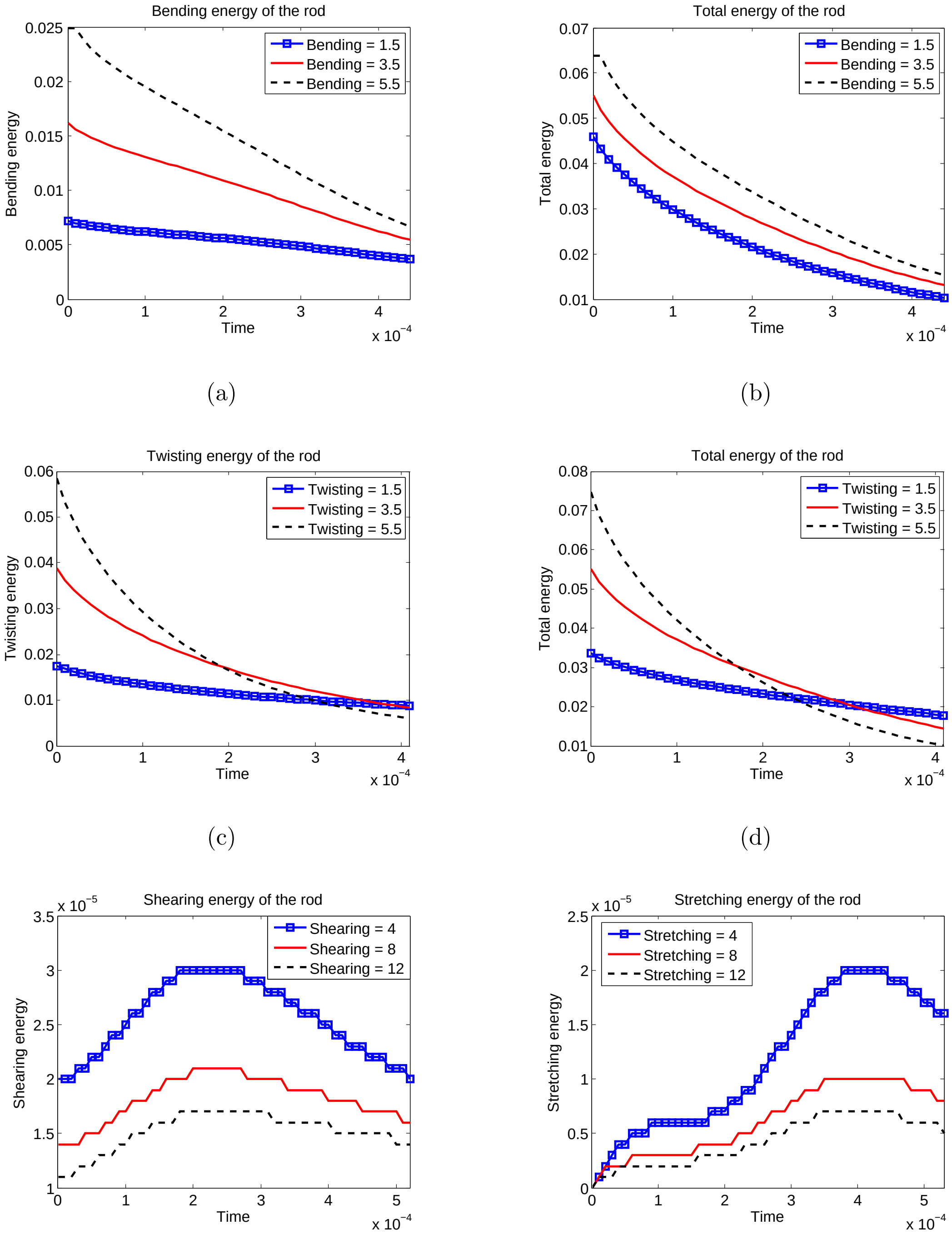

(a) (b)

(c) (d)

(e) (f)

Figure 4.4: (a) Bending energy (b) Total energy (c) Twist energy (d) Total energy (e) Shear energy (f) Stretch energy of the rod with different bending modulus.

(4.8). For curvature, we set $\kappa_1 = \kappa$ and $\kappa_2 = 0$. Table 4.7 shows the set of parameter values used in our computation. Note that the number of turns of a helix with a given length can be computed by Eq. (4.9) where κ_3 is the twist and L is length of the rod. The expected number of turns of a helix q can be computed by Eq. (4.9). Comparing the expected number of turns provides us insights into why the instability develops as the helix we prescribe becomes increasingly twisted.

$$\kappa = \frac{4\pi^2 r}{4\pi^2 r^2 + h^2} \tag{4.7}$$

$$\kappa_3 = \frac{2\pi h}{4\pi^2 r^2 + h^2} \tag{4.8}$$

$$q = \frac{\kappa_3 L}{2\pi} \tag{4.9}$$

Figure 4.5 (a) is the preferred target helix in Case 1. Figure 4.5 (b) - (d) show results for three cases. Figure 4.5 (b) shows that the rod achieves a stable helical configuration evolved from a straight, tethered rod. This corresponds to the parameter set Case 1 in Table 4.7. Figure 4.6 (a) shows the time evolution of total energy of the rod, which is decreasing as the rod deforms into its prescribed structure. We see that the energy curve shares the same concavity with that observed in Figure 4.2 (a), i.e the energy curve of a free, straight rod with a prescribed intrinsic twist. In both figures, energy of the rod decreases rapidly once the rod starts evolving towards its prescribed configuration; as the energy approaches zero, the rate of change also decreases, eventually reaching a plateau. Figure 4.5 (c) shows the simulation result of Case 2. We see that the rod tries to achieve its prescribed helical configuration but fails to do so due to the increased preferred twist. As can be seen, the rod at equilibrium is almost helical except for the buckling close to the bottom of the rod. Figure 4.6 (b) shows the time evolution of the energy profile of the rod in Case 2. Similar to Figure 4.6 (a), the total energy of the rod is decreasing and is minimized when the rod achieves its final configuration. In constrast to Case 1, the energy of the rod in Case 2 is somewhat concave down initially. Energy decreases more slowly at the beginning and more rapidly near $t = 0.005$s. This may be explained by the fact that the rod attempts to achieve its prescribed curvature and twist, but immediately experiences difficulty under the contraints of its own material properties. Due to its own material property, the rod is unable to minimize its energy further once it reaches a threshold, so it maintains a steady energy value around that threshold from $t = 0.005$s onward. Notice that the final energy of the rod is higher than that of Case 1 up to one order of magnitude, implying that it is a more unstable helical equilibrium compared to Case 1. Figure 4.5 (d) shows the simulation result of Case 3 in which we give the rod a much shorter preferred helical radius and axial distance, as can be seen from Table 4.7. A decreased amplitude r leads to an increased twist, followed from Eq. (4.8). With a larger preferred twist, we see that the rod immediately demonstrates a greater instability, showing more complicated geometry like loops or what is called plectonemes in [14]. Figure 4.6 (c) shows the energy profile of the rod in Case 3. We notice that the rod starts off with an energy that is one order of magnitude higher than the rod in Case 1 and Case 2. The total energy of the rod decreases rapidly as the rod starts to deform towards its prescribed configuration, reaching and leveling off at approximately 0.15 fJ in 0.002s. Compared to Case 2, it takes less time for the rod to reach a steady energy level and the final energy level of the rod is one order of magnitude greater, corresponding to a greater instability of its helical equilibrium. The buckling and loops we obtain in our simulations agree well with the instability studied in [14], except for the position of the buckling and loop observed in [14]. In Lim's simulation, buckling occurs at the middle of the rod; loops also occur in such a way that the rod shows some form of symmetry. In our simulations, in the presence of force at one end, buckling and loops occur closer to the tethered end to balance force and moment.

Table 4.7: Parameter values for tethered rod initialized as straight

Parameter	Value
Number of IB points M	150
Distance between IB points Δs (μm)	0.1
Time step Δt (s)	1×10^{-7}
Fluid viscosity μ ($g\mu\text{m}^{-1}\text{s}^{-1}$)	8.9×10^{-7}
Stiffness coefficient S ($g\mu\text{m s}^{-2}$)	50
Prescribed (Radius, Axial Distance) (r, h) (μm)	Case 1: (0.5,5)
	Case 2: (0.5, 2.5)
	Case 3: (0.05, 1)
Expected number of turns q	Case 1: 2.1509
	Case 2: 2.3264
	Case 3: 13.6525
Twist κ_3	Case 1: 0.9010
	Case 2: 0.9745
	Case 3: 5.7188

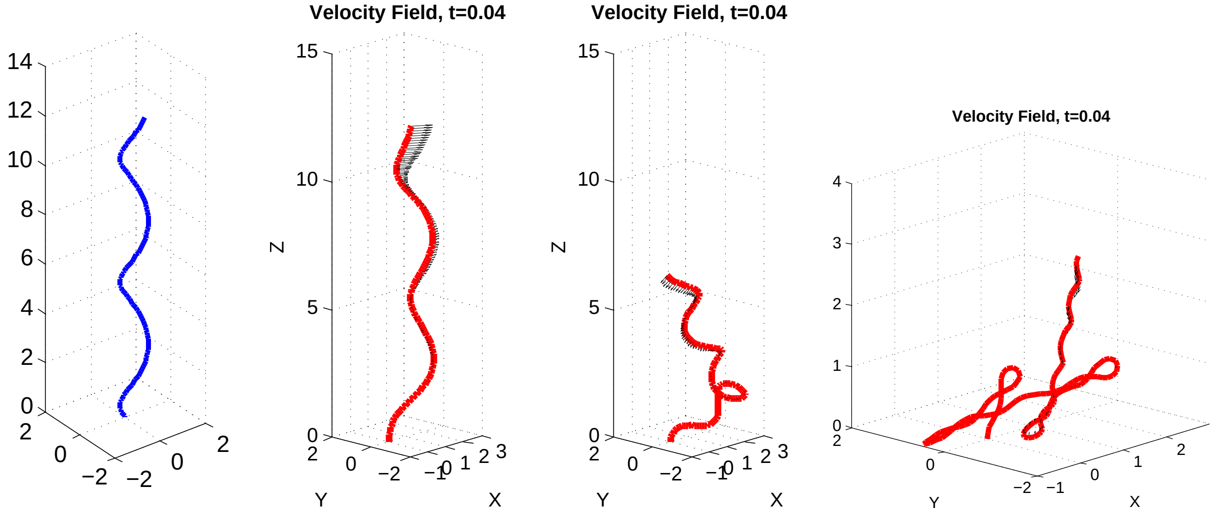

(a) Preferred helix (b) Case 1: Stable (c) Case 2: Buckling (d) Case 3: Loop

Figure 4.5: The rod is initialized as a tethered straight rod prescribed with a helical configuration. The parameter values used for Case 1 - Case 3 can be found in Table 4.7. Arrows refer to the velocity field of the rod at immersed boundary points.

4.2.2 Rod Initialized as Helical and Tethered

Besides the behavior of the rod initialized as a straight rod, we are also interested in the helical equilibria of a rod initialized as a helix. To explore the behavior of a tethered helical rod, we first initialize the rod as a circular helix and then prescribe the rod with a different helical radius and axial distance. We then analyze the different energy change of the rod associated with each type of instability. Similar to the above simulations for a straight, tethered rod, we run three cases for this test, each with a different preferred helical configuration. In each case, we initialize the rod as a tethered

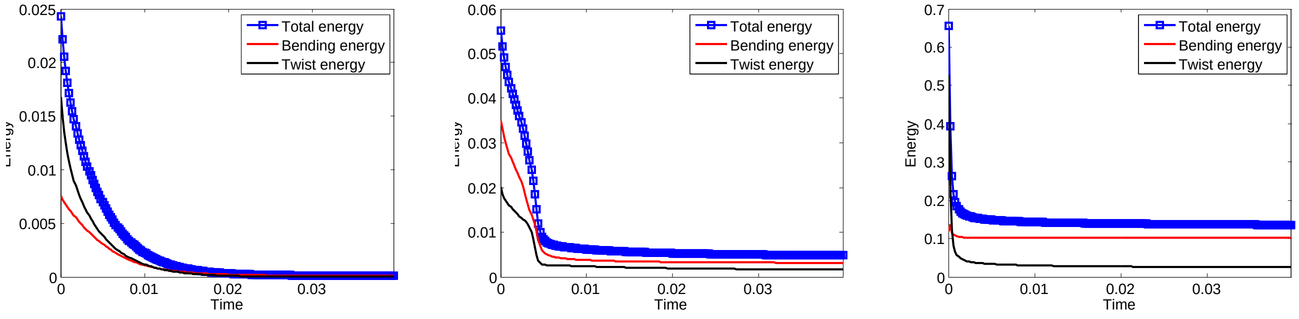

(a) Case 1: Stable

(b) Case 2: Buckling

(c) Case 3: Loop

Figure 4.6: Energy profile of helical equilibria achieved from a tethered straight rod in Case 1 through Case 3. Parameter values for each case can be found in Table 4.7.

helical rod with $r = 0.5$ (μm) and $h = 2.5$ (μm). When we initialize the rod as a helix, we also initialize the orthonormal triad by computing the tangent vector of the helix using the forward finite difference so that the $\boldsymbol{D}^3$ vector is aligned with the tangent vector of the rod at each point. In each case, we prescribe this helical configuration with an unchanged curvature and a changed twist. Given a preferred curvature and twist, we can compute the corresponding radius r and axial distance h by Eq. (4.2) and Eq. (4.3) respectively. Table 4.8 shows the helix parameters implemented in the three cases of our simulations; we distinguish between the helix parameter sets used in different cases by calling them Case 4, Case 5 and Case 6. Note that we construct the initial helix using a discretized version of Eq. (2.29) - Eq. (2.31) presented earlier [3]. The discretized helix construction is given by Eq. (4.10) where k denotes the k-th immersed boundary point of the rod and $x_k(s)$, $y_k(s)$ and $z_k(s)$ represent the x, y and z coordinate of the k-th point repectively. In Eq. (4.10), we set the number of immersed boundary points to be $M = 150$. Note that we set $\Delta s = 0.1$ which does not equal the length of the segment between each consecutive pair of immersed boundary points. Due to the nonzero curvature and twist, the total arclength of the rod is calculated to be $L = 14.8907$, which is close to but not exactly 15 as in Case 1 through Case 3. We would like to emphasize that this initial helix has a different curvature and twist from what it is prescribed with.

$$x_k(s) = -\, r\sin\left(\frac{2\pi k\Delta s}{S}\right) \tag{4.10a}$$

$$y_k(s) = r - r\cos\left(\frac{2\pi k\Delta s}{S}\right) \tag{4.10b}$$

$$z_k(s) = \frac{hk\Delta s}{S}. \tag{4.10c}$$

Figure 4.8 (a) - (d) show the simulation results of all our cases. Figure 4.8 (a) is our initialized helical configuration. Figure 4.8 (b) shows the final configuration the rod achieves in Case 4. Comparing with the initialized helical configuration, we see that the helical rod is eventually able to deform into the prescribed helix with a higher twist and more turns. The initial rod configuration has four full turns. However, we observe 4.5 turns after a new equilibria is achieved. Figure 4.9 (a) shows the energy profile of the rod in Case 4. As we can observe from the plot, in the initial time period, the bending energy of the rod increases temporarily as the rod tries to deform into a structure with a higher twist. The total energy and twist energy decreases throughout the deformation process. Notice that the radius of the prescribed helix in Case 4 is smaller than that of the initial helix, which corresponds to a greater curvature and therefore a greater bending energy. The increase in bending energy can be interpreted as a short adaptation of the rod to a more twisted helical structure. We can see from the figure that despite the slight increase at the beginning, the bending energy starts decreasing at $t = 2 \times 10^{-3}$ s and eventually decreases to approach zero as the rod achieves its prescribed configuration.

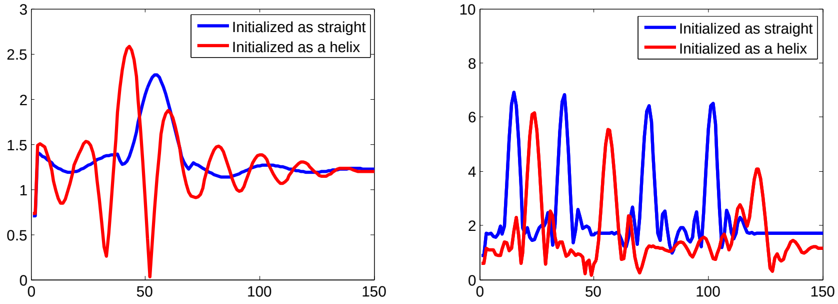

(a) Buckling: curvature along the rod (b) Loop: curvature along the rod

Figure 4.7: Curvature along the length of the rod for the buckling case and looping case. Buckling is Case 2 and Case 5 where we initialize the rod as straight and a helix respectiely. Loop is Case 3 and Case 6 where we initialize the rod as straight and helix respectively.

Figure 4.8 (c) shows the simulation result of Case 5, in which we set the preferred twist $\kappa_3 = \pi$. As a result of this increased twist, instead of achieving its prescribed helix, the rod shows buckling closer to the bottom of the rod compared to Case 2. Figure 4.7 (a) shows the position dependent curvature along the length of the rod. We calculate the curvature of the rod by computing the norm of the tangent vector based on Frenet's formula. We see that Case 5 in which we initialize the rod as a helix shows more fluctuations of curvature along the length of the rod. The greatest peak seen in the plot corresponds to the buckling observed. We see that in Case 5, buckling occurs closer to the bottom of the rod with a greater curvature. Figure 4.9 (b) shows the energy profile of the rod in this case. Notice that given a greater preferred twist, the rod also starts off with a higher energy value. The total energy of the rod in Case 5 has an initial energy that is one order of magnitude higher than that in Case 4. In Figure 4.9 (b), the twisting energy and total energy decrease monotonically throughout the process. The twisting energy and bending energy change remarkably at the beginning of the transformation, showing that the rod immediately tends to deform itself towards the prescribed curvature and twist. However, subject to the constraints of its own bending modulus and twist modulus, once the rod is unable to achieve its prescribed configuration, the bending energy and twisting energy both slow down its rate of decrease and eventually level off at a certain value. This explains the plateau we observe from $t = 2 \times 10^{-3}$ s onward in Figure 4.9 (b). Compared to Case 4, we see a higher energy at equilibrium in the case of buckling. Figure 4.8 (d) shows the simulation result of Case 6 in which we set $\kappa_3 = 2\pi$. This higher twist results in a greater instability of the helical equilibrium with loops and knots as we have seen in previous simulations. Figure 4.7 (b) shows the curvature long the rod for Case 3 and Case 6. Case 3 has four major loops and Case 6 has three major loops. Figure 4.9 (c) is the energy profile of the rod in this case. Compared to Case 5, the bending energy of the rod goes through a much smaller increase at the initial time period; the bending energy and twisting energy also reach a constant, however, much higher level more quickly. This may be explained by the fact that the gap between the prescribed configuration and the ability of the rod to deform is so large that the rod immediately reaches its limit to bend and twist and therefore stays at a steady energy level.

Table 4.8: Helix parameters for rod initialized as a tethered helix

Parameter	Value
Initialized (Radius, Axial Distance) (r, h)	(0.5,2.5)
Intrinsic twist vector of initialized helix $(\kappa_1, \kappa_2, \kappa_3)$	(1.22,0,0.97)
Prescribed intrinsic twist vector $(\kappa_1^*, \kappa_2^*, \kappa_3^*)$	Case 4: $(1.22, 0, \frac{\pi}{2})$
	Case 5: $(1.22,0,\pi)$
	Case 6: $(1.22,0,2\pi)$
Prescribed (Radius, Axial Distance) (r, h)	Case 4: (0.38,2.50)
	Case 5: (0.73,1.74)
	Case 6: (0.04,0.96)

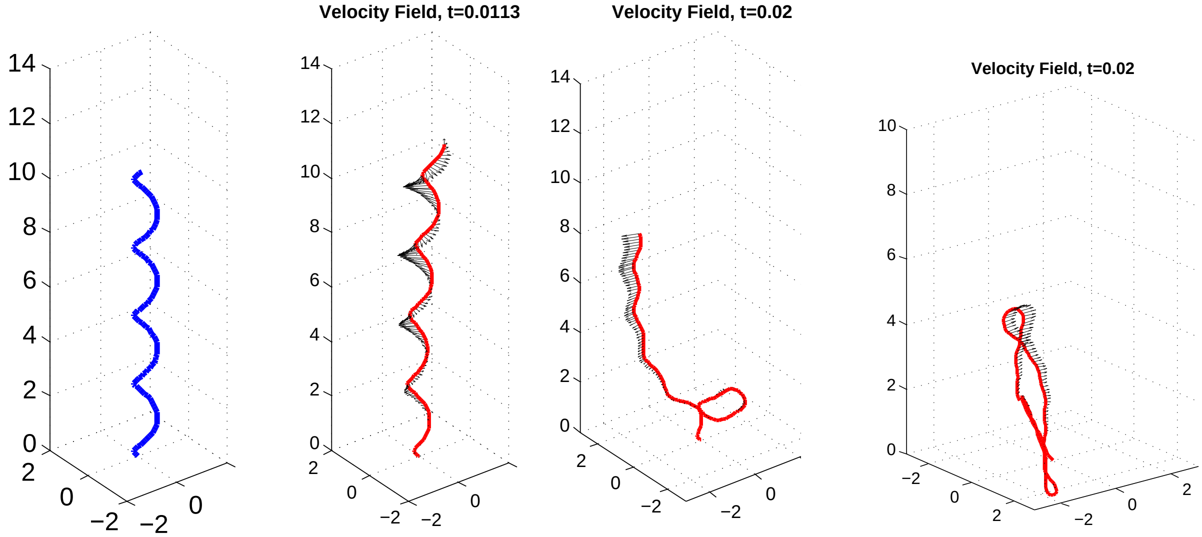

(a) Initial helix (b) Case 4: Stable (c) Case 5: Buckling (d) Case 6: Loop

Figure 4.8: Helical equilibria from a rod initialized as a tethered helix. The parameter values for Case 4 through Case 6 can be found in Table 4.8. Note that from (b) to (d), we increase the prescribed twist of the rod, which gives rise to instability.

Lim discussed the relation between prescribed intrinsic twist and instability of helical equilibria in detail in [14]. Inspired by this study, we wish to explore whether the length of the rod and the prescribed curvature of the rod has any effect on the instability of helical equilibria achieved. First, we test the effect of rod length on instability. We run simulations for a straight, tethered rod with a longer rod length. We prescribe the rod the same configuration as we did previously in Case 1 to Case 3. In this simulation, we employ the same immersed boundary points spacing Δs and change the number of

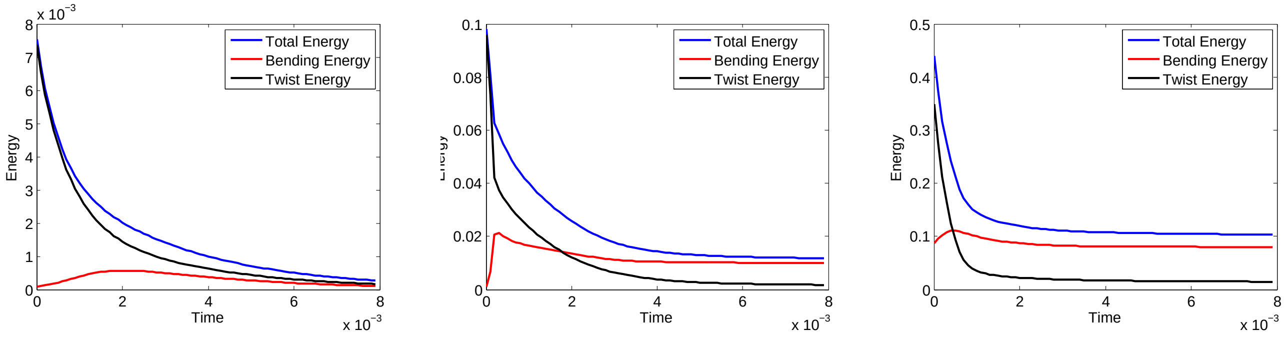

(a) Case 4: Stable

(b) Case 5: Buckling

(c) Case 6: Loop

Figure 4.9: Energy profile of helical equilibria achieved from a rod initialized as a tethered helix. The parameter values are found in Table 4.8.

immersed boundary points M from 150 to 250. Figure 4.10 (a) - (c) show the results of the simulation implemented with the configuration prescribed in Case 1, Case 2 and Case 3 respectively. In Figure 4.10 (a), we obtain a stable helical equilibrium as we did in Case 1. In Figure 4.10 (b), we still observe buckling like in Case 2. This can also be observed from Figure 4.11 (a) which indicates that buckling occurs at around the 100th immersed boudary point, which is approximately $\frac{2}{5}$ of the length of the rod. In Figure 4.10 (c), we observe loops again. Figure 4.11 (b) shows the curvature along the rod in this case. We observe five major loops. Compared to the loop in Figure 4.5 (d), the loops of a longer rod look more twisted and dense. The geometry also becomes more complicated.

To explore the effect of curvature alone on instability, we also run simulations for a straight, tethered rod prescribed with a zero twist and a sequence of nonzero, increasing curvature. We implement the standard parameter set and prescribe the rod with an intrinsic twist vector of $(\kappa_1, \kappa_2, \kappa_3) = (\kappa, 0, 0)$ where we vary κ in each simulation. Figure 4.12 (a) - (d) shows the simulation result for $(\kappa_1, \kappa_2, \kappa_3)$ where $\kappa_1 = 5$, $\kappa_1 = 10$, $\kappa_1 = 15$, $\kappa_1 = 30$ and $\kappa_1 = 45$ respectively. The prescribed configuration has twist $\kappa_3 = 0$ and therefore is a circle with radius 1. Comparing Figure 4.12 (a) - (d), we see that the configuration achieved by the rod at equilibrium becomes increasingly curled. We observe in Figure 4.12 (c) - (d), the rod has points of self-contact. Adding a repulsive force as a function of distance among each pair of immersed boundary points might prevent this from happening, which will be discussed in Chapter 5. Figure 4.13 (a) - (d) shows the energy curve of the rod associated with each case. Despite the occurence of self-contact, we notice that as we increase the curvature by κ_1, the total energy of the rod increases remarkably. The energy of the rod at equilibrium in three cases differs by up to one order of magnitude. The increase in energy corresponds to an increasing instability associated with each helical equilibrium achieved, which has been previously observed in [14] as well in the study of instability of a free straight rod with nonzero twist. The energy results in [14] indicate that a greater intrinsic twist is associated with a greater instability and a higher total energy. Our simulation results indicate that increasing curvature alone also contributes the instability of helical equilibria achieved by a straight, tethered rod.

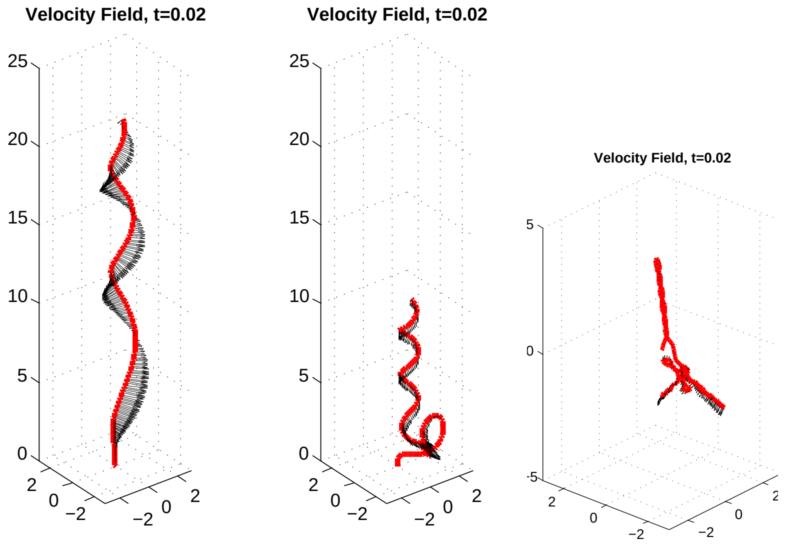

(a) (b) (c)

Figure 4.10: Helical equilibria of a rod initialized as tethered straight rod with prescribed helical parameters same as Case 1, Case 2 and Case 3 respectively. Parameter values can be found in Table 4.7. Note that in this case, we increase the length of the rod by increasing the number of immersed boundary points from $M = 150$ to $M = 250$ compared to Case 1 through Case 3 shown previously.

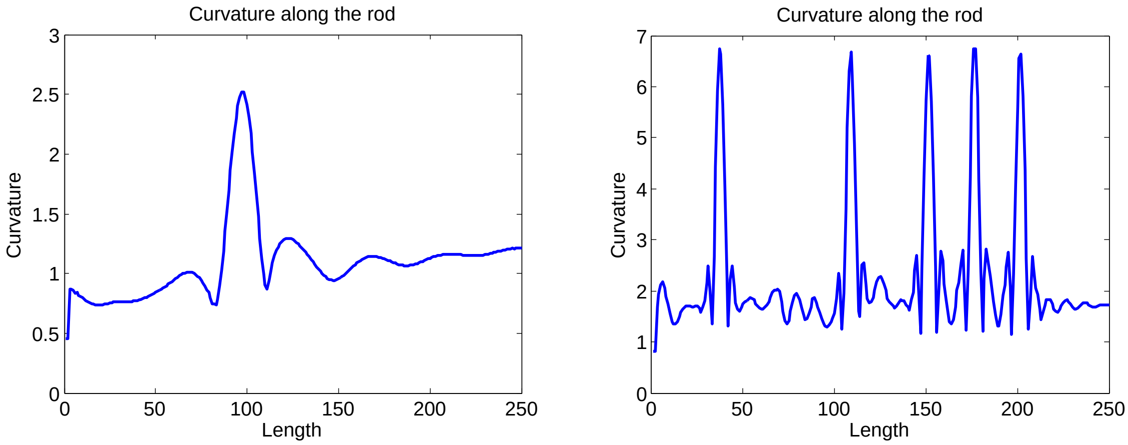

(a) (b)

Figure 4.11: Curvature along the length of the rod in the case of buckling and looping. In this case, we increase $M = 150$ to $M = 250$. Increased rod length for Case 2 in (a), Case 3 in (b).

4.3 Helical Bending Wave

4.3.1 Helical Wave Propagating on a Free Rod

We study the behavior of the rod propagating a helical bending wave along its length. The helical bending wave is distinct from a rigid rotation of a helix. The rod is prescribed with a time dependent

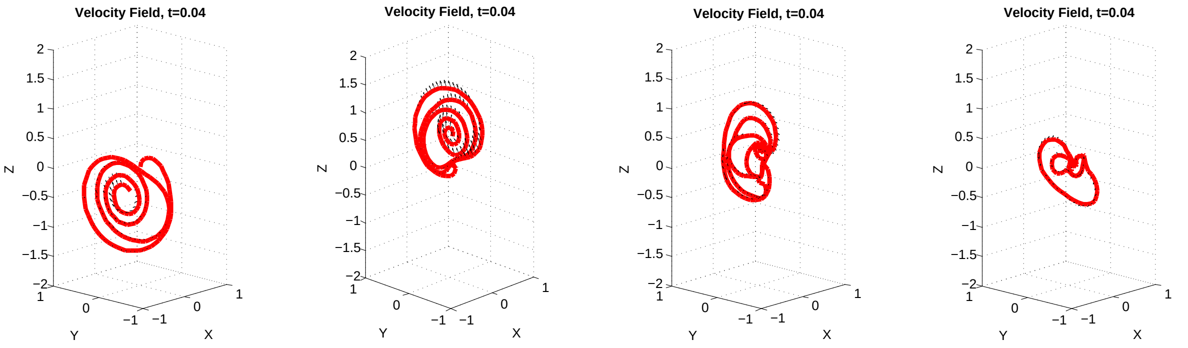

(a) $\kappa_1 = 5$ (b) $\kappa_1 = 15$ (c) $\kappa_1 = 30$ (d) $\kappa_1 = 45$

Figure 4.12: In each case, the rod is initialized as a straight and free rod and prescribed with a zero twist and nonzero curvature. The black arrows are the velocity vectors at each immersed boundary point. Parameters used can be found in Table 4.2.

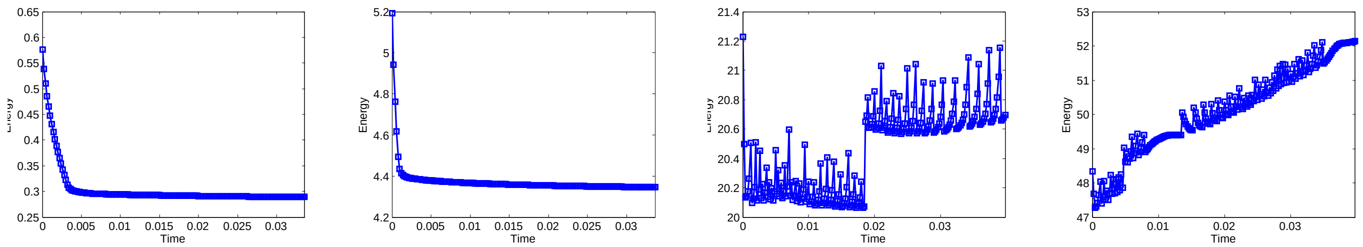

(a) $\kappa_1 = 5$ (b) $\kappa_1 = 15$ (c) $\kappa_1 = 30$ (d) $\kappa_1 = 45$

Figure 4.13: The energy profile of the rod prescribed with zero twist and nonzero curvature in each case described in Figure 4.12.

curvature with zero twist and each point on the helix is bending. We prescribe the rod with a time-dependent intrinsic twist vector $\mathbf{\Omega}(s,t)$ for a helical bending wave given by Eq. (4.11). Note that τ is the torsion $(\frac{1}{L^*})$, σ is the frequency of the propagating helical wave with a unit of $\frac{L^*}{t^*}$ where L^* is the characteristic length and t^* is the characteristic time; Ω_1 and Ω_2 together determine the curvature of the rod κ by Eq. (4.12).

$$\mathbf{\Omega}(s,t) = \{\Omega_1, \Omega_2, \Omega_3\} = \{\kappa_1 \cos(\tau(s+\sigma t)), -\kappa_2 \sin(\tau(s+\sigma t)), 0\} \tag{4.11}$$

$$\kappa = \sqrt{\Omega_1^2 + \Omega_2^2} \tag{4.12}$$

In the prescribed intrinsic twist vector, we set the twist to be zero by setting the third component $\Omega_3 = 0$. As is mentioned previously in Section 2.2, in the context of non-rigid rotation, torsion does not equal twist. As a result of the non-zero torsion, the rod will be rotating in the x-y plane. The frequency of the traveling wave is described by σ where a higher σ corresponds to a faster traveling wave, not considering the restraints of the material properties of the rod. In the following discussion, we also present simulation results showing that subject to the constraints of the stiffness of the rod, a higher σ does not necessarily lead to a faster propagation of the wave on the rod. Note that the sign of σt in both the first and second component of $\mathbf{\Omega}(s,t)$ determine the direction of the swimming rod.

The helical waveform can also be represented by r and p where r is amplitude, p is pitch and h is the handedness. h can be either 1 or -1. We choose $h = 1$ for simplicity. Note that $h = 2\pi p$ is the wavelength of the helical wave and also referred to as the axial distance of one turn of the helix first mentioned in Eq. (2.27). Depending on the material moduli and prescribed helical waveform, the helical bending wave might be propagating at different speeds along the length of the rod. In this project, we explore the behavior of the rod propagating a helical bending wave in both free and tethered conditions. First, we present results for the case of a free rod. We first show the effect of σ on the speed at which the rod propagates the helical bending wave with a given set of material moduli. Details of the parameters used can be found in Table 4.9 where the standard parameter set is regarded as a reference parameter set for us to compare all our simulations with. In each simulation we present in this section, one or two parameters will be varied based on the standard parameter set; we compare each simulation result with that obtained by the standard parameter set. Figure 4.14 shows the result of our Simulation 1 where we use all the parameter values from the standard parameter set. We prescribe the rod with a helical bending wave with $r = 1$ and $p = 3$, based on which, the corresponding curvature κ_1, κ_2 and torsion τ can be calculated through Eq. (4.13a) and Eq. (4.13b) which are equivalent to Eq. (4.7) and Eq. (4.8). Note that if we set $\kappa_1 = \kappa_2$, then $\kappa_1 = \kappa_2 = \kappa$ which can be derived from Eq. (4.12).

$$\kappa = \frac{r}{p^2 + r^2} \tag{4.13a}$$

$$\tau = h \cdot \frac{p}{p^2 + r^2} \tag{4.13b}$$

In this simulation, we set $\kappa_1 = \kappa_2$ and set the frequency of the traveling wave to be $\sigma = 2 \times 10^4$ μms^{-1}.

Table 4.9: Free straight rod propagating a helical bending wave

Parameter	Standard
Number of IB points M	100
Fluid viscosity μ ($dag\mu\text{m}^{-1}\text{s}^{-1}$)	8.9×10^{-7}
Bending modulus $a_1 = a_2$ ($dag\mu\text{m}^3\text{s}^{-2}$)	3.5×10^{-3}
Twist modulus a_3 ($dag\mu\text{m}^3\text{s}^{-2}$)	3.5×10^{-3}
Shear modulus $b_1 = b_2$ ($dag\mu\text{ms}^{-2}$)	8.0×10^{-1}
Stretch modulus b_3 ($dag\mu\text{ms}^{-2}$)	8.0×10^{-1}
Prescribed (r, p) (μm)	(1,3)
Prescribed (κ, τ) (μm)	(0.1,0.3)
Frequency σ (μms^{-1})	2×10^4

We see from Figure 4.14 (a) that while the rod is propagating a helical bending wave, it generates primarily self-rotation in the x-y plane with slow movement along the positive z-axis, which can be seen from Figure 4.14 (d) which we will discuss shortly. Figure 4.14 (b) shows the wave that is propagating along the length of the rod at different time points. The angular frequency of oscillation at each point of the rod is $\tau\sigma$; therefore the period of oscillation at each point can be calculated by $T = \dfrac{2\pi}{\tau\sigma}$. In this simulation, the period of oscillation is calculated to be 0.001 s. In Figure 4.14 (b), we plot the x-coordinate vs. the z-coordinate of the immersed boundary points on the rod at different times within one period of the rod motion. We notice that the waveforms observed at $t = 0.0002$ s and $t = 0.001$ s look somewhat symmetric about the z-axis and both have a smaller amplitude compared to the waveform observed at $t = 0.0006$ s. This agrees with the physical phenomenon that it takes time for a straight rod to start propagating a helical wave and that at the end of a period, the rod tends to return to its initial state. We also notice that the maximum amplitude that the rod achieves is approximately 0.04, which occurs around a half of the period. As the prescribed intrinsic twist vector $\mathbf{\Omega}$ is a function of both time t and arclength s, the oscillation at different points along the length of the rod have different phases.

Figure 4.14 (c) shows the motion of the x-coordinate of different chosen points on the rod. $k = 1$ refers to the first point at the bottom of the rod, which is initialized at the origin; $k = 50$ refers to the 50^{th} point counting from the bottom, which is also the mid-point of the rod; $k = 100$ refers to the 100^{th} point on the rod. We see from this figure that the top and bottom of the rod are oscillating at approximately the same amplitude 0.04 and at a remarkably higher amplitude than that of the mid-point. We note that this observation corresponds to the energy distribution along the length of the rod seen earlier in Figure 4.2 (c) from Section 4.1 where the middle region of a free rod with a prescribed intrinsic twist plays a dominant role in the total bending energy of the rod. Due to the fact that a higher bending energy is stored within the middle region of the rod, this bending energy restrains the rod from releasing it and thus from generating movements. We also note that we prescribe the rod with a curvature $\kappa = 0.1$, which is the amplitude of the sinusoidal oscillation that the rod is expected to achieve. The difference between the achieved amplitude 0.04 and the prescribed amplitude 0.1 suggests that the rod is unable to achieve its prescribed configuration subject to its own material moduli. Figure 4.14 (d) shows the motion of the z-coordinate of the first and second points of the rod. Although we see that z-coordinate of each of the two points increase slowly and slightly as time elapses, the increment indicates that the rod is moving in the direction of positive z-axis. The average swimming speed can be calculated by the increment of z-coordinate at each point and the time elapsed. We calculate the swimming speed based on the displacement of the first point of the rod. The result of this calculation is shown in Table 4.10. Lastly, Figure 4.14 (e) shows the energy profile of the rod in this case. The twist energy is zero, corresponding to the zero twist we prescribe the rod. We see that the energy oscillates in the intial time period. As time evolves, the amplitude of oscillation decays. At time $t = 0.01$ s, the energy curve reaches a nearly constant level. Notice that the energy oscillates around 1×10^{-4} fJ, a relatively low value, throughout the time process. This indicates that the rod is staying in a relatively stable state.

To explore the effect of changing σ on the behavior of the rod propagating a helical bending wave, we increase the value of $\sigma = 2 \times 10^4$ in Simulation 1 to $\sigma = 5 \times 10^4$ in Simulation 2 while keeping the rest of the parameters unchanged from Simulation 1. The parameter values can be found in Table 4.9. Figure 4.15 (a) shows the wave that is propagating along the rod at different time points. The calculated period for Simulation 2 can be found in Table 4.10. The increased σ, i.e. a higher frequency of the traveling wave results in a shorter period of oscillation at each point. In Figure 4.15 (a), the waveforms at $t = 0.0002$ s and $t = 0.0004$ s look somewhat symmetric with respect to the z-axis, showing that the rod is oscillating about the z-axis periodically. Figure 4.15 (b) shows the time evolution of the oscillating trajectory of the x-coordinate of three different chosen immersed boundary points, namely the first point, the mid-point and the last point on the rod. We will use the same color scheme for the rest of the simulations as Simulation 1 where the blue line represents the bottom point, the red line represents the mid-point and the black dashed line represents the top point. We observe that in this simulation, each chosen point oscillates with a time-dependent amplitude which also undergoes a

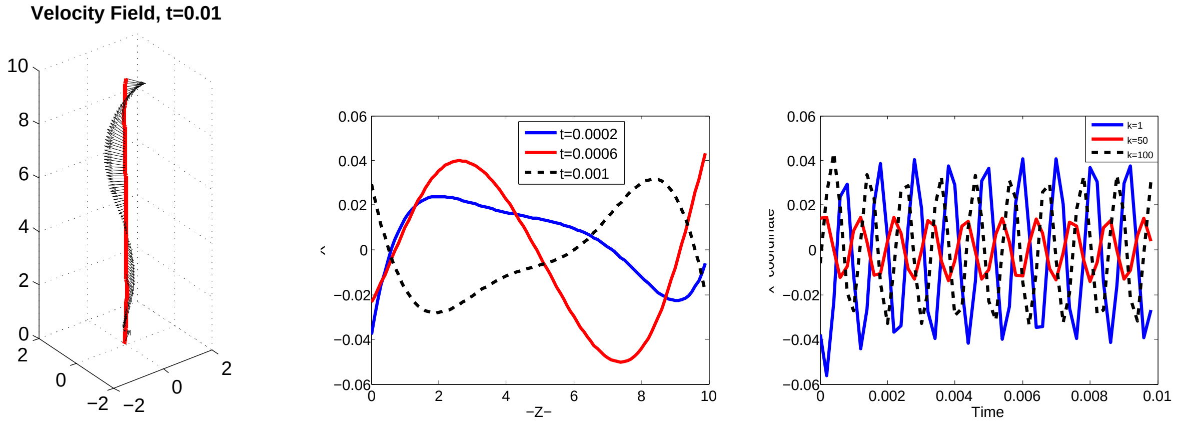

(a) Free rod with a helical wave

(b) Waveform of the rod

(c) Wave of x-coordinate at different positions along the length of the rod

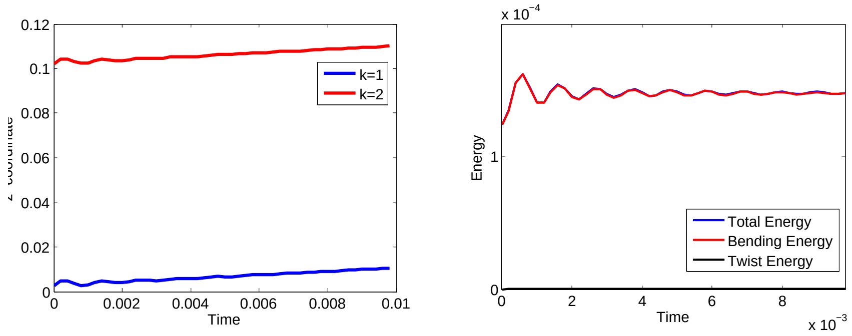

(d) Wave of z-coordinate at different positions along the length of the rod

(e) Energy of the rod

Figure 4.14: Simulation 1 - Free rod propagating a helical bending wave of frequency $\sigma = 2 \times 10^4$. Parameter values can be found in Table 4.9 and Table 4.10.

periodic change. Compared to Figure 4.14 (c) in Simulation 1, the maximum amplitude achieved at the two endpoints of the rod decreases from 0.04 to 0.02 despite the fact that we prescribe the rod with exactly the same intrinsic twist $\mathbf{\Omega}(s,t)$, which implies the same κ and therefore, the same amplitude. Comparing the achieved amplitude among the three chosen points along the rod, we still see that the mid-point has the least movement among the three with the smallest amplitude. The amplitude achieved at the two endpoints are approximately equal. The waveform at the two endpoints differ only in phase of the motion. Note that the frequency of the oscillation also increases due to the increased input σ.

Figure 4.15 (c) shows the time evolution of the energy. In this figure, we observe a more frequent oscillation of the energy in the initial stage compared to Simulation 1; this can be explained by the increased frequency of the traveling wave and decreased period of the overall oscillation. Notice that similar to Simulation 1, the energy eventually tends towards a constant value as time elapses. To summarize, with the same material moduli, an increase in σ decreases the amplitude achieved by the rod. As the wave propagates faster along the rod, the rod is required to bend faster to keep up with the wave propagation. However, due to the constraints of the bending modulus of the rod itself, the rod is unable to keep up its motion with the traveling speed and the prescribed amplitude of the wave. The inability of the rod to achieve the prescribed amplitude is seen more remarkably through the inconsistent amplitude of the oscillation at a given point. Notice that in Table 4.10, the increased σ also results in a smaller swimming speed along the z-axis; we see that when a rod is incapable of achieving its prescribed amplitude, it also loses the ability to swim faster along the z-axis. This agrees with the results presented in [24] where swimming speed is found to scale quadratically with amplitude. Thus, a smaller achieved amplitude gives a decreased swimming speed.

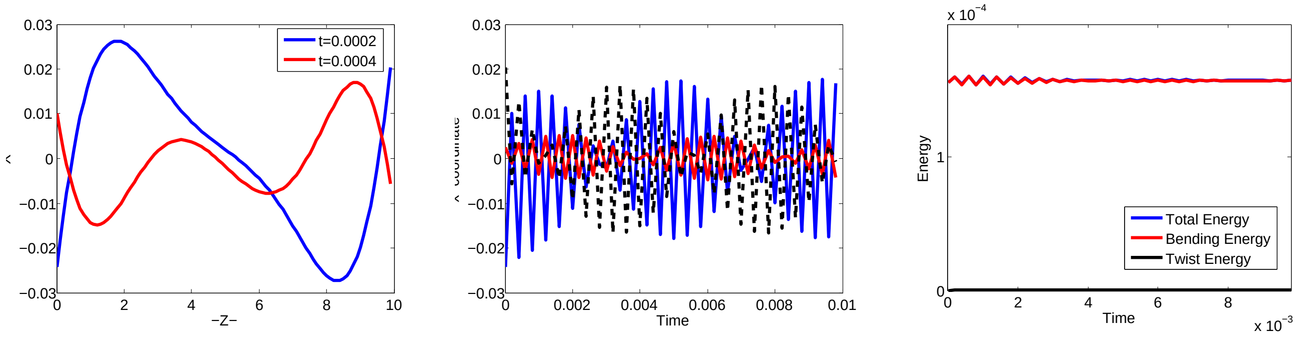

(a) Waveform of the rod

(b) Wave of x-coordinate at different positions along the length of the rod

(c) Energy of the rod

Figure 4.15: Simulation 2 - Free straight rod propagating a helical bending wave and $\sigma = 5 \times 10^4$ which has been increased compared to Simulation 1. Parameter values can be found in Table 4.9 and Table 4.10.

Table 4.10: Free rod propagating a helical bending wave (Sim. 1 - Sim. 4) where σ is increasing from Sim. 1 to Sim. 4

Parameter	Sim. 1	Sim. 2	Sim. 3	Sim. 4
Period T (s)	0.001	4.19×10^{-4}	2.0944×10^{-4}	1.0472×10^{-4}
Swimming speed v (μms^{-1})	0.8	0.273	0.1426	0.0106

To explore the behavior of the rod with a helical bending wave with an increasing frequency, we continue to increase σ. In Simulation 3 and Simulation 4, we set $\sigma = 100000$ and $\sigma = 200000$ respectively. Figure 4.16 (a) shows the wave propagating along the length of the rod at $t = 0.0002$ s, approximately the end of one period of the rod oscillation. From this figure, the rod achieves a maximum amplitude of 0.01, which is even smaller than the amplitude achieved in Simulation 2. Figure 4.16 (b) shows the movement of the x-coordinate of the same three chosen points. Compared to Figure 4.15 (b), the increased σ does not lead to a higher frequency wave along the x-axis at each endpoint. The amplitude achieved by the rod at each point, though small, is constant with respect to time at each chosen point. In fact, at each chosen point, the oscillation becomes slower than Simulation 1 and Simulation 2. Figure 4.16 (c) shows the time evolution of the energy of the curve. The total energy of the rod is comparable to that in Simulation 1 and Simulation 2. However, in contrast to the previous two simulations, we observe almost no oscillations due to the high frequency. Figure 4.16 (d) shows the propagation of the wave along the rod at $t = 0.0002$ s, approximatley after two periods of its oscillation. The form of the wave is similar to (a), however with a much smaller amplitude. The achieved amplitude has a scale that is one order of magnitude less than (a). Figure 4.16 (e) is the Simulation 4 counterpart of movement of the x-coordinate at different positions along the rod. We notice the oscillation of the rod along the x-axis is similar to that of Simulation 3 shown in (b), but the amplitude is significantly decreased and the period of the oscillation is longer. Figure 4.16 (f) is the energy of the rod of Simulation 4, from which we see that the energy shares approximately the same value and pattern with that of Simulation 3.

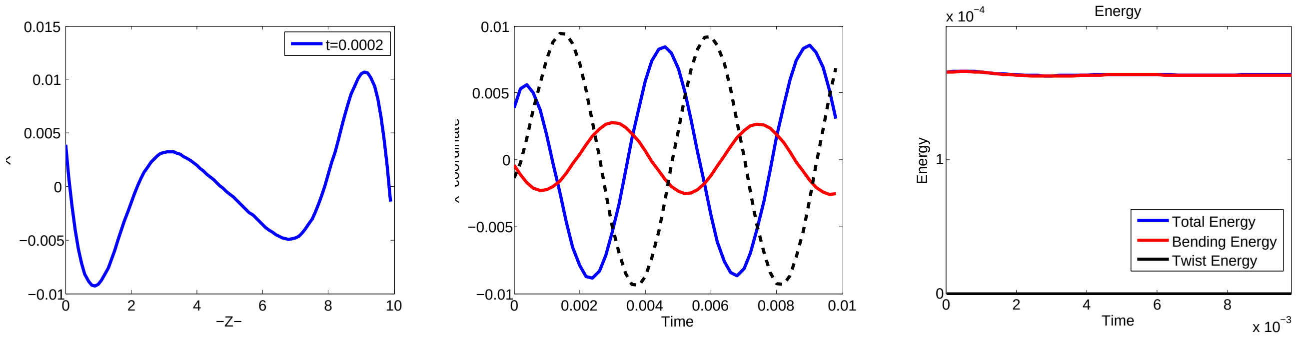

(a) Waveform of the rod

(b) Wave of x-coordinate at different positions along the length of the rod

(c) Energy of the rod

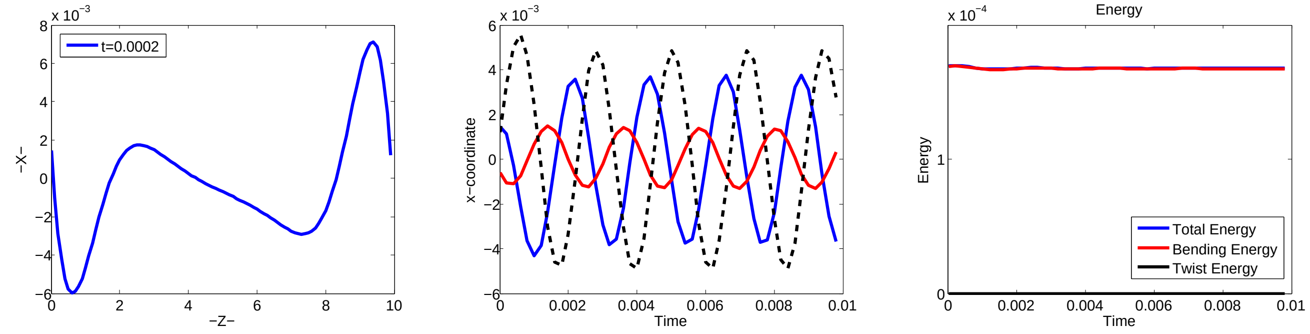

(d) Waveform of the rod

(e) Wave of x-coordinate at different positions along the length of the rod

(f) Energy of the rod

Figure 4.16: (a) - (c) show the helical wave in Simulation 3 (Free rod and $\sigma = 100000$); (d) - (f) show the helical wave in Simulation 4 (Free rod and $\sigma = 200000$)

Table 4.11: Free rod propagating a helical bending wave (Sim. 5 - Sim. 8)

Parameter	Sim. 5	Sim. 6	Sim. 7	Sim. 8
Changed Parameter	$a_1 = a_2 = 5.5 \times 10^{-3}$	$\mu = 8.9 \times 10^{-5}$	$\mu = 8.9 \times 10^{-8}$	$(r, p) = (0.5, 2.5)$
Period T (s)	0.001	0.001	0.001	3.2239×10^{-4}
Swimming speed v (μms^{-1})	1.8456	1×10^{-4}	22.7572	1442.2

To verify that the waveform achieved by the rod is indeed affected by the material moduli of the rod, we increase the bending modulus in the following simulation. In Simulation 5, we change the bending modulus $a_1 = a_2$ from 3.5×10^{-3} in the standard parameter set to 5.5×10^{-3} and keep the rest of the parameters unchanged. Eq. (4.4a) shows the equation for bending energy. Increases in bending

Table 4.12: Free rod propagating a helical bending wave in high viscosity fluid

Frequency σ	20000	-100	-100
Helical parameter (r, p)	(1,3)	(0.5,2.5)	(0.1,1.5)
Swimming speed v	1×10^{-4}	0.0936	0.0302
Maximum energy E	1.7×10^{-4}	1.7×10^{-4}	3.3×10^{-5}

modulus will increase this energy. To minimize the energy, the rod will adjust itself to a different configuration. Figure 4.17 (a) shows the propagating wave along the length of the rod at different time points. Since we keep σ unchanged compared to Simulation 1, the period of the oscillation remains unchanged. From Figure 4.17 (a), we see a similar phase of the motion of the rod. Compared to Figure 4.14 (b), the wave looks smoother and also shows a slightly higher amplitude. Figure 4.17 (b) shows the oscillation of the x-coordinate of the two endpoints and the mid-point along the rod. The frequency of the oscillation remains the same with that observed in Simulation 1 due to the unchanged σ value. However, the achieved amplitude increases from 0.04 to 0.06 for the two endpoints; for the mid-point, the achieved amplitude also increases to above 0.02 as opposed to below 0.02 in Simulation 1. Figure 4.17 (c) shows the time evolution of energy of the rod. While the frequency of the energy oscillation looks identical to that in Figure 4.14 (e), the energy level is higher in Simulation 1. Notice that the average swimming speed of the rod in Simulation 5, which can be found in Table 4.11, is significantly higher than the value calculated in Simulation 1 and Simulation 2. We conclude that a greater bending modulus enables the rod to achieve a greater amplitude and swimming speed under the same condition. Due to a greater bending energy and a faster movement, the rod demonstrates a greater total energy. Simulation 5 verifies our previous assumption that given a prescribed helical wave, the greater the bending modulus, the more likely it is for the rod to achieve its prescribed waveform. Note that if the bending modulus is too large, the rod might be too stiff to bend to achieve its prescribed configuration in which case, it might be unable to achieve its prescribed configuration.

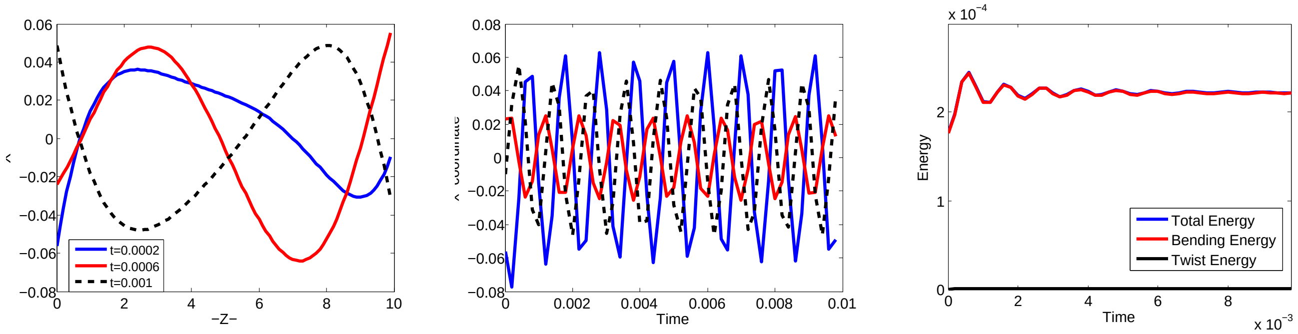

(a) Waveform of the rod

(b) Wave of x-coordinate at different positions along the length of the rod

(c) Energy of the rod

Figure 4.17: Simulation 5 - Straight free rod propagating a helical bending wave with bending moduli $a_1 = a_2 = 5.5 \times 10^{-3}$. Parameters can be found in Table 4.9.

Fluid viscosity μ is a measure of resistance to flow. We infer that changes in fluid viscosity will also result in changes in the motion of a rod propagating a helical bending wave. In Simulation 6 and Simulation 7, we alter the value of fluid viscosity in each simulation while keeping the rest of the parameters unchanged and explore the behavior of the rod under each condition. In previous simulations, we use $\mu = 8.9 \times 10^{-7} g\mu\text{m}^{-1}\text{s}^{-1}$, which is the viscosity value of water. In Simulation 6, we increase the fluid viscosity by scaling μ by 100. We set $\mu = 8.9 \times 10^{-5} g\mu\text{m}^{-1}\text{s}^{-1}$ and apply the same helical bending wave to the rod. Figure 4.18 (a) shows the wave along the length of the rod at different time points throughout the evolution. Note that we keep the frequency σ unchanged from the standard parameter set and thus the rod has the same period of oscillation. Noticeably, the achieved amplitude of the rod is significantly less than that observed in all our previous simulations, with an order of magnitude of only 10^{-3}. We can also see from the figure that along the length of the rod, only points towards the end of the rod demonstrate remarkable movement. The middle of the rod remains almost motionless about the x-axis. This can be explained by the increased fluid viscosity which corresponds to an increased resistance to motion. Figure 4.18 (b) shows the oscillation of the x-coordinate of the endpoints and the mid-point of the rod. In this figure, we see that the mid-point is oscillating with the smallest amplitude. The oscillations at the two endpoints look unsymmetric with the bottom point oscillating in the negative x-axis and the top point in the positive x-axis. The point at the top oscillates at an amplitude of approximately 7×10^{-4} while the point at the bottom has an oscillating amplitude of approximately 5×10^{-4}. Figure 4.18 (c) shows the time evolution of energy of the rod. The energy level of the rod is about the same as that in Simulation 1.

Due to the increased fluid viscosity, we observe an oscillation of smaller amplitude. This verifies that an increase in fluid viscosity indeed leads to a more damped oscillation of the rod. In Table 4.11, we calculate the average swimming speed of the rod. For most points along the length of the rod, the movement along the z-axis is nearly zero. The small deviation from zero can be interpreted by the oscillation about its original location. Simulation 6 shows that for a given rod propagating the same wave, it is more difficult to generate swimming speed in a high viscosity fluid than when it is immersed in a low viscosity fluid. However, we show that it is possible for the rod to improve its swimming speed by adjusting its swimming strategy, i.e. the wave it propagates to achieve movement. Table 4.12 shows the result of three simulations of a free rod propagating a helical bending wave in a fluid with relatively higher viscosity. In all of the three simulations, $\mu = 8.9 \times 10^{-5}$. The first column represents the simulation result of Simulation 6. The second and third column represents two additional simulations we run to study the effect of swimming strategy on swimming speed. In the first additional simulation, we change the helical waveform by decreasing σ to -100 and changing (r,p) to $(r, p) = (0.5, 2.5)$. Note that -100 represents the propagation of wave in an opposite direction as does in Simulation 6. In the second additional simulation, we change the helical waveform to $(r, p) = (0.1, 1.5)$ and set $\sigma = -100$. Note that immersed in the fluid of same viscosity, the rod is able to achieve a greater average swimming speed by decreasing the traveling wave frequency σ. Comparing the second and third column, we see that for a rod propagating a wave of same frequency σ, the swimming speed is also determined by helical wave parameter (r, p) of the wave it propagates. Moreover, propagating a wave of different helical radius and pitch, the rod also has a different energy profile. We see from the table that when the rod propagates a wave with $(r, p) = (0.5, 2.5)$, while it is able to achieve a higher swimming speed, it also consumes a higher energy than when $(r, p) = (0.1, 1.5)$. Depending on the biological context, there might exist an optimal swimming strategy of swimming speed and energy consumption for a micro-organism trying to swim in a highly viscous fluid. However, by comparing the second and third column to the first column, i.e. Simulation 6, we conclude that in a high viscosity environment, decreasing σ is not only conducive to increasing the swimming speed but also decreasing energy consumption and improving energy efficiency.

In Simulation 7, we decrease the fluid viscosity by scaling the original μ by $\dfrac{1}{10}$. We set $\mu =$

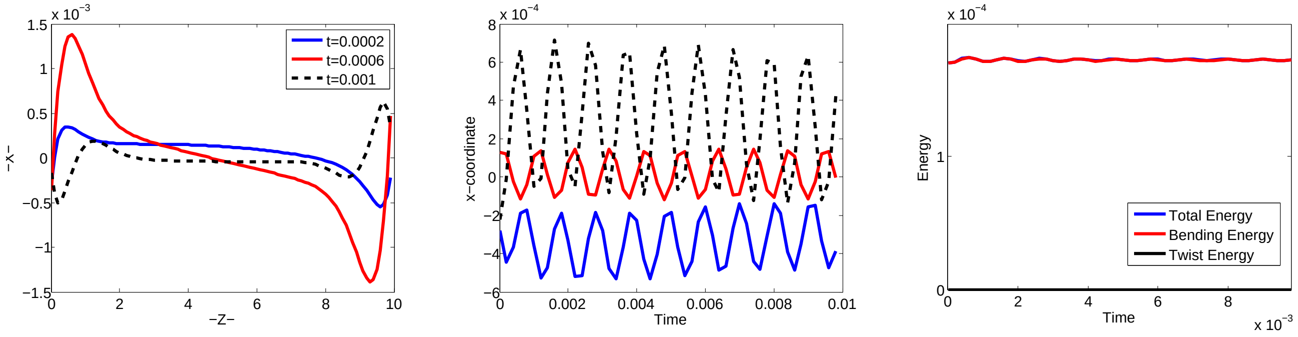

(a) Waveform of the rod

(b) Wave of x-coordinate at different positions along the length of the rod

(c) Energy of the rod

Figure 4.18: Simulation 6 - Free straight rod propagating a helical bending wave in a fluid with viscosity $\mu = 8.9 \times 10^{-5}$. Parameters can be found in Table 4.9.

$8.9 \times 10^{-8} g\mu \mathrm{m}^{-1}\mathrm{s}^{-1}$. Figure 4.19 (a) shows the configuration of the rod at $t = 0.01$ s. From the configuration of the rod, we see that the rod seems to oscillate more homogeneously along the length of the rod. Figure 4.19 (b) shows the waveform propagating along the length of the rod. Compared to Simulation 6, the achieved amplitude of the rod is significantly higher. The curve looks smoother and the rod seems to be bending less than the previous simulations. Figure 4.19 (c) shows the movement of the x-coordinate of the same three chosen points on the rod. The rod achieves a much greater amplitude compared to Simulation 6, but still a smaller amplitude compared to Simulation 1. Comparing the oscillation of the same three chosen points on the rod, we see a smaller gap between the amplitude at different positions along the length of the rod. The point at the top of the rod shown by the black dashed line oscillates at about the same amplitude as the mid-point, in contrast to the previous simulations where the amplitudes at the two endpoints of the rod are much higher. Figure 4.19 (d) shows the movement of the z-coordinate of the first and second point close to the bottom of the rod. The much greater slope of the lines compared to Simulation 1 shows that the rod is swimming at a much higher speed than Simulation 1. In Table 4.11, we calculate the swimming speed of the rod in this simulation to be 22.7572, which is approximately one order of magnitude greater than that of Simulation 1. Figure 4.19 (e) shows the time evolution of the energy of the rod. Compared to previous simulations, the energy of the rod is a lot lower with no significant oscillation, which agrees with the relatively small amplitude observed in Part (c) of Figure 4.19. The results of Simulation 7 with a decreased fluid viscosity indicate that for a given rod propagating a given helical bending wave, a lower viscosity leads to a higher swimming speed and is more beneficial for a rod to achieve its prescribed waveform. Lim also studies the relationship between fluid viscosity and instability of a straight rod with nonzero intrinsic twist in [14]. The study in [14] shows that for a rod with given intrinsic twist, increases in fluid viscosity result in equilibrium configurations with increasing instability and increasing total energy. This agrees with our result that the total energy of the rod in Simulation 6 is higher than that in Simulation 7.

Based on our analysis, given a prescribed helical wave, bending moduli, fluid viscosity and traveling wave frequency all play a critical role in affecting the behavior of the rod. In turn, we are also interested in the behavior of the rod prescribed with a different helical bending wave, namely a different curvature and torsion, given a set of certain bending moduli, fluid viscosity and wave frequency. In Simulation 8,

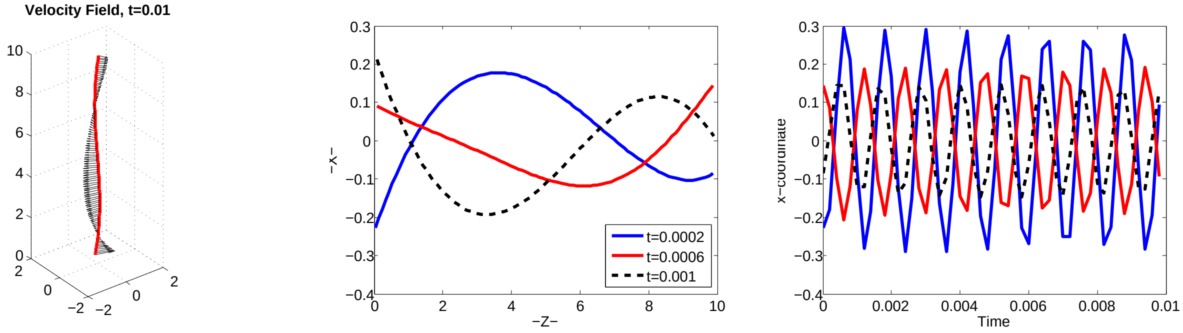

(a) Rod configuration

(b) Waveform of the rod

(c) Wave of x-coordinate at different positions along the length of the rod

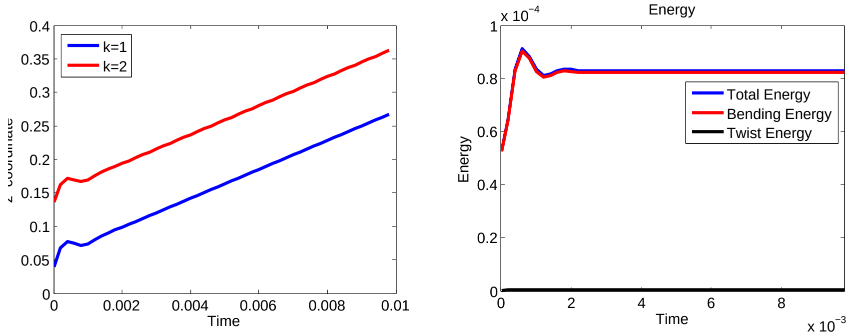

(d) Wave of z-coordinate at different positions along the length of the rod

(e) Energy of the rod

Figure 4.19: Simulation 7 - Free straight rod propagating a helical bending wave in a fluid with viscosity $\mu = 8.9 \times 10^{-8}$. Parameters can be found in Table 4.9.

we set $r = 0.5$ and $p = 2.5$ as opposed to $r = 1$ and $p = 3$ in the standard parameter set and keep the remaining parameters unchanged from the standard parameter set. Note that compared to the helix with $(r, p) = (1, 3)$, $(r, p) = (0.5, 2.5)$ means a less compressed and twisted helix. Using Eq. (4.13a) and Eq. (4.13b), we have $\kappa = 0.0769$ and $\tau = 0.3846$. Figure 4.20 (a) shows the prescribed helix, i.e. a helix defined by $(r, p) = (0.5, 2.5)$. Figure 4.20 (b) - (c) show the rod configuration and position at the initial time evolution and at the end of the evolution respectively. From (b) to (c), the rod evolves from a straight configuration to its helical configuration defined by prescribed helical parameters. More noticeably, the displacement of the rod along the z-axis is much greater than any of the simulations observed previously. The calculated average of the rod's swimming speed is given in Table 4.11, which differs from the swimming speed of the rod in Simulation 1 by up to two orders of magnitude. Figure 4.20 (d) shows the wave that propagates along the length of the rod at different time points. We see that in this figure, the maximum amplitude achieved by the rod reaches 0.6, which is higher than that observed in Simulation 1.

Figure 4.20 (e) shows the oscillation of the rod at the bottom, middle and top of the rod as time elapses. We see that as time evolves, the amplitude of oscillation at each point is decreasing remarkably for the two endpoints while the decrease is not obvious for the mid-point represented by the blue line. This decrease in oscillation indicates the decreased movement of the rod overall, implying that the rod is approaching some form of equilibrium, which can also be seen from the plateau in Figure 4.20 (g) which will be discussed shortly. Figure 4.20 (f) shows the displacement of the first two points from the bottom of the rod along the z-axis. A positive displacement indicates movement in the direction of positive z-axis. From this figure, we see that the rod moves along the positive z-axis at the initial stage of the evolution and does not start moving down until it reaches $z = 2\mu$m. Figure 4.20 (g) shows the energy of the rod, from which we see that the total energy and bending energy of the rod is decreasing since the beginning of the time evolution. The total energy and bending energy reach an equilibrium roughly after $t = 2 \times 10^{-3}$ s. In contrast to all our previous simulations, the twisting energy of the rod in this simulation is not zero. The twisting energy increases after the rod starts moving and remains at a relatively constant level as the rod approaches an equilibrium. Compared to the previous simulations, the order of magnitude of the energy of the rod in this case is significantly higher. Note that the energy is of order 10^{-4} fJ in Simulation 1 through Simulation 7. In this simulation, the rod starts with an energy of 0.013 fJ and approaches approximately 0.008 fJ at the end of the simulation. This increased energy can be explained by the increased kinetic energy of the rod as it moves along the z-axis. Note that kinetic energy is the energy possessed by an object in motion, computed by $E_k = \frac{1}{2}mv^2$ where m is the mass and v is the velocity. Hence, with a greater speed, the rod possesses a greater kinetic energy.

Note that for all the simulations mentioned previously, we set the frequency σ to be positive. As mentioned previously, the sign of σ determines the direction in which the wave propagates along the rod. From Simulation 8, we see that a positive σ leads to a major movement in the direction of negative z-axis despite the fact that the rod starts moving in the direction of positive z-axis initially. Note that the movement along the positive z-axis is temporary. The rod starts to move in the negative z-axis immediately after the rod deforms into a helical shape. In the following simulations, we change the sign of σ by setting σ to be negative. We set $\sigma = -1000$ in Simulation 9 and set $\sigma = -20000$ in Simulation 10. We keep the rest of the parameters identical to the standard parameter set. Figure 4.21 (a) - (e) show the simulation results of Simulation 8. Figure 4.21 (a) shows the configuration and position of the rod at $t = 0.2$ s. As expected, the rod moves in a direction opposite to Simulation 8 where we implement a positive σ. Figure 4.21 (b) shows the wave propagating along the length of the rod at three different time points. We notice that the rod achieves a maximum amplitude of approximately 0.8, which is higher than any of the simulations run before. Figure 4.21 (c) shows the oscillation of the rod along the x-axis where the smaller σ applied results in a less frequent oscillation and greater wavelength. Similar to Simulation 8, the mid-point of the rod continues to have the greatest amplitude in oscillations among all of the three points. Figure 4.21 (d) shows the displacement of the rod along the z-axis. Notice that the rod is moving along the positive z-axis throughout time evolution. The swimming speed, which is calculated by taking the ratio of displacement over time, is shown in Table 4.13. Figure 4.21 (e) shows the energy profile of the rod. The energy of the rod decreases rapidly after the rod starts moving. Note that we also have a nonzero twisting energy in this case. Figure 4.21 (f) - (i) show the simulation results of Simulation 10. Figure 4.21 (f) shows the wave propagating along the length of the rod. The maximum amplitude of the wave achieved is 0.5. Figure 4.21 (g) and (h) show the oscillation of the rod about the x-axis and z-axis respectively. We note that this is different from our previous results with a positive σ in that when σ is positive, a greater σ value leads to a smaller swimming speed. However, in the situation where σ is negative, an increase in the magnitude of σ leads to a greater swimming speed, which is shown in Table 4.13. Figure 4.21 (i) shows the energy of the rod which is higher compared to (e) and similar to Figure 4.20 (h).

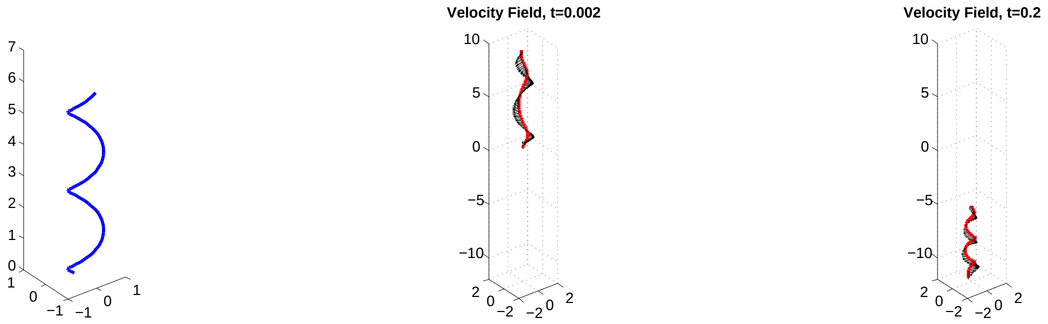

(a) Rod at $t = 0.0001$ s (b) Rod at $t = 0.0001$ s (c) Rod at $t = 0.01$ s

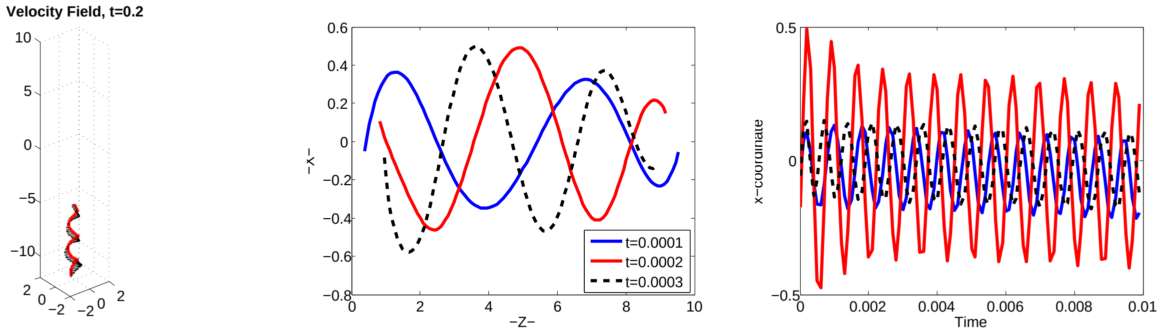

(d) Rod at $t = 0.01$ s (e) Wave propagating along the rod (f) Wave of x-coordinate at different positions along the length of the rod

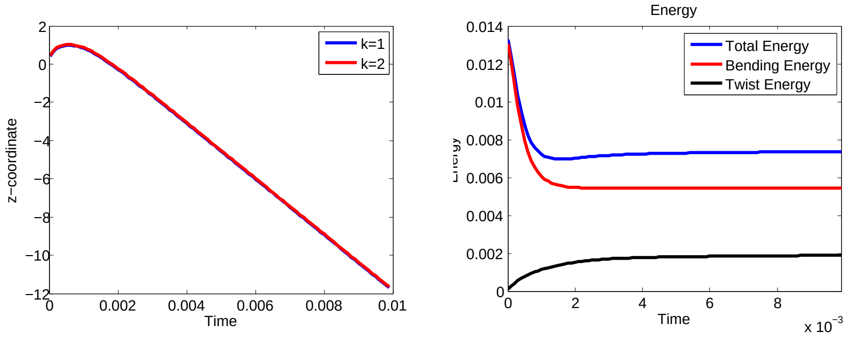

(g) Wave of z-coordinate at different positions along the length of the rod (h) Energy of the rod

Figure 4.20: Simulation 8 - Free straight rod propagating a helical bending wave with helical parameter $(r, p) = (0.5, 2.5)$. Parameter values can be found in Table 4.9.

Table 4.13: Free rod propagating a helical bending wave upward (Sim. 9 - Sim. 10)

Parameter	Sim. 9	Sim. 10
Period T (s)	0.0064	3.2239×10^{-4}
Swimming speed v (μms^{-1})	217.3348	1437.4

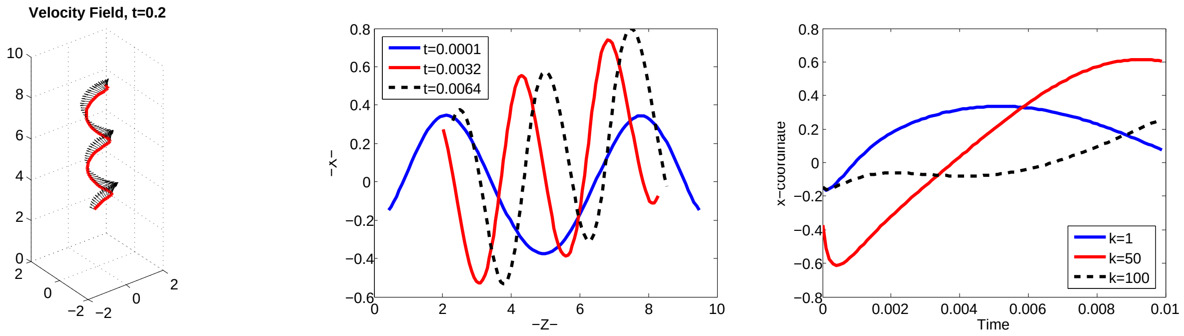

(a) Rod figuration at $t = 0.2$ s (b) Wave propagating along the rod (c) Wave of x-coordinate at different positions along the length of the rod

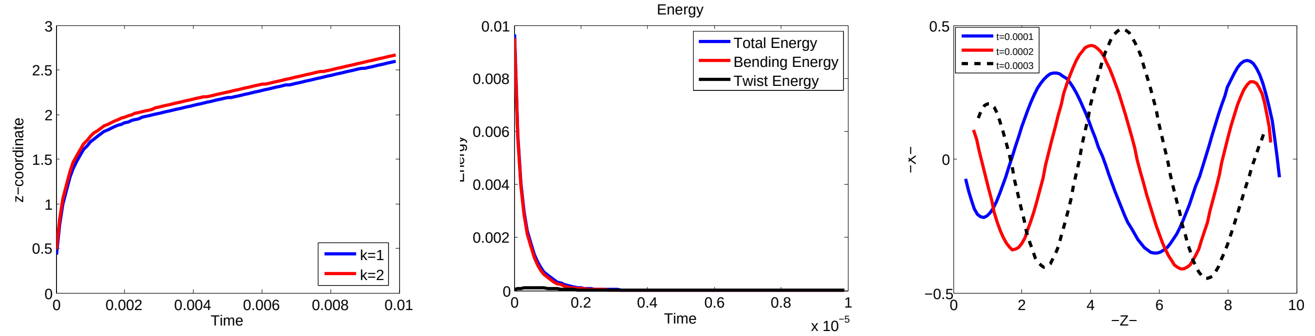

(d) Wave of z-coordinate at different positions along the length of the rod (e) Energy of the rod (f) Wave propagating along the rod

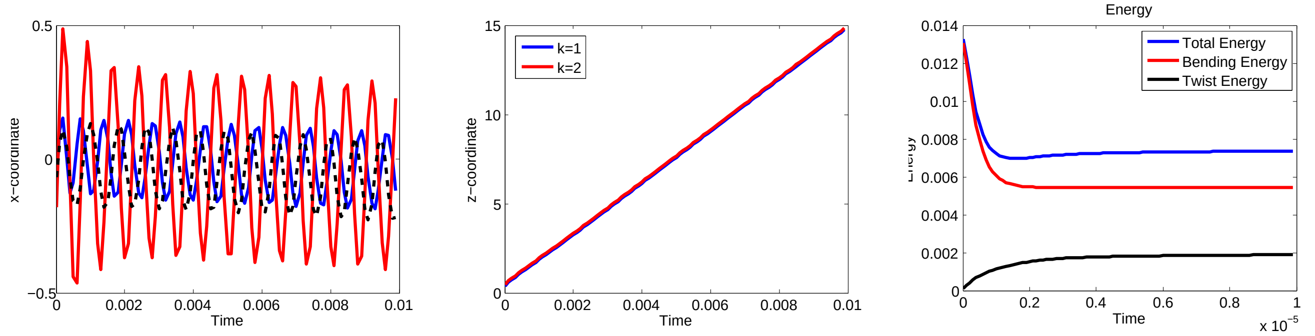

(g) Wave of x-coordinate at different positions along the length of the rod (h) Wave of z-coordinate at different positions along the length of the rod (i) Energy of the rod

Figure 4.21: Simulation 9 - Free Rod propagating a helical bending wave with frequency $\sigma = -1000$; Simulation 10 - Free rod propagating a helical bending wave with frequency $\sigma = -20000$.

4.3.2 Helical Wave Propagating on a Tethered Rod

The distinctive behaviors of a free rod propagating a helical bending wave under different conditions imply that a rod, if tethered, might demonstrate instabilities under certain conditions. We now wish to explore the stability of a tethered rod propagating a helical bending wave. From the previous simulations of a free rod, we find that the frequency of the traveling wave σ and the prescribed helical wave determined by helical radius r and axial distance of one turn of the helix h could both affect the motion of the rod. In the following simulations, we tether the rod at the bottom using the same Hookean type force as described in Section 4.2 with a stiffness coefficient of $S = 50\ g\mu\mathrm{m}^{-1}\mathrm{s}^{-1}$. We vary frequency σ and helical parameters (r, p) in each simulation and compare the simulation results. First, in Simulation 11, we tether the rod and apply a helical bending wave with frequency $\sigma = 50000$ and a helical radius and axial distance $(r, p) = (1, 3)$. This gives the calculated period T, which is shown in Table 4.14. Figure 4.22 (a) shows the rod configuration as it propagates the helical bending wave, from which we see that the untethered end of the rod undergoes a rotation. Figure 4.22 (b) shows the wave that is propagating along the length of the tethered rod. With one end tethered, major oscillations are observed at the open end of the rod. Figure 4.22 (c) shows the oscillation of the rod about the x-axis at different points. Due to the high frequency of the propagating wave, both the mid-point and the endpoint show high frequency oscillation; it is also due to this high frequency that the achieved amplitude at the endpoint is relatively low. Figure 4.22 (d) shows the energy of the rod. Despite the oscillations, the energy of the rod remains at a relatively constant level, showing a relatively steady and periodic motion of the rod. Note that in this simulation, we are applying the same parameter set used in Simulation 1 through Simulation 4 except for frequency σ. From Table 4.10, we know that the swimming speed of the rod decreases with increasing σ. In an untethered condition, the swimming speed of the rod with $\sigma = 50000$ will lie between 0.1426 and 0.273, which is relatively small. This explains the steady motion, energy level and oscillation exhibited by the rod.

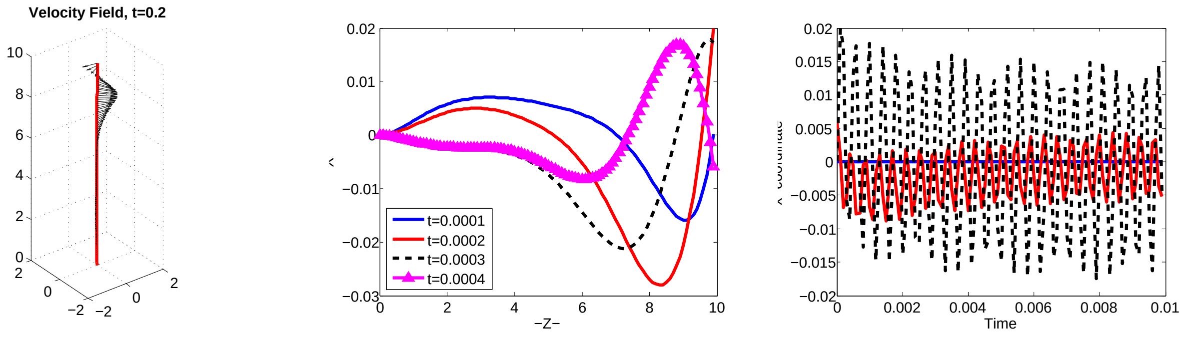

(a) Rod configuration

(b) Wave propagating along the rod

(c) Oscillation of the x-coordinate at different points on the rod

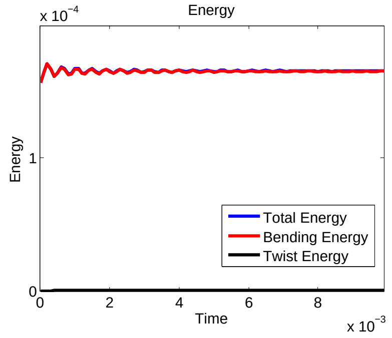

(d) Energy of the rod

Figure 4.22: Simulation 11 - Tethered rod propagating a helical bending wave with frequency $\sigma = 50000$ and helical parameter $(r, p) = (1, 3)$.

In Simulation 12, we increase σ to 100000 with the rest of parameters unchanged from Simulation 9. Table 4.14 shows the calculated period associated with this frequency. Figure 4.23 (a) shows the wave propagating along the rod. With an increased frequency σ, the wave has a smaller amplitude. Figure 4.23 (b) shows the oscillation of the rod at the same three chosen points. We see that the oscillation exhibits similar patterns with that of Simulation 2 shown in Figure 4.15 (b), in which case, the wave is propagating so fast that the rotation at the untethered end is incapable of keeping up with the frequency. Figure 4.23 (c) shows the energy of the rod. Despite the high frequency, the rod has a constant energy corresponding to a steady periodic rotation of the rod.

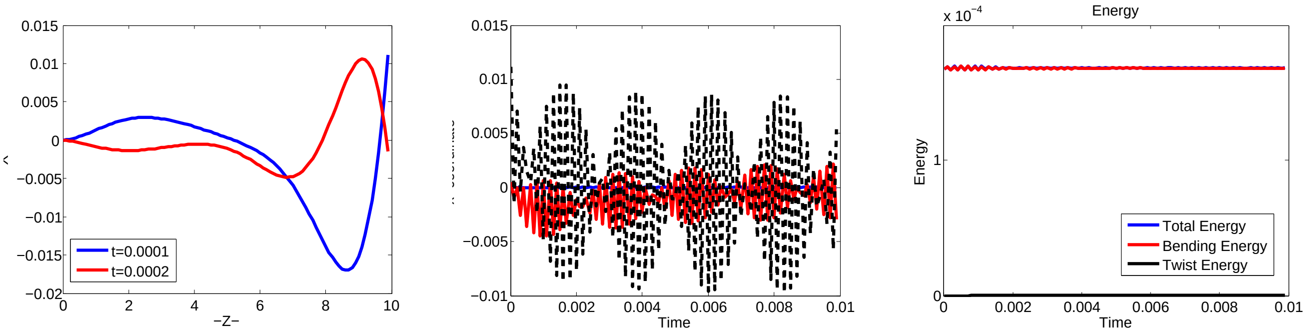

(a) Wave propagating along the rod (b) Oscillation of the x-coordinate at different points on the rod (c) Energy of the rod

Figure 4.23: Simulation 12 - Tethered rod propagating a helical bending wave of $\sigma = 100000$ and helical parameter $(r, p) = (1, 3)$

In Simulation 8, we change the helix parameters associated with the helical bending wave on a free rod and observe a much faster swimming speed of the rod along the negative z-axis. In the case of a tethered rod, we infer that if we apply the same helical bending wave used in Simulation 8 to a tethered rod, the greater swimming speed observed in an unloaded condition will transform to an instability of the rod. As mentioned previously, the sign of σ determines the direction in which the wave propagates and therefore the displacement of the rod along the z-axis. A positive σ leads to a propagation in the negative z-axis and a negative σ corresponds to a propagation in the positive z-axis. We run simulations for a tethered rod using two different signs for σ and explore its effect on the stability of the rod. In Simulation 13, we prescribe the tethered rod with a helical bending wave defined by $(r, p) = (0.5, 2.5)$ and $\sigma = 20000$ which corresponds to a major movement along the negative z-axis as is seen in Simulation 8. Note that this is the same parameter set we previously applied to a free rod in Simulation 8. Table 4.14 shows the calculated period associated with this parameter set. Figure 4.24 (a) shows the rod at $t = 0.01$ s. The rod appears to be undergoing a steady rotation similar to Simulation 11 and Simulation 12. Figure 4.24 (b) shows the wave propagating along the length of the rod at different points within one period of oscillation. Comparing this figure with Figure 4.20 (e), the waveform does not seem to be changed much by applying the tether force with the same amplitude and frequency.

Figure 4.24 (c) shows the oscillation of the x-coordinate at the two endpoints and mid-point of the rod. The mid-point of the rod represented by the red line starts off with a large amplitude oscillation about the origin. However, the amplitude decreases immediately and the axis of rotation starts to deviate from the z-axis as well. The unloaded endpoint at the top of the rod, which is represented by the black line has a relatively larger amplitude compared to the mid-point. Similarly, after the rod starts moving, the oscillation perturbs from the z-axis. At the end of the time evolution, the oscillation returns to the z-axis. Compared to Figure 4.20 (f) where the rod oscillates symmetrically about the z-axis, this is a sign that the propagating helical wave defined by (r, p) and σ is competing with the tether force at the bottom of the rod. The deviation of oscillation from the z-axis demonstrates the presence of an emerging instability. Figure 4.24 (d) is the energy profile of the rod. Compared to its counterpart in Simulation 8 shown in Figure 4.20 (h), the rod has an energy that is approximately twice as much as the free rod in Simulation 8. In contrast to the energy of the free rod in Simulation 8, the three types of energy (total energy, bending energy and twist energy) of the tethered rod in Simulation 13 all start with an immediate increase. After about the same amount of time, the energy also reaches a constant with small oscillations. Despite the fact that the rod is tethered and therefore exhibits no actual movement along the z-axis, the energy of the rod is higher than that observed in Simulation 8, which is another indicator of instability.

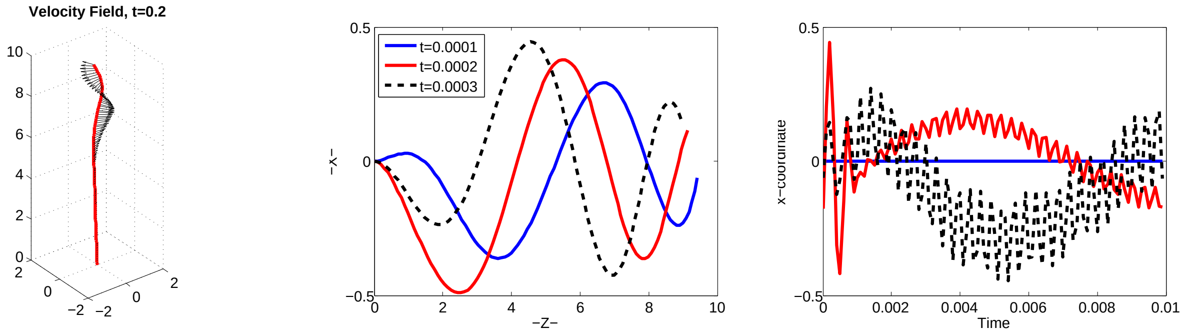

(a) Rod at $t = 0.2$ s

(b) Wave propagating along the rod

(c) Oscillation of the x-coordinate at different points on the rod

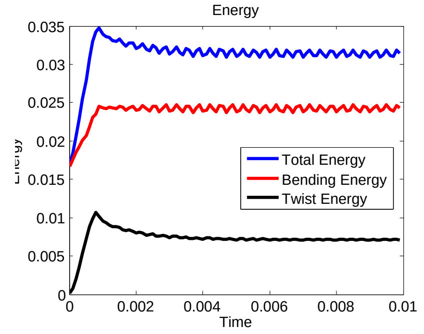

(d) Energy of the rod

Figure 4.24: Simulation 13 - Tethered rod propagating a bending wave with freqeuncy $\sigma = 20000$ and helical parameter $(r, p) = (0.5, 2.5)$

We have seen in simulations of a free rod with a positive σ that a smaller frequency contributes to a faster swimming speed. We have also seen some form of instability of the tethered rod in Simulation 13. We claim that if we decrease the frequency of the traveling wave, σ used in Simulation 13, then we should expect a greater instability of the rod. To verify this claim, we implement a frequency of $\sigma = 10000$ in Simulation 14 with the rest of the parameters unchanged from Simulation 13. Figure 4.25 (a) - (c) show the rod configuration at $t = 0.002$ s, $t = 0.1$ s and $t = 0.2$ s respectively. We see that as time evolves, the rod starts to demonstrate greater instability with compression and deformation not observed in Simulation 13. Figure 4.25 (d) shows the wave propagating along the length of the rod at $t = 0.0001$ s, $t = 0.005$ s and $t = 0.01$ s, corresponding to the rod configuration presented in (a), (b) and (c). Figure 4.25 (e) shows the oscillation of the three chosen points along the x-axis. The mid-point of the rod represented by the red line oscillates with an increasing amplitude as time elapses. The untethered open end of the rod represented by the black dashed line exhibits the same behavior although with a smaller amplitude compared to the mid-point. Note that the amplitude of the rod achieved by the mid-point reaches 1.5 at maximum, which triples the maximum amplitude achieved in Simulation 13. Figure 4.25 (f) is the energy profile of the rod from which we see approximately the same energy value as compared to Simulation 13. However, the rod has a more remarkable oscillation amplitude compared to Simulation 13. All of the signs shown by the results in Figure 4.25 indicate a greater instability of the rod.

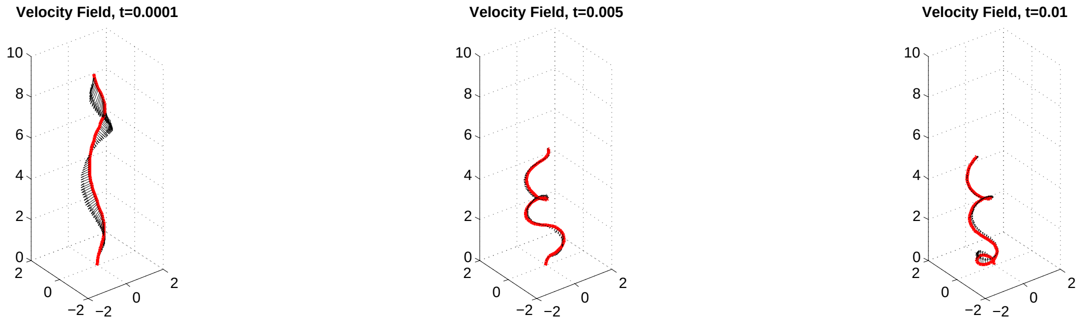

(a) Rod at $t = 0.0001$ s

(b) Rod at the middle of time evolution

(c) Rod at the end of time evolution

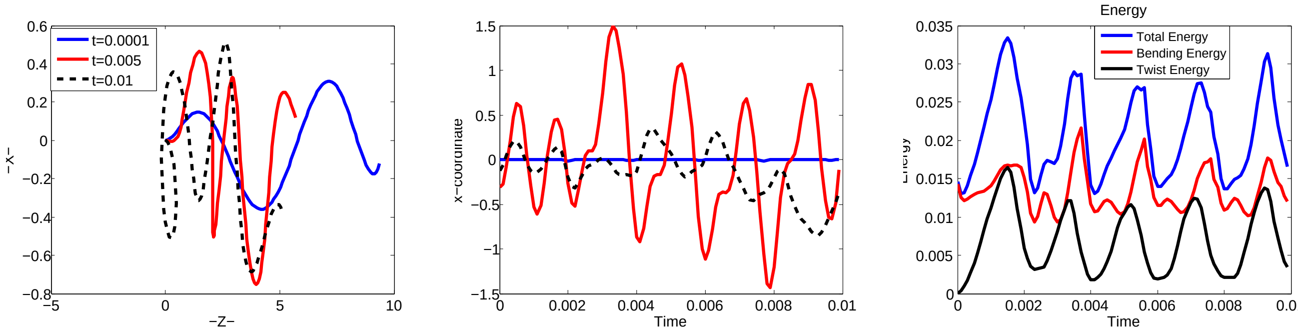

(d) Wave propagating along the length of the rod

(e) Oscillation of the x-coordinate at different points on the rod

(f) Energy of the rod

Figure 4.25: Simulation 14 - Tethered rod propagating a bending wave of frequency $\sigma = 10000$ and helical parameter $(r, p) = (0.5, 2.5)$

In Simulation 15 and Simulation 16, we apply the same parameter set used for Simulation 8 and Simulation 9 to a tethered rod and explore the stability of the rod in each case. Associated parameters

Table 4.14: Tethered rod propagating a helical bending wave downward (Sim. 11 - Sim. 14)

Parameter	Sim. 11	Sim. 12	Sim. 13	Sim. 14
Frequency σ	50000	100000	20000	10000
Prescribed (r, p)	(1,3)	(1,3)	(0.5,2.5)	(0.5,2.5)
Prescribed (κ, τ)	(0.1,0.3)	(0.1,0.3)	(0.0769,0.3846)	(0.0769,0.3846)
Period T (s)	4.1888×10^{-4}	2.0944×10^{-4}	3.2239×10^{-4}	6.4478×10^{-4}

can be found in Table 4.15. Figure 4.26 (a) shows the rod configuration at $t = 0.1$ s. In this simulation, the rod is undergoing a steady rotation as observed in Simulation 13 although there seems to be a deformation point at the bottom of the helix. Figure 4.26 (b) shows the wave propagating along the length of the rod. Figure 4.26 (c) shows the oscillation of the rod about the x-axis. The mid-point of the rod oscillates at a larger amplitude than the point at the top of the rod. The energy profile of the rod is shown in Figure 4.26 (d) where the total energy is relatively low compared to Simulation 13 and Simulation 14. After $t = 0.02$ s, the energy stays at a relatively constant level with some small oscillations.

Figure 4.26 (e) and (f) show the configuration of the rod at $t = 0.001$ s and $t = 0.002$ s respectively. We see that at $t = 0.002$ s, the rod has already shown instability with the buckling at the bottom of the rod. Figure 4.26 (g) shows the wave that is propagating along the rod at $t = 0.002$ s, $t = 0.004$ s and $t = 0.006$ s where we see that the rod starts to move drastically in the initial stage of time evolution. Figure 4.26 (h) shows the energy profile of the rod. The energy of the rod oscillates drastically as does Simulation 14 shown in Figure 4.25 (f). However, compared to Simulation 14, the energy of the rod is much higher in our current simulation. Note that in Simulation 14, the rod has a total energy of approximately 0.035 fJ whereas in Simulation 16, the rod has a total energy of approximately 0.14 fJ. This shows that with an increased traveling frequency in the direction of positive z-axis, we observe an instability of a tethered rod much more quickly than the case of a positive σ.

Table 4.15: Tethered rod propagating a helical bending wave upward (Sim. 15 - Sim. 16)

Parameter	Sim. 15	Sim. 16
Frequency σ	-1000	-20000
Prescribed (r, p)	(0.5,2.5)	(0.5,2.5)
Prescribed (κ, τ)	(0.0769,0.3846)	(0.0769,0.3846)
Period T (s)	0.0065	3.2239×10^{-4}

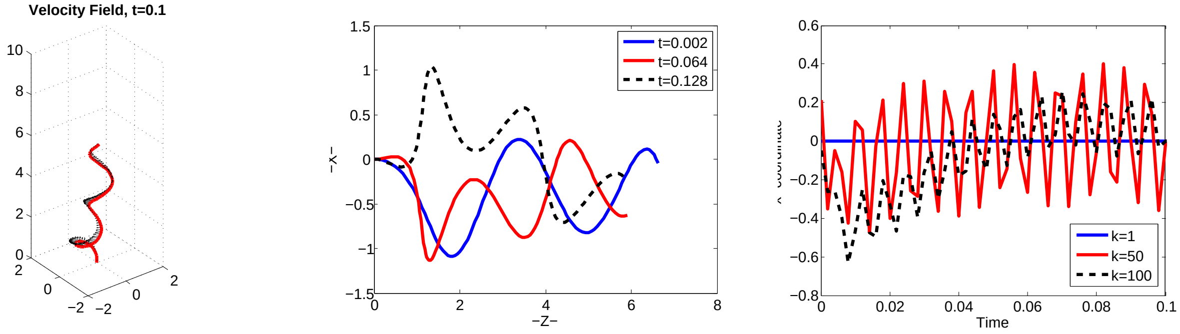

(a) Rod at $t = 0.1$ s (b) Wave propagating along the rod (c) Oscillation of the x-coordinate at different points on the rod

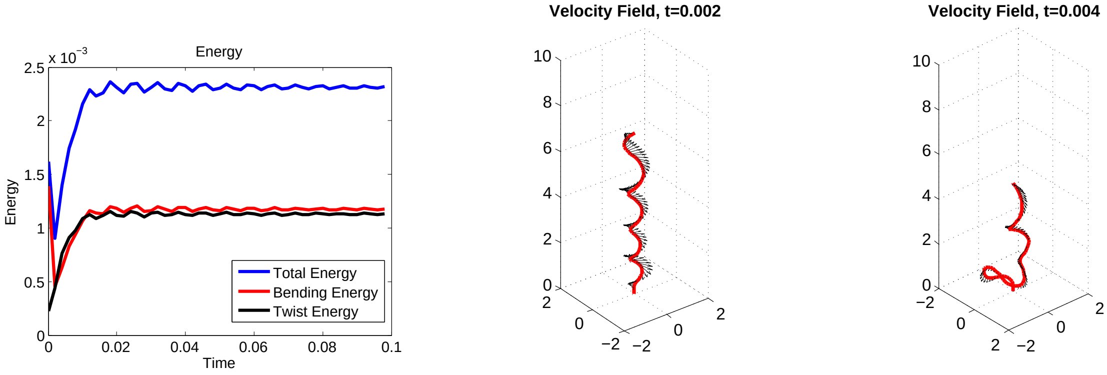

(d) Energy of the rod (e) Rod at $t = 0.002$ s (f) Rod at $t = 0.004$ s

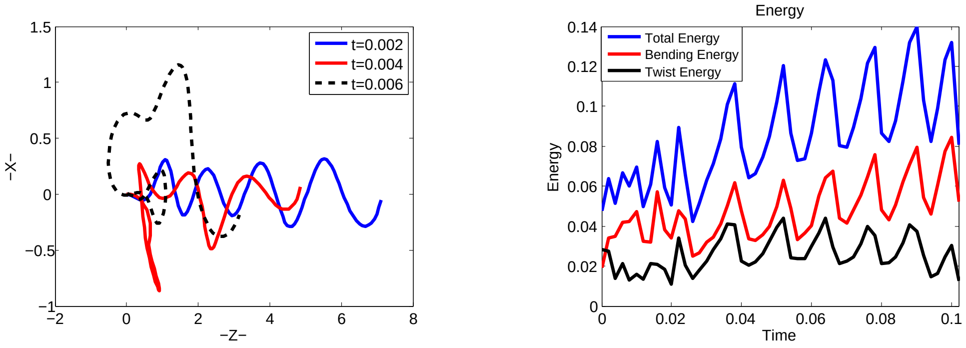

(g) Wave propagating along the rod (h) Energy of the rod

Figure 4.26: Simulation 15 - Tethered rod propagating a bending wave similar to Simulation 8 where $\sigma = -1000$; Simulation 16 - Tethered rod propagating a bending wave similar to Simulation 9 where $\sigma = -20000$.

Chapter 5

Conclusions

To summarize, we explored the effect of different material moduli and prescribed configurations on the helical equilibrium of a free and tethered rod. For a rod initialized as free and straight, depending on the helical configuration we prescribe relative to the bending and twist moduli of the rod, the rod may or may not achieve its prescribed configuration. In the presence of such a gap between achieved and prescribed configuration, the equilibrium achieved by the rod demonstrate an instability. We have found through our simulations that in the case where a rod initialized as straight and free, the rod achieves a stable helical equilibrium. The energy of the rod, including bending energy, twist energy and total energy is monotonically decreasing throughout the process. For a free rod, the energy at the two endpoints of the rod is symmetric and the energy at each free end occupies more than 10% of the energy of the entire rod. We conclude that for a free straight rod, the two free endpoints of the rod is dominating the energy profile of the entire rod compared to the rest of the immersed boundary points of the rod. In the process of achieving its equilibrium, all of the rod's energy components are minimized.

As an extension of Lim's study in [14] where the instabilities of helical equilibria of an open free elastic rod with zero curvature and nonzero twist are studied, we explore the instabilities of helical equilibrium of a tethered rod with nonzero curvature and nonzero twist. Depending on the prescribed helical radius and axial distance, the rod demonstrates stable equilibrium, buckling and loops. For a rod initialized as straight and tethered with a given rod length, as we increase the expected number of turns, we observe an increasing instability as the rod attempts to achieve a greater twist. We find that in all of the cases (stable equilibrium, buckling and loops), the total energy of the rod is decreasing; moreover, as the number of turns increases therefore leading to an increasing instability, the total energy of the rod also increases. This agrees with the results presented by Lim's earlier study in the case of free rod [14]. We observe that in comparison to the achieved helical configuration of an open elastic free rod, the position of buckling and loops of a tethered rod is shifted along the rod in such a way that the rod is no longer symmetric in order to balance the additional tether force added to the bottom of the rod. To balance the internal force and moment, the position of buckling and loops on a tethered rod is affected by both the prescribed configuration (expected number of turns) and the length of the rod.

In addition to the helical equilibria achieved by a rod that is initialized as straight and tethered, we extend our study to the instability of a tethered rod which is initialized as a helix. As the twist and therefore the expected number of turns of a helix increases, the rod shows similar forms of instability with buckling and loops. We find that while the total energy and twisting energy of the rod is minimized during the evolution of the rod, the bending energy of the rod is increased. As the prescribed twist and instability increase, the role of bending energy increases, implying that an increasing proportion of the total energy of the rod is converted to bending energy as the rod deforms to achieve more turns. This could be explained by the fact that the bending modulus of the rod is dominating over the rest of the material moduli and that it is this dominating role that constrains the rod from achieving a configuration that is increasingly bent and twisted. It has been pointed out in [9, 12] that a buckling instability of sperm has been observed in high-viscosity migration experiments of sperm. This buckling instability has led to assymmetric flagellar beating and circling motility. Relating with the buckling instability observed with our simulations, we may infer that this buckling instability may be a result of a sperm trying to deform into a shape it is incapable of achieving due to its own material properties.

Lim studied the instability of a free rod with zero curvature and nonzero twist. As an extension, we also explore the instability of a free rod with zero twist and an increasing curvature, which is virtually a circle of a certain radius. In our simulations, as the rod curls itself to achieve its prescribed configuration with an increasing twist, self-contacts occur. Inaccuracy of our simulation may result due to the occurence of these points of self-contact. However, the order of magnitude of the energy profile obtained in each case could more or less reflect the approximate energy level of the rod to some degree. We see that as the prescribed curvature increases, it becomes increasingly difficult for the rod to achieve its prescribed configuration and that the total energy of the rod is increasing rapidly suggesting an increasing level of instability. To further verify this claim, repulsive forces may be added to avoid self-contacts, which provides an interesting future work topic.

As mentioned in Chapter 1, the inertia is miniscule in zero Reynolds number flow. At a microscopic scale, the tendency of the surrounding fluid to continue moving is minimal when the object stops moving. Therefore, simple flapping motions are not able to produce motility on a microscopic length scale [12]. Micro-organisms like sperm solve this problem by producing a bending wave, which propagates along the flagellum [12]. Motivated by this mechanism, we also study the propagation of a helical bending wave on a rod and the instability associated with this wave. In our study of helical bending wave propagating on a free rod, we discover the different effects of traveling wave frequency σ on the behavior of the rod in two different regimes. For a free rod propagating a helical bending wave of handedness $h = 1$ and a given helical shape $(r, p) = (1, 3)$, we have found that increasing traveling wave frequency σ decreases the ability of the rod to achieve its prescribed bending waveform as well as its swimming speed within a traveling frequency range of $(20000, 200000)$. Note that within this range of σ value for this given helical waveform, the rod is never able to achieve its prescribed amplitude. We therefore conclude that within the regime where the rod is unable to achieve its prescribed amplitude, an increase in the traveling frequency σ leads to a decreasing achieved amplitue and an increasing total energy of the rod. When the same free rod propagates a bending wave of the same handedness $(h = 1)$ and a waveform of $(r, p) = (0.5, 2.5)$, we have found that the rod is able to achieve its prescribed amplitude. In such a case, as we increase the traveling frequency σ, the wave propagates faster. This faster propagation leads to an increased swimming speed and a higher total energy of the rod. The result obtained through our simulation suggests that when a micro-organism like sperm attempts to propagate a bending wave in a regime where it is unable to achieve its prescribed amplitude, an increase in propagation speed is no longer beneficial to its movement in the fluid, which in addition brings increased energy consumption. This simulation result in part explains the relatively low frequency observed in many motile micro-organisms, such as sea urchin sperm with a flagellar beating frequency of 30-80 Hz and E. Coli with a rate of rotation of its rotary motor within the range of 90-290 Hz [2, 7].

In our study of a helical bending wave propagating on a free straight rod, we have also found an asymmetric behavior of the rod with respect to the direction in which the wave propagates along the rod for a given handedness of the helical bending wave. In our mathematical formulation, the direction in which the wave propagates is determined by the sign of σ. Through our simulations, a positive σ corresponds to a wave propagation in the negative z-axis and a negative σ corresponds to a wave propagation in the positive z-axis. For a free rod propagating a helical bending wave in a regime where it is able to achieve its prescribed amplitude and swims with a remarkable swimming speed, a negative σ results in a rod movement in the positive z-axis throughout the movement of the rod. However, for the same rod propagating exactly the same wave in an opposite direction (positive σ), we have found that the rod starts off by moving along the positive z-axis for a short period of time in the initial stage of its movement and then starts to move in the negative z-axis. We observe that in this case, the rod is trying to first deform into its prescribed helical shape before generating substantial movement along the z-axis. This phenomenon shows the asymmetry of the rod movement with respect to the direction of wave propagation. This asymmetry also results in a different level of instability of a tethered rod propagating a helical bending wave. We infer that this asymmetry may be related to the handedness of the helical wave.

Sperm usually traverse a high-viscosity fluid enviroment before feritilization. Studies have revealed that fluid viscosity is a key factor determining the fertilization success of sperm and that fluid viscosity significantly alters rolling rate, planarity, and waveform of sperm [12, 22]. Studies have shown that in high viscosity fluids, sperm have a lower beat frequency, wavespeed and wavelength than in low viscosity fluids. However, the progressive velocity of sperm remains relatively constant in both fluid environments. In our simulations, we have found that for a rod propagating a given helical bending wave, increasing fluid viscosity has reduced the ability of the rod to achieve its prescribed amplitude. In a higher viscosity environment, the rod has a much lower achieved amplitude than when it is trying to propagate the same helical bending wave in a low viscosity environment. As is stated above, when the rod is unable to achieve its prescribed waveform, excessively high beat frequency only results in excessive energy consumption and decreased achieved amplitude. Hence, it is unlikely that sperm achieves an equal progressive velocity in high viscosity fluids as in low viscosity through increasing traveling wave frequency. We have found in our simulations, the ability of a rod to achieve its prescribed waveform depends on the waveform it is trying to propagate as well as its traveling wave frequency. Our simulations results show that in a high viscosity fluid, decreasing the traveling wave frequency and changing the waveform propagating along the rod both contribute to a greater swimming speed of the rod. This agrees with the discussion made previously in [22] based on the relationship between wavespeed and frequency. It is pointed out in [22] that if a sperm reduces its beat frequency, i.e. number of beats performed per second, it will consequently encounter the disadvantage of resistance from the highly viscous fluids less frequently, enabling it to achieve a relatively greater swimming speed. Through our simulations, we also observe that a greater swimming speed is also associated with a higher total energy of the rod. This implies that there may exist an optimized strategy for a swimming sperm in a viscous fluid, minimizing its energy consumption while maximizing its swimming speed. Sperm may do this by adjusting the bending wave frequency and/or the waveform including amplitude and pitch it propagates.

Appendix A

MATLAB Code

Main file

```
Parameters;
%Initialize the tether point
tether=0;
D1=zeros(3,nPt);
D2=zeros(3,nPt);
D3=zeros(3,nPt);

%Initialize the position of IB points
Lx=zeros(3,nPt);
Lx(1,:)=0;
Lx(2,:)=0;
ss=zeros(1,nPt);
for i=1:nPt
    Lx(3,i)=(1+epsil)*(i-1)*ds;
end
LH=zeros(3,nPt-1);
for i=1:nPt-1;
    LH(1,i)=1/2*(Lx(1,i+1)-Lx(1,i))+Lx(1,i);
    LH(2,i)=1/2*(Lx(2,i+1)-Lx(2,i))+Lx(2,i);
    LH(3,i)=1/2*(Lx(3,i+1)-Lx(3,i))+Lx(3,i);
end

%Initialize orthonormal triads
D1(1,1:nPt)=1;
D1(2,1:nPt)=0;
D1(3,1:nPt)=0;

D2(1,1:nPt)=0;
D2(2,1:nPt)=cos(epsil);
D2(3,1:nPt)=-sin(epsil);

D3(1,:)=0;
D3(2,:)=sin(epsil);
D3(3,:)=cos(epsil);

%Initialize the points around the centerline
xC=zeros(m+1,nPt);
yC=zeros(m+1,nPt);
```

```
zC=zeros(m+1,nPt);
fidEF=fopen('EF.txt','w');
fidENB=fopen('ENB.txt','w');
fidENT=fopen('ENT.txt','w');
fidUx=fopen('Ux.txt','w');fidUy=fopen('Uy.txt','w');fidUz=fopen('Uz.txt','w');
fidx=fopen('PosX.txt','w');fidy=fopen('PosY.txt','w');fidz=fopen('PosZ.txt','w');

for iStep=1:iter
    %Compute tangent vector of given IB positions
    TC = TangentVec(Lx);

    %Compute triads at half boundary points given triads at boundary points
    [DHn] = TriadHalfPt(D1,D2,D3);
    DH1 = DHn(:,:,1);
    DH2 = DHn(:,:,2);
    DH3 = DHn(:,:,3);

    %Compute internal force vector at half boundary point
    [FH E_F] = InternalForceHalfPt(DH1,DH2,DH3,TC,tether,iStep);

    %Compute internal moment at half boundary point
    [NH E_NB E_NT]= InternalMomentHalfPt(DH1,DH2,DH3,D1,D2,D3,tether,iStep);

    %Compute force and moment at boundary point
    MF = MomentnForce(NH,FH,TC,Lx);
    moment_Pt =  MF(:,:,1);
    force_Pt = MF(:,:,2);

    %Check the sum of forces and torques to ensure stability
    nx=sum(moment_Pt(1,:))
    ny=sum(moment_Pt(2,:))
    nz=sum(moment_Pt(3,:))
    fx=sum(force_Pt(1,:))
    fy=sum(force_Pt(2,:))
    fz=sum(force_Pt(3,:))
    Lx(:,1)

    %Enforce tether force if the rod is tethered
    if (tether == 1)
    force_Pt(1,1)=force_Pt(1,1)+S*(-Lx(1,1));
    force_Pt(2,1)=force_Pt(2,1)+S*(-Lx(2,1));
    force_Pt(3,1)=force_Pt(3,1)+S*(-Lx(3,1));
    end

    %Solve for linear velocity and pressure at IB points
    Up = RegStk(Lx,moment_Pt,force_Pt);
    IB_vel = Up(1:3,:);
    IB_p = Up(4,:);

    %Solve for angular velocity at IB points
    IB_ang = AngSolve(Lx,moment_Pt,force_Pt);

    %Update orthonormal triad
    Dn = updateTriadMot(D1,D2,D3,IB_ang,iStep);
    D1 = Dn(:,:,1);
    D2 = Dn(:,:,2);
```

```
    D3 = Dn(:,:,3);

    %Update positions
    Lx = updatePoints(IB_vel,Lx,nPt);

    if (mod(iStep,2000)==0)

    %Write energy to file
        fprintf(fidEF,'%f\n',E_F); %Write energy
        fprintf(fidENB,'%f\n',E_NB);fprintf(fidENT,'%f\n',E_NT);

        fprintf(fidx,'%f\n',Lx(1,:));fprintf(fidy,'%f\n',Lx(2,:));fprintf(fidz,'%f\n',Lx(3,:));
        fprintf(fidUx,'%f\n',IB_vel(1,:));fprintf(fidUy,'%f\n',IB_vel(2,:));fprintf(fidUz,'%f\n',IB_vel(3,:));

    end

end
 fclose(fidEF);fclose(fidENB);fclose(fidENT);
 fclose(fidx);fclose(fidy);fclose(fidz);
 fclose(Ux);fclose(Uy);fclose(Uz);
```

Bibliography

[1] J.H. Beinbockel. Introduction to tensor calculus and continuum mechanics. online, 1996. Available at http://www.math.odu.edu/ jhh/part1.PDF.

[2] H.C. Berg and L. Turner. Torque generated by the flagellar motor of escherichia coli. *Biophysics Journal*, 65:2201–2216, 1993.

[3] C.J. Brokaw. Torsion, twist, and writhe: the elementary geometry of axonemal bending in three dimensions. online, 2002. Available at http://www.cco.caltech.edu/ brokawc/-Suppl3D/TTWcomb.pdf.

[4] R. Cortez. Numerical methods based on regularized δ-distributions. UNC 2005.

[5] R. Cortez. The method of regularized stokeslets. *SIAM Journal on Scientific Computing*, 23:1204–1225, 2001.

[6] R. Cortez, L. Fauci, and A. Medovikov. The method of regularized stokeslets in three dimensions: Analysis, validation, and application to helical swimming. *Physics of Fluids*, 17:1204–1224, 2005.

[7] D. Eshel, C. Shingyoji, and K. et al. Yoshimura. Transient behavior of sea urchin sperm flagella following an abrupt change in beat frequency. *Journal of Experimental Biology*, 152:441–451, 1990.

[8] L. Fauci and C. Peskin. A computational model of aquatic animal locomotion. *Journal of Computational Physics*, 77:85–108, 1988.

[9] H Gadelha, E.A. Gaffney, and D.J. et al. Smith. Non-linear instability in flagellar dynamics: a novel modulation mechanism in sperm migration? *Journal of the Royal Society Interface*, 7:1689–1697, 2010.

[10] A. Goriely. On the dynamics of elastic strips. *Journal of Nonlinear Science*, 11:3–45, 2001.

[11] J.S. Guasto. Fluid mechanics of planktonic microorganisms. *Annual Review Fluid Mechanics*, 44:373–400, 2011.

[12] J.C. Kirkman-Brown and D.J. Smith. Sperm motility: is viscosity fundamental to progress? *Molecular Human Reproduction*, 17:539–544, 2011.

[13] E. Lauga and T.R. Powers. The hydrodynamics of swimming microorganisms. *Reports on Progress in Physics*, 72:400–412, 2009.

[14] S. Lim. Dynamics of an open elastic rod with intrinsic curvature and twist in a viscous fluid. *Physics of Fluids*, 22:2066–2083, 2010.

[15] M.D. Manson. Dynamic motors for bacterial flagella. *Proceedings of the National Academy of Sciences*, 107:11151–11152, 2010.

[16] P. Marks. Whip-tailed bacteria could tweet to nanobots. online. http://www.newscientist.com/article/dn19740-whiptailed-bacteria-could-tweet-to-nanobots.html.

[17] Medbib. Bacteria. http://www.medbib.com/Bacterium.

[18] S.D. Olson. Infinite support. Personal notes.

[19] SD Olson. Modeling the dynamics of an elastic rod with intrinsic curvature and twist using a regularized stokes formulation. *Journal of Computatonal Physics*, 238:169–187, 2013.

[20] C.S. Peskin. The immersed boundary method. *Acta Numerica*, 11:479–517, 2002.

[21] T.R. Powers. Dynamcis of filaments and membranes in a viscous fluid. *Reviews of Modern Physics*, 82:1607–1630, 2010.

[22] D.J. Smith, E.A. Gaffney, and N. et al. Kapur. Bend propagation in the flagella of migrating human sperm, and its modulation by viscosity. *Cell Motility and the Cytoskeleton*, 4:220–236, 2009.

[23] W.A. Strauss. *Partial Differential Equations*. John Wiley and Sons, Ltd, 2nd edition, 2008.

[24] G.I. Taylor. Analysis of the swimming of microscopic organisms. *Proceedings of the Royal Society of London A*, 209:447–461, 1951.